UCLA

Title

The TESS-Keck Survey. XVI. Mass Measurements for 12 Planets in Eight Systems

Permalink

https://escholarship.org/uc/item/11n957n7

Journal

ISSN

Authors

Murphy, Joseph M Akana
Batalha, Natalie M
Scarsdale, Nicholas
et al.

Publication Date

2023-10-01

DOI

Copyright Information

Peer reviewed

The TESS-Keck Survey. XVI. Mass Measurements for 12 Planets in Eight Systems

Joseph M. Akana Murphy[1,29], Natalie M. Batalha[1], Nicholas Scarsdale[1], Howard Isaacson[2,3], David R. Ciardi[4],
Erica J. Gonzales[1,29], Steven Giacalone[2], Joseph D. Twicken[5,6], Anne Dattilo[1], Tara Fetherolf[7,30],
Ryan A. Rubenzahl[8,29], Ian J. M. Crossfield[9], Courtney D. Dressing[2], Benjamin Fulton[10], Andrew W. Howard[8],
Daniel Huber[11], Stephen R. Kane[7], Erik A. Petigura[12], Paul Robertson[13], Arpita Roy[14,15], Lauren M. Weiss[16],
Corey Beard[13], Ashley Chontos[11,17,31], Fei Dai[8,18,32], Malena Rice[19,20,21,33], Judah Van Zandt[12], Jack Lubin[13],
Sarah Blunt[8], Alex S. Polanski[9], Aida Behmard[22,29], Paul A. Dalba[1,23,23], Michelle L. Hill[7], Lee J. Rosenthal[8],
Casey L. Brinkman[11], Andrew W. Mayo[2], Emma V. Turtelboom[24], Isabel Angelo[12,25], Teo Močnik[26],
Mason G. MacDougall[12], Daria Pidhorodetska[7], Dakotah Tyler[12], Molly R. Kosiarek[1,29], Rae Holcomb[13],
Emma M. Louden[21], Lea A. Hirsch[27], Emily A. Gilbert[28], Jay Anderson[14], and Jeff A. Valenti[14]

[1] Department of Astronomy and Astrophysics, University of California, Santa Cruz, CA 95064, USA; joseph.murphy@ucsc.edu
[2] Department of Astronomy, University of California, Berkeley, CA 94720, USA
[3] Centre for Astrophysics, University of Southern Queensland, Toowoomba, QLD, Australia
[4] NASA Exoplanet Science Institute-Caltech/IPAC, Pasadena, CA 91125, USA
[5] NASA Ames Research Center, Moffett Field, CA 94035, USA
[6] SETI Institute, Mountain View, CA 94043, USA
[7] Department of Earth and Planetary Sciences, University of California, Riverside, CA 92521, USA
[8] Department of Astronomy, California Institute of Technology, Pasadena, CA 91125, USA
[9] Department of Physics and Astronomy, University of Kansas, Lawrence, KS 66045, USA
[10] NASA Exoplanet Science Institute/Caltech-IPAC, Pasadena, CA 91125, USA
[11] Institute for Astronomy, University of Hawai'i, Honolulu, HI 96822, USA
[12] Department of Physics and Astronomy, University of California, Los Angeles, CA 90095, USA
[13] Department of Physics and Astronomy, University of California, Irvine, CA 92697, USA
[14] Space Telescope Science Institute, Baltimore, MD 21218, USA
[15] Department of Physics and Astronomy, Johns Hopkins University, Baltimore, MD 21218, USA
[16] Department of Physics and Astronomy, University of Notre Dame, Notre Dame, IN 46556, USA
[17] Department of Astrophysical Sciences, Princeton University, Princeton, NJ 08540, USA
[18] Division of Geological and Planetary Sciences, California Institute of Technology, Pasadena, CA, 91125, USA
[19] Department of Physics, Massachusetts Institute of Technology, Cambridge, MA 02139, USA
[20] Kavli Institute for Astrophysics and Space Research, Massachusetts Institute of Technology, Cambridge, MA 02139, USA
[21] Department of Astronomy, Yale University, New Haven, CT 06511, USA
[22] Division of Geological and Planetary Science, California Institute of Technology, Pasadena, CA 91125, USA
[23] SETI Institute, Carl Sagan Center, Mountain View, CA 94043, USA
[24] Department of Astronomy, University of California, Berkeley CA 94720, USA
[25] Mani L. Bhaumik Institute for Theoretical Physics, University of California, Los Angeles, CA 90095, USA
[26] Gemini Observatory/NSF's NOIRLab, Hilo, HI 96720, USA
[27] University of Toronto, Mississauga, ON L5L 1C6, Canada
[28] Jet Propulsion Laboratory, California Institute of Technology, 4800 Oak Grove Drive, Pasadena, CA 91109, USA

Abstract

With JWST's successful deployment and unexpectedly high fuel reserves, measuring the masses of sub-Neptunes transiting bright, nearby stars will soon become the bottleneck for characterizing the atmospheres of small exoplanets via transmission spectroscopy. Using a carefully curated target list and observations from more than 2 yr of APF-Levy and Keck-HIRES Doppler monitoring, the TESS-Keck Survey is working toward alleviating this pressure. Here we present mass measurements for 11 transiting planets in eight systems that are particularly suited to atmospheric follow-up with JWST. We also report the discovery and confirmation of a temperate super-Jovian-mass planet on a moderately eccentric orbit. The sample of eight host stars, which includes one subgiant, spans early-K to late-F spectral types (T_{eff} = 5200–6200 K). We homogeneously derive planet parameters using a joint photometry and radial velocity modeling framework,

[29] NSF Graduate Research Fellow.
[30] UC Chancellor's Fellow.
[31] Henry Norris Russell Fellow.
[32] NASA Sagan Fellow.
[33] Heising-Simons 51 Pegasi b Postdoctoral Fellow.

discuss the planets' possible bulk compositions, and comment on their prospects for atmospheric characterization.

Unified Astronomy Thesaurus concepts: Exoplanets (498); Radial velocity (1332)

Supporting material: machine-readable table

1. Introduction

The Kepler spacecraft (Borucki et al. 2010) taught us about the Milky Way's intrinsic planet radius distribution for planets interior to 1 au (Howard et al. 2012; Batalha et al. 2013; Fressin et al. 2013; Petigura et al. 2013; Fulton et al. 2017; Bryson et al. 2021). However, the long-stare, single-field nature of the survey precluded ground-based Doppler mass measurements for all but the brightest host stars. NASA's TESS mission (Ricker et al. 2014), on the other hand, with its detections of transiting exoplanets orbiting bright, nearby stars across the full sky, is allowing us to better understand the observed exoplanet mass and radius distribution. Of particular interest to theories of planet formation and evolution are the masses of sub-Neptunes, whose seeming diversity in bulk density has challenged our post-Kepler interpretations of small planet formation and evolution (e.g., Luque & Pallé 2022). Thus far, TESS is responsible for discovering nearly 100 planets smaller than 4 $R_\oplus$ that also have robust mass measurements.[34]

Measurements of atmospheric properties are key to understanding the interior composition of sub-Neptunes (Rogers & Seager 2010) as they lie at the confluence of theoretical isocomposition curves in the mass–radius plane (Valencia et al. 2007; Adams et al. 2008; Zeng et al. 2019; Otegi et al. 2020). Constraints of atmospheric composition can also inform theories of their formation and evolution histories (e.g., Madhusudhan 2019 and references therein; Kite et al. 2020). For these reasons, transit spectra of sub-Neptunes are extremely valuable. However, precise knowledge of the planets' surface gravities is required in order to interpret these data due to the degeneracy between surface gravity and atmospheric mean molecular weight (Batalha et al. 2019). Space-based transit photometry delivers precise planet radii, making planet mass the dominant source of uncertainty in the surface gravity calculation. Therefore, precise mass measurements and the substantial investments of ground-based resources that they require remain the critical first step in the effort to understand the physical drivers of sub-Neptune diversity.

1.1. The TESS-Keck Survey: Planet Atmospheres

The TESS-Keck Survey (TKS; Chontos et al. 2022), a multisemester Doppler monitoring campaign of promising TESS planet candidates with the Keck-HIRES and APF-Levy spectrographs, is working to provide the precise planet mass measurements required by future efforts in atmospheric characterization, among other investigations (e.g., Lubin et al. 2022; Scarsdale et al. 2021). TKS science falls along four main axes: (1) planet bulk composition, (2) system architectures and dynamics, (3) planet atmospheres, and (4) evolved systems. The systems presented in this work were all observed as members of science case three (SC3), planet atmospheres.

The goal of the TKS SC3 program is to measure precise masses for transiting planets in TESS systems that are particularly amenable to atmospheric follow-up. The SC3 target list was constructed using input from a quantitative selection function in addition to hand-tuning based on results from the TESS Follow-up Observing Program (TFOP; e.g., a target would be dropped despite a favorable selection function value if reconnaissance spectroscopy revealed the system to be an eclipsing binary).[35] Details of the target selection procedure can be found in Scarsdale et al. (2021) and Chontos et al. (2022). The latter contains the complete TKS target list.

In short, the quantitative selection function we used to identify potential SC3 targets strikes a balance between favorable prospects for atmospheric characterization and Doppler observing cost. The function is the ratio of a planet candidate's expected transmission spectroscopy metric (TSM; Kempton et al. 2018), a JWST signal-to-noise ratio (S/N) proxy, and the estimated Keck-HIRES exposure time required to achieve a 5σ mass measurement. TSM is defined as

$$\text{TSM} = (\text{scale factor}) \times \frac{R_p^3 T_{eq}}{M_p R_*^2} \times 10^{-J/5}, \quad (1)$$

where "scale factor" is a normalization constant that depends on planet radius,

$$\text{scale factor} = \begin{cases} 0.19 & \text{for } R_p < 1.5\ R_\oplus \\ 1.26 & \text{for } 1.5 < R_p < 2.75\ R_\oplus \\ 1.28 & \text{for } 2.75 < R_p < 4\ R_\oplus \\ 1.15 & \text{for } 4 < R_p < 10\ R_\oplus. \end{cases}$$

R_p and M_p are in Earth units, T_{eq} is in kelvin (and assumes zero Bond albedo and full day–night heat redistribution), R_* is in solar units, and J is the host star's apparent magnitude in the J band. The scale factor values account for all unit conversions. Since TSM depends on planet mass, we used the mass–radius relation from Chen & Kipping (2017) to translate planet radius values from the TESS object of interest (TOI) catalog (Guerrero et al. 2021) into preliminary mass estimates. The Keck-HIRES exposure time required to achieve a 5σ mass measurement was estimated using the methods in Plavchan et al. (2015). A high value for this ratio indicates a more favorable target.

In order to encourage a sample of planets that was spread evenly over parameter space, TOIs were divided into bins in stellar T_{eff}, planet radius, and planet instellation flux. Selection function values for planets in the same T_{eff}–R_p–S_p bin were compared against one another. The top five highest-ranking planets in each bin were then considered as candidates for the final TKS SC3 target list. Though our binning technique attempted to select a sample that spanned a wide range of host

---

Table 1
Summary of 2 Minute Cadence TESS Observations

System	Sectors	Observing Start/End (UT)
HIP 8152	3, 30	2018 Sep 20/2020 Oct 21
HD 42813	6, 33	2018 Dec 11/2021 Jan 13
HD 25463	5, 32, 43, 44	2018 Nov 15/2021 Nov 6
TOI-669	9, 35	2019 Feb 28/2021 Mar 7
HD 135694	(14 total)	2019 Jul 18/2023 Jan 18
HIP 9618	17, 42, 43	2019 Oct 7/2021 Oct 12
HD 6061	17, 57	2019 Oct 7/2022 Oct 29
TOI-1736	(6 total)	2019 Nov 2/2022 Dec 23

Note. According to data available on MAST as of 2023 March 7. Systems are listed in order of increasing TOI number, starting with HIP 8152 (TOI-266). The start and end dates of the TESS observing baseline are listed in the "Observing start/end" column, but the systems were not necessarily observed continuously during this period. HD 135694 has 2 minute cadence TESS light curves from a total of 14 sectors: 14, 15, 16, 20, 21, 22, 26, 40, 41, 47, 49, 53, 56, and 60. TOI-1736 has 2 minute cadence TESS light curves from a total of six sectors: 18, 19, 25, 52, 58, and 59.

star T_{eff}, since Keck-HIRES is not optimized for observing cooler stars,[36] our final SC3 target list comprises primarily planets orbiting G dwarfs. Our target list also focuses on sub-Neptunes since they offer reasonable expected Doppler observing costs (compared to super-Earths) but are still not giant planets, for which the literature already contains numerous atmospheric measurements.

At the start of the survey in 2019B, we identified 20 TESS systems with at least one high-value planet candidate for atmospheric characterization according to our sample selection procedure. After more than 2 yr of Doppler monitoring, the majority of these systems are now either already published, e.g., HD 63935 (Scarsdale et al. 2021), HD 191939 (Lubin et al. 2022), or the subject of publications in preparation by TKS collaborators. The eight systems presented in this work constitute the remaining systems of the TKS SC3 target list.

1.2. Targets in This Work

In order of increasing TOI number, the systems presented in this work are as follows:

1. HIP 8152 (TOI-266): a G dwarf hosting two sub-Neptunes.
2. HD 42813 (TOI-469): an early-K dwarf hosting one sub-Neptune.
3. HD 25463 (TOI-554): a late-F dwarf hosting a sub-Neptune and a super-Earth on opposite sides of the radius valley (Fulton et al. 2017; Van Eylen et al. 2018).
4. TOI-669: a G dwarf hosting one sub-Neptune.
5. HD 135694 (TOI-1247): an early-K dwarf hosting one sub-Neptune.
6. HIP 9618 (TOI-1471): a G dwarf hosting two sub-Neptunes, each with $P > 20$ days. The system is also host to a massive, distant companion as seen by a linear trend

in the radial velocities. The nature of the companion is uncertain.
7. HD 6061 (TOI-1473): an early-G dwarf hosting one sub-Neptune. The host star also appears to be gravitationally bound to a mid-M dwarf companion (TIC 600433892). The two stars have a sky-projected separation of about 200 au.
8. TOI-1736: a slightly evolved G star hosting one sub-Neptune and one nontransiting, super-Jovian-mass planet on a moderately eccentric orbit. The system is also host to a massive, distant companion as seen by a linear trend in the radial velocities. The nature of the companion is uncertain.

Why are these systems attractive targets for atmospheric observations? While not every planet presented here has an extraordinarily high TSM value—Kempton et al. (2018) suggested that "good" targets for atmospheric characterization have TSM >50, which is not true for three of the 11 transiting planets in this work—Batalha et al. (2023) made it clear that the most informative samples for inferring population-level characteristics are not necessarily composed of the best individual targets for atmospheric characterization. Furthermore, Batalha et al. (2023) noted that planets are often chosen for Doppler and subsequent atmospheric follow-up because they are extreme in some way. This novelty bias systematically disfavors planets that are in fact the Galaxy's most common products of planet formation. To this end, six of the 11 transiting planets presented here land on the mode of the sub-Neptune mass–radius distribution. As noted above, the majority of the planets in the TKS SC3 program orbit G dwarfs, stellar hosts that are currently underrepresented in the set of atmospheric targets for JWST, as much focus remains on small planets orbiting cool stars.[37] Finally, this work presents a large sample of planets with homogeneously derived physical properties, mitigating the effects of potential systematic biases from the data analysis. We discuss the planets' prospects for atmospheric characterization further in Section 13.

The paper is organized as follows: We summarize the TESS 2 minute cadence observations in Section 2. We present high-resolution imaging of the host stars in Section 3 and describe our stellar characterization in Section 4. We discuss our Doppler observations and data reduction in Section 5. We discuss our light curve inspection, cleaning, and initial transit modeling in Section 6. We search for radial velocity trends and nontransiting companions in Section 7. We examine stellar activity in Section 8. In Section 9 we describe our joint photometry, radial velocity, and stellar activity modeling framework. We present the results of this modeling in Section 10. In Section 12 we discuss possible bulk compositions for the planets and place them in the mass–radius diagram. In Section 13 we discuss the planets' prospects for atmospheric characterization. We conclude in Section 14. We note that the times of observations labeled in Barycentric Julian Date (BJD) or Barycentric TESS Julian Date (BTJD; BTJD = BJD − 2457000; i.e., the TESS and Doppler

---

[36] Keck-HIRES measures stellar radial velocities using a warm cell of molecular iodine (Butler et al. 1996), which imprints absorption lines on the stellar spectrum between ∼5000 and 6000 Å. Therefore, Keck-HIRES is generally less efficient at measuring the radial velocities of M dwarfs compared to G dwarfs, for example.

[37] While planets transiting cool stars are typically more efficient targets for transmission spectroscopy (owing in part to the larger planet–star radius ratio), the radius distribution of planets orbiting M dwarfs is distinct from that of FGK dwarfs (Dressing & Charbonneau 2013). This implies differences in the dominant channel(s) of planet formation and evolution as a function of stellar properties, and, consequently, that the atmospheric characteristics of planets around M dwarfs may not be representative of planets with Sun-like hosts.

Table 2
Imaging Observations from This Work

System	Instrument	Observation Date (UT)	Filter	t_{exp} (s)	N_{exp}	Resolution (FWHM)	Contrast at $0\rlap{.}''5$ (Δ mag)
HIP 8152	Palomar-PHARO	2018 Dec 22	Br-γ	9.9	15	$0\rlap{.}''11$	6.0
HD 25463	Keck-NIRC2	2020 Sep 9	Br-γ	0.2	9	$0\rlap{.}''05$	7.5
HD 135694	Keck-NIRC2	2020 May 28	Br-γ	1.0	9	$0\rlap{.}''05$	7.0
HD 6061	Keck-NIRC2	2020 May 28	J-cont	1.2	9	$0\rlap{.}''04$	7.0
HD 6061	Keck-NIRC2	2020 May 28	Br-γ	1.5	18	$0\rlap{.}''05$	7.5
HD 6061	Palomar-PHARO	2020 Dec 5	H-cont	1.4	15	$0\rlap{.}''08$	7.1
HD 6061	Palomar-PHARO	2020 Dec 5	Br-γ	1.4	15	$0\rlap{.}''09$	6.7
TOI-1736	Keck-NIRC2	2020 Sep 9	Br-γ	0.5	9	$0\rlap{.}''05$	6.5

Note. J-cont: $\lambda_0 = 1.213$ μm and $\Delta\lambda = 0.020$ μm. H-cont: $\lambda_0 = 1.668$ μm and $\Delta\lambda = 0.018$ μm. Br-γ: $\lambda_0 = 2.169$ μm and $\Delta\lambda = 0.0323$ μm. Systems are listed in order of increasing TOI number.

observations) were measured using the using the Barycentric Dynamical Time standard (TDB; e.g., Eastman et al. 2010).

2. TESS Photometry

Of the 12 planets characterized in this work, 11 are detected in transit by TESS. Table 1 summarizes the 2 minute cadence TESS observations for each system as they were available on the Mikulski Archive for Space Telescopes (MAST) on 2023 March 7 (i.e., up to and including TESS Sector 60). Each system was observed in at least two sectors, with HD 135694 being observed in 14. The photometry was processed by the TESS Science Processing Operations Center pipeline (SPOC; Jenkins et al. 2016). All of the TESS data used in this paper can be found in MAST:10.17909/y06k-3f04.

For all of our targets, there are no individual sources from Gaia Data Release 3 (DR3; Gaia Collaboration et al. 2016, 2023) within $20''$ that cause >1% dilution, nor does the combined flux of all DR3 sources within that radius cause >1% dilution for any target. Furthermore, the SPOC data products we use are already corrected for dilution from Gaia sources per Gaia DR2 (Gaia Collaboration et al. 2018). In Section 3 we present high-resolution imaging observations that rule out significant dilution from unresolved companions.[38] We discuss our light curve inspection and cleaning in Section 6 and our transit modeling in Section 9.1.

3. High-resolution Imaging

To ensure that the planet transits were not subject to dilution from sources not resolved by Gaia, we used high-resolution imaging (HRI) to place contrast limits on potential nearby companions. HD 42813, TOI-669, and HIP 9618 all have high-resolution images in the literature that rule out dilution from nearby companions. We summarize the results of these observations in Section 3.1. For the remaining five systems, HIP 8152, HD 25463, HD 135694, HD 6061, and TOI-1736, we present new observations from Palomar-PHARO (Hayward et al. 2001) and Keck-NIRC2 (Wizinowich et al. 2000). The Palomar-PHARO and Keck-NIRC2 observations were obtained under the programs of PIs D. R. Ciardi and E. J. Gonzales, respectively. A summary of the imaging

observations from this work can be found in Table 2, and sensitivity curves are shown in Figure 1.

3.1. Literature Observations

HD 42813 and TOI-669 have Keck-NIRC2 observations from Schlieder et al. 2021. HD 42813 was observed with Keck-NIRC2 on 2019 March 25 using the narrowband Br-γ filter ($\lambda_0 = 2.169$ μm and $\Delta\lambda = 0.032$ μm) and an integration time of 30 s. The star appears single and the Keck-NIRC2 observation rules out companions of Δ7.4 mag at 5σ confidence at a separation of $0\rlap{.}''5$. The TOI-669 Keck-NIRC2 observation was taken on 2019 June 9 using the K filter ($\lambda_0 = 2.196$ μm and $\Delta\lambda = 0.336$ μm) and an integration time of 10 s. The star appears single, and the Keck-NIRC2 observation rules out companions of Δ7.6 mag at 5σ confidence at a separation of $0\rlap{.}''5$.

Osborn et al. (2023) reported the discovery and confirmation of HIP 9618 b and c using space-based photometry from TESS and CHEOPS (Benz et al. 2021) along with radial velocity observations from CAFE, HARPS-N, and SOPHIE (Perruchot et al. 2008; Cosentino et al. 2012; Aceituno et al. 2013). To rule out dilution from nearby sources, the authors observed HIP 9618 with a variety of optical speckle and near-infrared (NIR) adaptive optics (AO) instruments, including Keck-NIRC2. The HRI shows no evidence of stellar companions within $1''$.

3.2. Palomar-PHARO and Keck-NIRC2 Observations

3.2.1. HIP 8152 (TOI-266)

Palomar Observatory HRI observations of HIP 8152 were made with the PHARO instrument on the 5.1 m Hale telescope. Palomar-PHARO has a pixel scale of $0\rlap{.}''025$ pix^{-1} for a total field of view of about $25''$. Observations of HIP 8152 were taken on 2018 December 22 in the narrowband Br-γ filter. Observations were acquired using the natural guide star AO system P3K (Dekany et al. 2013) in the standard five-point `quincunx` dither pattern with steps of $5''$. Each dither position was observed three times, with $0\rlap{.}''5$ positional offsets between each observation, for a total of 15 frames. For HIP 8152, each frame had an integration time of 9.9 s, amounting to a total on-source time of 149 s. No stellar companions were detected.

3.2.2. HD 25463 (TOI-554)

Keck Observatory HRI observations of HD 25463 were made with the NIRC2 instrument on the 10 m Keck II telescope. Keck-NIRC2 was used in the narrow-angle mode

---

[38] The results of TFOP imaging data, in addition to the results of other reconnaissance observations, were used to inform TKS target selection, as acknowledged by Chontos et al. (2022). This paper formally reports the results of imaging observations of targets without such data already in the literature.
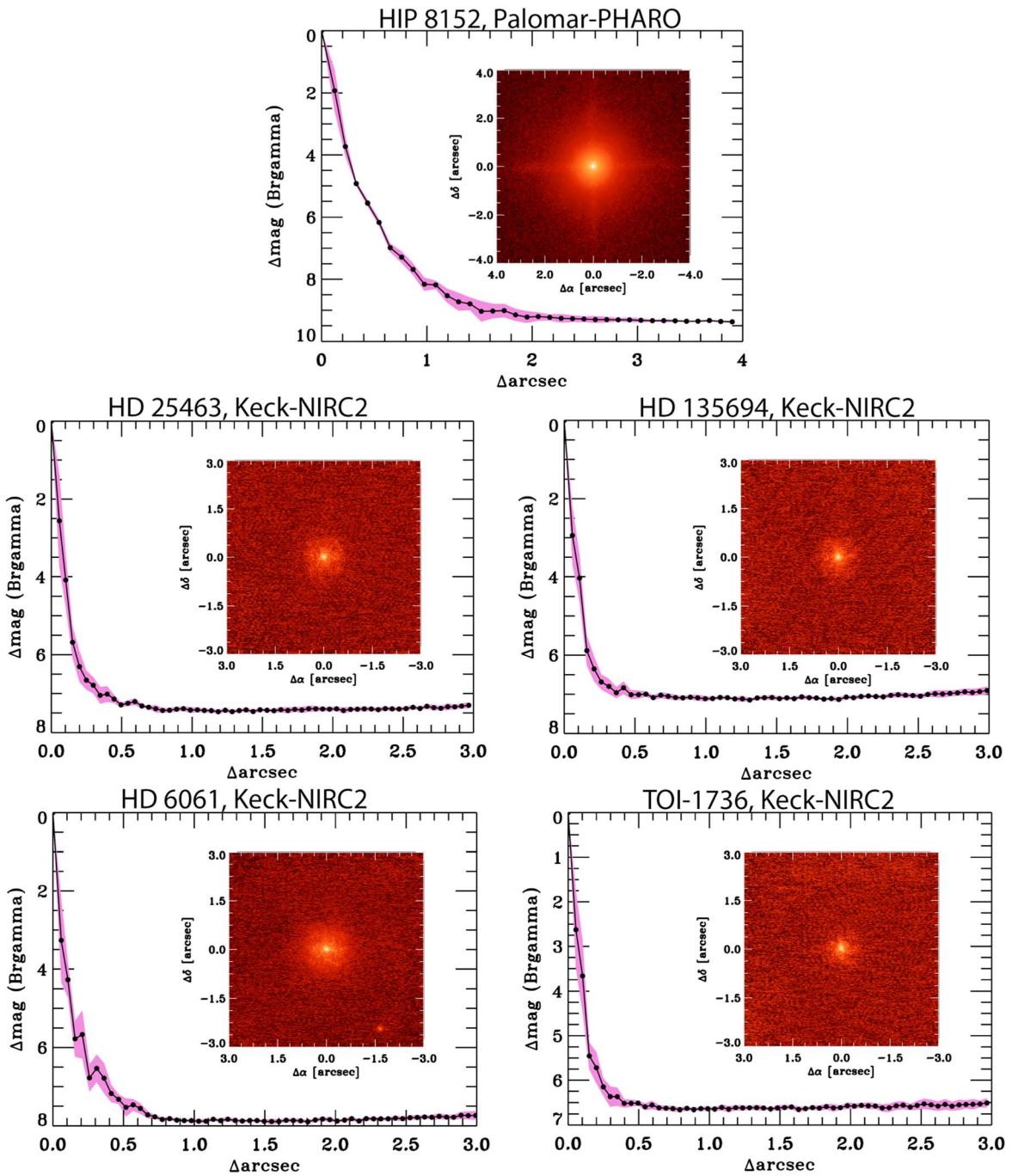
Figure 1. AO imaging results for HIP 8152, HD 25463, HD 135694, HD 6061, and TOI-1736 from our observations with Palomar-PHARO and Keck-NIRC2. Contrast curves are shown in black with 1σ error envelopes in purple. The images themselves are shown as the postage stamp insets. HIP 8152, HD 25463, HD 135694, and TOI-1736 all appear single. Keck-NIRC2 observations of HD 6061 were taken in both Br-γ and J-cont, but only the former is shown here. In the image of HD 6061, TIC 600433892 can be seen in the lower-right corner at a separation of $\approx 3''$. TIC 600433892 is fainter than HD 6061 by 6.2 mag in the TESS bandpass, meaning that its dilution of HD 6061 b's transits is about a 0.1% effect (i.e., much less than the uncertainty on the stellar radius). HD 6061 and TIC 600433892 have consistent distances and proper motions according to Gaia DR3, meaning that the two stars are almost certainly gravitationally bound. At a distance of 67 pc, their on-sky separation of $3''$ translates to a sky-projected separation of about 200 au.

with a pixel scale of approximately $0''01$ pix^{-1} and a full field of view of about $10''$. Observations of HD 25463 were taken on 2020 September 9 in the narrowband Br-γ filter. Observations were acquired using the natural guide star AO system in the standard three-point dither pattern to avoid the lower-left quadrant of the detector, which is typically noisier than the other three quadrants. The dither pattern has a step size of $3''$. Each dither position was observed three times, with $0''5$

positional offsets between each observation, for a total of nine frames. For HD 25463, each frame had an integration time of 0.2 s, amounting to a total on-source time of 1.8 s. No stellar companions were detected.

3.2.3. HD 135694 (TOI-1247)

Keck-NIRC2 observations of HD 135694 were taken on 2020 May 28 following the methods described in Section 3.2.2.

Images were taken in the narrowband Br-γ filter. Each frame had an integration time of 1.0 s, amounting to a total on-source time of 9 s. No stellar companions were detected.

3.2.4. HD 6061 (TOI-1473)

Keck-NIRC2 observations of HD 6061 were taken on 2020 May 28 following the methods described in Section 3.2.2. Images were taken in both the *J*-continuum ($\lambda_0 = 1.213$ μm and $\Delta\lambda = 0.020$ μm) and Br-γ narrowband filters. Observations of HD 6061 were taken in multiple filters due to the visual observation of a nearby diluting source (TIC 600433892, separation of $\approx 3''$) in order to further ascertain colors and the likelihood of the nearby stellar object being bound. For the Br-γ observations, six images were taken at each dither position, for a total of 18 frames. Each frame had an integration time of 1.2 s in *J*-cont and 1.5 s in Br-γ, amounting to a total on-source time of 11 s in *J*-cont and 27 s in Br-γ.

HD 6061 was also observed with Palomar-PHARO on 2020 December 5 following the methods described in Section 3.2.1. HD 6061 was observed in both the Br-γ and *H*-continuum ($\lambda_0 = 1.668$ μm and $\Delta\lambda = 0.018$ μm) narrowband filters. Each frame (in both Br-γ and *H*-cont) had an integration time of 1.4 s, amounting to a total on-source time of 21 s in each filter. We discuss the nature of the stellar companion in Section 3.4. Other than TIC 600433892, no other stellar companions were detected.

3.2.5. TOI-1736

Keck-NIRC2 observations of TOI-1736 were taken on 2020 September 9 following the methods described in Section 3.2.2. Images were taken in the narrowband Br-γ filter. Each frame had an integration time of 0.5 s, amounting to a total on-source time of 4.5 s. No stellar companions were detected.

3.3. Palomar-PHARO and Keck-NIRC2 Reduction

Both the Palomar-PHARO and the Keck-NIRC2 data were reduced using the same methods. The science frames were flat-fielded and sky-subtracted. The flat fields were generated from a median average of dark subtracted flats taken on-sky. The flats were normalized such that the median value of the flats is unity. The sky frames were generated from the median average of the dithered science frames; each science image was then sky-subtracted and flat-fielded. The reduced science frames were combined into a single coadded image using an intrapixel interpolation that conserves flux, shifts the individual dithered frames by the appropriate fractional pixels, and median-coadds the frames. The final resolutions of the combined dithers were determined from the FWHM of the point-spread functions (PSFs) in the corresponding filter.

The sensitivities of the final combined AO image were determined by injecting simulated sources azimuthally around the primary target every $20°$ at separations of integer multiples of the central source's FWHM (Furlan et al. 2017). The brightness of each injected source was scaled until standard aperture photometry detected it with 5σ significance. The resulting brightness of the injected sources relative to each target set the contrast limits at that injection location. The final 5σ limit at each separation was determined from the average of all of the determined limits at that separation. The uncertainty on the limit was set by the rms dispersion of the azimuthal slices at a given radial distance. The final sensitivity curves are
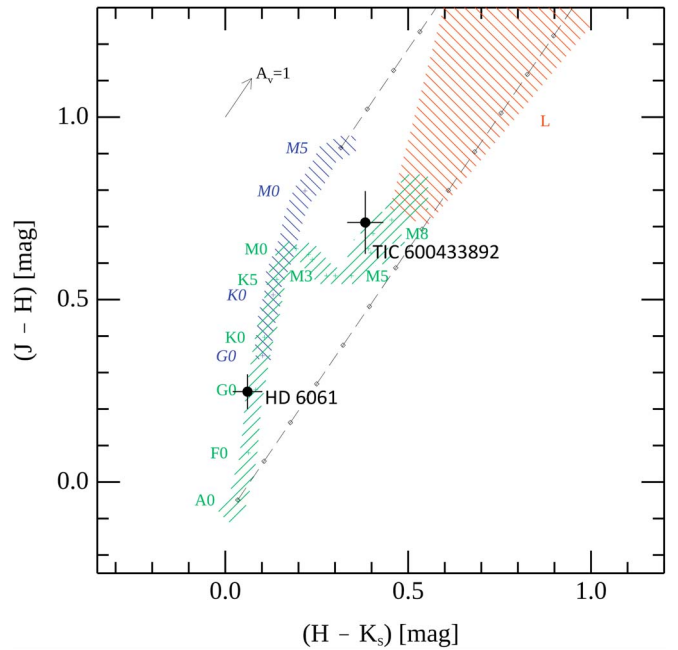

Figure 2. A 2MASS *JHK$_s$* color–color diagram. The dwarf branch, giant branch, and brown dwarf loci are shown with green, blue, and red hashes, respectively. Black dashed lines represent the direction of reddening induced by extinction (A_V). HD 6061 and TIC 600433892 are overplotted as the black circles with 1σ error bars. TIC 600433892 is consistent with being an M4/5V dwarf. We find that HD 6061 is consistent with being a G0 dwarf, which agrees with the classification from Cannon & Pickering (1993).

shown in Figure 1. For all targets, no stellar companions were detected within $1''$.

3.4. TIC 600433892: A Stellar Companion to HD 6061

HD 6061 was observed in multiple filters with both Keck-NIRC2 and Palomar-PHARO due to the presence of a nearby stellar companion. In Br-γ, the companion, TIC 600433892, has a separation of $3''06 \pm 0''20$ and a position angle of $213° \pm 1°$ E of N. TIC 600433892 is fainter than HD 6061 by 6.2 mag in the TESS bandpass, meaning that its dilution of HD 6061 b's transits, approximately a 0.1% effect, is negligible. According to Gaia DR3, HD 6061 and TIC 600433892 have consistent distances to 1σ (67.69 ± 0.07 pc and 66.3 ± 1.4 pc, respectively) and consistent proper motions to 3σ ($\mu_\alpha = -9.72 \pm 0.01$ mas yr^{-1} and $\mu_\delta = -10.09 \pm 0.01$ mas yr^{-1} for HD 6061, $\mu_\alpha = -10.7 \pm 0.5$ mas yr^{-1} and $\mu_\delta = -10.6 \pm 0.2$ mas yr^{-1} for TIC 600433892). This implies that the two stars are almost certainly gravitationally bound. At a distance of 67 pc, $3''$ translates to a sky-projected separation of about 200 au.

Following the methods of Ciardi et al. (2018), relative photometry was conducted on the Keck-NIRC2*J*-cont image and the Palomar-PHARO*H*-cont and Br-γ images to deblend the infrared magnitudes of the two stars (where Br-γ is taken to have a central wavelength that is sufficiently close to K_s). The resulting Two Micron All Sky Survey (2MASS; Skrutskie et al. 2006) *JHK$_s$* color–color diagram suggests that TIC 600433892 is an M4/5V dwarf (Figure 2). Following the reasoning in Ciardi et al. (2018), it is unlikely that TIC 600433892 is a heavily reddened ($A_V > 6$ mag using an $R = 3.1$ extinction law) early-F or late-A background star, given that the entire line-of-sight extinction through the Galaxy is only $A_V \approx 2$ mag (Schlafly & Finkbeiner 2011).

Table 3
Keck-HIRES Template Observations

System	Date (UT)	t_{exp} (s)	Decker	Airmass	S/N (pix^{-1})	N_{exp}
HIP 8152	2019 Aug 18	476	B3	1.34	210	1
HD 42813	2019 Oct 31	314	B1	1.21	217	2
HD 25463	2019 Aug 18	26	B3	1.52	200	3
TOI-669	2020 Jan 04	1692	B3	1.28	214	1
HD 135694	2020 Mar 9	180	B1	1.66	211	2
HIP 9618	2020 Jan 30	263	B3	1.42	210	2
HD 6061	2019 Dec 28	180	B3	1.15	213	2
TOI-1736	2020 Aug 11	187	B3	1.59	211	1

Note. B1 decker: $3{\rlap{.}''}5 \times 0{\rlap{.}''}574$, $R = 60,000$. B3 decker: $14'' \times 0{\rlap{.}''}574$, $R = 60,000$. S/N measured at 5500 Å. $N_{exp} > 1$ means that consecutive exposures were taken and then combined to produce the final template spectrum. For these cases, the t_{exp}, airmass, and S/N reported in this table are the median values across the N_{exp} observations. All template observations were acquired with a moon separation of $>30°$.

4. Determination of Stellar Properties

4.1. Stellar Template Observations

We used the High Resolution Echelle Spectrometer (HIRES; Vogt et al. 1994) on the 10 m Keck I telescope at the W. M. Keck Observatory on Maunakea to obtain iodine-free spectra of each system at high resolution and S/N, which were used to produce a deconvolved stellar spectral template (DSST) for each host. The exposure parameters for each template are summarized in Table 3. Triple-shot exposures of rapidly rotating B stars were taken with the iodine cell in the light path immediately before and after the high-resolution templates were collected in order to precisely constrain the instrumental PSF. The data collection and reduction followed the methods of the California Planet Search (CPS) as described in Howard et al. (2010).

4.2. Stellar Characterization

We performed an initial stellar characterization of each host star using SpecMatch-Emp (Yee et al. 2017) to constrain stellar effective temperature (T_{eff}), metallicity ([Fe/H]), and stellar radius (R_*) directly from the iodine-free Keck-HIRES template spectra. SpecMatch-Emp fits stellar spectra between 5000 and 5800 Å in 100 Å segments using a linear combination of spectral templates from a library of over 400 precisely characterized FGKM stars.

To estimate the posteriors of the fundamental stellar parameters, we used isoclassify (Huber et al. 2017; Berger et al. 2020) in grid mode with the allsky dust map, which is an extinction model obtained via a combination of the models from Drimmel et al. (2003), Marshall et al. (2006), and Green et al. (2019). isoclassify infers marginal posteriors for stellar properties by integrating over a grid of MIST isochrones (Choi et al. 2016). To inform the isoclassify analysis, we input priors stemming from our SpecMatch-Emp results, parallaxes from Gaia DR3, and 2MASS JHK_s magnitudes.[39] Following Tayar et al. (2022), to account for model-dependent systematic uncertainties, we inflated the errors on each host star's mass and radius by adding an

additional 5% and 4% uncertainty, respectively, in quadrature with the measurement error reported by isoclassify. The final stellar parameters are summarized alongside planet parameters in Appendix A.

5. Doppler Follow-up

5.1. Keck-HIRES

We obtained high-resolution spectra of each target with Keck-HIRES to measure precise radial velocities (RVs). RVs were determined following the procedures of Howard et al. (2010). In brief, a warm cell of molecular iodine was placed at the entrance slit during the RV observations (Butler et al. 1996). The superposition of the iodine absorption lines on the stellar spectrum provides both a fiducial wavelength solution and a precise, observation-specific characterization of the instrument's PSF. As part of a forward model, the spectrum is divided into about 700 pieces between ∼5000 and 6000 Å, with each piece being 2 Å in width. For each piece, the product of the DSST and the Fourier Transform Spectrograph iodine spectrum is convolved with the PSF to match the iodine-in observation. As one of the free parameters, an RV for each piece of spectrum is produced. The pieces are weighted using all observations of the star to produce a single RV for each observation. Our Keck-HIRES Doppler observations are summarized in Table 4, and the RV measurements can be found in Table 5.

5.2. APF-Levy

5.2.1. Data Reduction and Cleaning

For the brighter targets in our sample ($V < 9.25$ mag), we also obtained high-resolution spectra with the Levy spectrograph mounted on the 2.4 m Automated Planet Finder telescope (APF; Vogt et al. 2014) at Lick Observatory on Mt. Hamilton near San José California. Though mounted on a much smaller telescope, APF-Levy is complementary to Keck-HIRES in both latitude and observing cadence. In the case of TOI-1736, APF-Levy observed periastron passage for the giant planet (TOI-1736 c) while the system was inaccessible from Maunakea. With its queue-based observing schedule and lower oversubscription rate compared to Keck, APF-Levy can also typically observe targets with higher cadence than Keck-HIRES.

The standard reduction pipeline used to compute RVs from APF-Levy spectra follows the methods of Howard et al. (2010). As with our Keck-HIRES observations, spectra were obtained with a warm cell of molecular iodine in the light path. We used the Keck-HIRES DSSTs to compute RVs instead of acquiring independent iodine-free template spectra with APF-Levy. Keck-HIRES DSSTs have been shown to serve as effective replacements for APF-Levy templates in the CPS Doppler reduction pipeline (e.g., Dai et al. 2020; MacDougall et al. 2021; Dalba et al. 2022; Lubin et al. 2022) and provide an efficient alternative to the long exposures that would otherwise be required to achieve similar S/N on an iodine-free APF-Levy template.

To avoid using low-quality APF-Levy RVs in our analysis, for each system we inspected the distribution of APF-Levy RV errors as a function of S/N at 5500 Å. We placed a conservative maximum RV error threshold of three times the median RV error for each target. Observations that landed

---

[39] In the case of HD 6061, the 2MASS JHK_s magnitudes were deblended to account for the flux from TIC 600433892 (see Section 3.4).

Table 4
Summary of RV Observations

System	Instrument	First/Last Observation (UT)	N RVs (unbinned)	Median t_{exp} (s)	Median S/N (pix^{-1})	Typical Decker
HIP 8152	Keck-HIRES	2019 Aug 14/2022 Jul 25	94 (94)	683	213	C2
HD 42813	Keck-HIRES	2019 Sep 17/2022 Feb 22	71 (71)	429	219	B5
HD 25463	Keck-HIRES	2019 Aug 14/2022 Feb 22	97 (265)	37	213	B5
	APF-Levy	2019 Aug 2/2020 Nov 16	124 (152)	592	108	W
TOI-669	Keck-HIRES	2019 Nov 7/2021 Nov 24	61 (62)	897	150	C2
HD 135694	Keck-HIRES	2020 Jan 4/2022 Jul 9	79 (80)	295	214	B5
	APF-Levy	2019 Oct 25/2023 Jan 31	117 (150)	1200	68	W
HIP 9618	Keck-HIRES	2020 Jan 21/2022 Jul 25	61 (61)	290	214	B5
	APF-Levy	2020 Feb 19/2022 Nov 28	127 (206)	1800	80	W
HD 6061	Keck-HIRES	2019 Dec 16/2021 Aug 30	64 (64)	205	212	B5
	APF-Levy	2020 Jan 3/2022 Nov 22	56 (69)	1200	69	W
TOI-1736	Keck-HIRES	2020 Aug 2/2022 Jan 19	77 (79)	226	203	B5
	APF-Levy	2021 Feb 18/2023 Jan 28	257 (282)	1800	85	W

Note. RVs are binned by 8 hr. Keck-HIRES B5 decker: $3{''}5 \times 0{''}861$, $R = 45{,}000$. Keck-HIRES C2 decker: $14'' \times 0{''}574$, $R = 45{,}000$. APF-Levy W decker: $1'' \times 3''$, $R = 95{,}000$. S/N is measured at 5500 Å. All observations were acquired with a moon separation of $>30°$.

Table 5
Radial Velocities and S_{HK} Values

System Name	Time (BJD)	RV (m s^{-1})	RV Unc. (m s^{-1})	S_{HK}	S_{HK} Unc.	Inst.
HIP 8152	2458710.099141	−4.38	1.41	0.164	0.002	HIRES
...	...	...	...	...	...	...

Note. The RV and S_{HK} measurements presented in this paper. Only the first row of the table (which is sorted by system and then by observation date) is shown here to inform its contents and format. BJD is reported using the TDB standard (e.g., Eastman et al. 2010). Model-specific instrumental offsets have not been applied to the RV values. The RV errors listed here represent measurement uncertainty and have not been added in quadrature with the corresponding instrument jitter values resulting from our models of the data (see Appendix A). This table is available in its entirety online in machine-readable format.

(This table is available in its entirety in machine-readable form.)

above the error threshold were removed, and the APF-Levy RVs were recomputed using the cleaned data set. For HD 135694, this resulted in removing four APF-Levy spectra, all with $\sigma_{RV} > 6.3$ m s^{-1}. For HIP 9618, we removed six spectra, all with $\sigma_{RV} > 5.8$ m s^{-1}. For HD 6061, we removed three spectra, all with $\sigma_{RV} > 21.9$ m s^{-1}. For TOI-1736, we removed 13 spectra, all with $\sigma_{RV} > 6.6$ m s^{-1}. The APF-Levy Doppler observations used in our analysis are summarized in Table 4, and the RV measurements can be found alongside the Keck-HIRES RVs in Table 5.

5.2.2. The Case of HD 25463

For one system, HD 25463, the reduction methods we used to measure velocities from the APF-Levy spectra were slightly different from the methods of Howard et al. (2010) due to the star's rapid rotation (for HD 25463, we measure a sky-projected stellar rotational velocity of $v \sin i_* = 11.6 \pm 1.0$ km s^{-1} using SpecMatch-Syn; Petigura et al. 2017). For ease of reference, we will refer to the methods in Howard et al. (2010) as the "default" reduction pipeline. To measure the radial velocity of a star from a spectrum, the default Doppler pipeline breaks the spectrum into small chunks and fits stellar absorption lines chunk-by-chunk. The size of each chunk is determined by a fixed pixel width. For Keck-HIRES, this pixel width translates to a chunk width of about 2 Å in wavelength space. However, because APF-Levy has higher spectral

resolution than Keck-HIRES, this fixed pixel width translates to a smaller chunk width in wavelength space. For reference, the W decker on APF-Levy has $R = 95{,}000$ (Vogt et al. 2014) while the B5 decker on Keck-HIRES has $R = 45{,}000$ (Vogt et al. 1994), where these deckers are typical for observations of HD 25463. Using the default Doppler reduction pipeline on APF-Levy spectra therefore results in less spectral information being contained in each chunk than when it is applied to Keck-HIRES spectra.

This difference in the wavelength space width of each chunk is typically not an issue for inactive, slowly rotating stars (as is evident in the consistency between the APF-Levy and Keck-HIRES RVs for a representative system such as HIP 9618). However, for more rapid rotators ($v \sin i_* \gtrsim 10$ km s^{-1}), line broadening can conspire with the smaller chunk width to cause catastrophic errors in the APF-Levy RV measurement process. This failure happens because single stellar absorption lines become too broad to fit within a single chunk. We observe this failure mode for HD 25463 when trying to measure RVs from the APF-Levy spectra via the default method. To circumvent this failure, for HD 25463's APF-Levy spectra we compute RVs by fitting entire echelle orders simultaneously instead of fitting small chunks in series. This method also does not depend on an iodine-free template spectrum. Instead, we simultaneously solve for the stellar template using all of the iodine-in spectra. Save for these changes, the rest of the reduction is similar to the default method.

We refer to this alternative method of computing the APF-Levy RVs as the `iGrand` method. For completeness, Appendix B contains figures comparing the default APF-Levy RVs to the `iGrand` RVs for HD 25463. It is clear that the default APF-Levy RVs are inconsistent with the contemporaneous Keck-HIRES measurements (the default APF-Levy RVs show nearly 100 m s^{-1} of scatter). In contrast, the spread and uncertainties of the `iGrand` velocities are more in line with expectations for a star of this magnitude ($V = 6.9$ mag) and spectral type ($T_{eff} = 6200$ K).

As we did for the other targets that were observed with APF-Levy, we removed low-quality APF-Levy spectra of HD 25463 by setting a maximum RV error threshold of three times the median APF-Levy `iGrand` RV error. This resulted in removing 10 APF-Levy spectra, all with $\sigma_{RV} > 18.8$ m s^{-1}.

6. Light Curve Inspection and Cleaning

Before applying our joint analysis of the photometry and RVs, we first inspected and cleaned the TESS data. Using `lightkurve` (Lightkurve Collaboration et al. 2018), we downloaded all of the TESS Presearch Data Conditioning Simple Aperture Photometry (PDCSAP; Smith et al. 2012; Stumpe et al. 2012, 2014) 2 minute cadence data for each target, excluding data with `NaN` values or data quality flags. We then normalized the data on a sector-by-sector basis. We also applied the following analysis to the simple aperture photometry (SAP; Twicken et al. 2010; Morris et al. 2020) light curves for each target. While the best-fitting transit parameters were nearly identical between fits to the PDCSAP and SAP data, we generally found the SAP data contained obvious spacecraft systematics and required more outliers to be rejected.

6.1. Transit Search

For each system, we searched for transits in the TESS PDCSAP light curve using the box least-squares method (BLS; Kovács et al. 2002). The signals reported by the SPOC were identified in the transiting planet search pipeline component, which employs an adaptive, noise-compensating matched filter (Jenkins 2002; Jenkins et al. 2010, 2020). We recovered all SPOC-reported signals in the TOI catalog as of 2022 October 4, with a median S/N of 23 across all of our BLS detections and with each detection having S/N $\gtrsim 10$. After recovering the SPOC-reported signals, we masked the planet transits and re-ran our BLS search but failed to find any other candidates.

In the case of TOI-554.02, our BLS search recovers the candidate's shallow transits with a slightly lower significance (S/N ≈ 8), motivating, in part, a more thorough investigation of the purported transit signal (see Section 6.1.1). In addition, there are two instances where we identify transiting planet candidates whose properties disagree with entries in the TOI catalog. These are the so-called "duotransit" planets orbiting HIP 8152 and HIP 9618, which we discuss in Section 6.1.2.

6.1.1. Statistical Validation of TOI-554.02 (HD 25463 c)

In the hierarchy of exoplanet detection, statistical validation is typically an intermediate step taken between planet candidacy and confirmation[40] where astrophysical false-

---

[40] For the purposes of this discussion, we take planet "confirmation" to mean that the planet's mass has been measured to some fiducial precision. For the mass–radius diagram in Figure 10, we show planets from the NASA Exoplanet Archive whose mass measurements have better than 50% fractional precision.

positive scenarios are systematically ruled out (e.g., Borucki et al. 2012; Morton et al. 2016). In the case of transiting planet candidates, validation is used to statistically exclude the possibility that the purported transit signal is in fact, for example, a background eclipsing binary star system. Since most of the transiting planets in this work are at least marginally ($\gtrsim 2.5\sigma$) detected with RVs, we bypass the statistical validation step as the measurement of their host star's Doppler signal confirms their planetary nature. However, in two cases, we measure only an upper limit on the planet mass. The first, HIP 9618 c, was externally validated and confirmed by Osborn et al. (2023) using a combination of TESS and CHEOPS photometry and CAFE, HARPS-N, and SOPHIE RVs (see Section 10.6.2 for details). The second, TOI-554.02 (HD 25463 c) has not yet been confirmed, so we take additional measures to statistically validate this planet.

A new threshold crossing event with $P = 3.04$ days was detected by the transit search of the SPOC Sectors 1–46 2 minute light curve for HD 25463 (a.k.a. TOI-554). An initial limb-darkened transit model was fitted (Li et al. 2019), and a suite of diagnostic tests were conducted to help determine whether or not the signal was planetary in nature (Twicken et al. 2018). The transit signature passed all of the diagnostic tests presented in the SPOC Data Validation reports. The TESS Science Office reviewed the vetting information and issued an alert for TOI-554.02 on 2022 April 20.

The planet candidate is small ($R_p \approx 1.3\ R_{\oplus}$ from the SPOC report), and the pipeline only detects its transit with S/N = 8.5. However, due to the candidate's short orbital period and the system's four sectors of photometry, TESS has observed 29 purported transits. After removing HD 25463 b's transits from the light curve (as identified by our initial BLS search of the system), we re-ran BLS, but TOI-554.02's transit signal was not immediately apparent. We narrowed the BLS period grid to look for signals short of 10 days (down from 100 days) and increased the number of grid points (by a factor of 2). We identified a peak in the BLS power spectrum with S/N ≈ 8 that corresponded to the SPOC-reported signal for TOI-554.02. While each individual transit is not entirely obvious by eye, the phase-folded transit shows a clear decrease in flux. We masked transits associated with TOI-554.02 and re-ran the BLS search but found no additional transit-like events.

As discussed above, since our RV observations only place an upper limit on the mass of TOI-554.02 (see Section 10.3), we independently analyzed the TESS photometry and our Keck-NIRC2 HRI with the planet validation framework `TRICERATOPS` (Giacalone et al. 2021) to rule out astrophysical false-positive scenarios that might be responsible for TOI-544.02's purported transit signal. `TRICERATOPS` validates planets by simulating astrophysical false positives arising from gravitationally bound stellar companions, chance-aligned foreground or background stars, and known nearby stars that are blended with the target in the TESS data. The marginal likelihoods of these false-positive scenarios are calculated and compared to that of the scenario where the signal is caused by a planet transiting the target star. This calculation yields two quantities: the false-positive probability (FPP; the overall probability that the signal is caused by something other than a planet transiting the target star) and the nearby false-positive probability (NFPP; the probability that the signal is caused by a known nearby star that is blended with the target in the TESS data). In order for a planet to be considered validated, it must achieve FPP < 0.015 and NFPP < 0.001. To

account for the intrinsic stochasticity in its calculation, we ran TRICERATOPS 50 times on the same data set, obtaining $FPP = (4.6 \pm 0.2) \times 10^{-4}$ and $NFPP = (5.7 \pm 0.9) \times 10^{-6}$. We find that the dominant contributor to FPP is the STP scenario, which involves a gravitationally bound stellar companion that hosts a transiting planet; however, we note that this scenario is unlikely due to the absence of evidence for a stellar companion in our iodine-free spectra or RV data. Regardless, these values are sufficiently small to consider the planet statistically validated. We also note that these results are independent of the fact that we confirm HD 25463 b using RVs, which makes it even more likely that TOI-554.02 is a true planet (Lissauer et al. 2012; Guerrero et al. 2021). Hereafter, we refer to TOI-554.02 as HD 25463 c.

6.1.2. Duotransit Systems

HIP 8152 (TOI-266) and HIP 9618 (TOI-1471) both host two transiting planets, with the sub-Neptunes HIP 8152 c and HIP 9618 c each having two transits in widely time-separated sectors (these planets constitute a "duotransit" scenario; Osborn et al. 2022). CHEOPS, in tandem with our Keck-HIRES RVs of the systems, recently confirmed the correct period of HIP 8152 c ($P = 19.61$ days; via private communication with the CHEOPS team; point of contact H. Osborn) and HIP 9618 c ($P = 52.56$ days; Osborn et al. 2023). SPOC did not correctly identify the transit signals of these planets in the TESS data. For HIP 8152, TOI-266.02 is spuriously reported with $P = 6.19$ days and $T_c = 1392.10$ BTJD. For HIP 9618, as last updated on 2022 April 20, TOI-1471.02 is listed as having $P = 683.33$ days (the time difference between the transit in Sector 17 and the transit in Sector 42) and $T_c = 1779.19$ BTJD (correct). After masking the transits of HIP 8152 b and HIP 9618 b as identified by BLS, we re-ran our BLS search for both systems. In each case, the BLS power spectrum contained peaks with comparable significance ($S/N \approx 10$) at the aliases of the period allowed by the two widely time-separated transits. We masked the planet c transits by hand in each system and ran another BLS search, but found no additional transit-like events.

For HIP 9618, the SPOC pipeline originally excluded all data points in the Sector 17 light curve beyond 1787.72 BTJD due to a high level of scattered light from Earth, resulting in the exclusion of a second transit of HIP 9618 b in Sector 17 near 1788 BTJD. This initially caused the pipeline to match the first Sector 17 transit of HIP 9618 b with the Sector 17 transit of HIP 9618 c, and to report that TOI-1471.01 had $P = 11.8$ days. It was not until later that TFOP follow-up revealed these two transits were actually of different depth and duration. To include the 1788 BTJD transit of HIP 9618 b in their analysis, Osborn et al. (2023), hereafter O23, re-extracted aperture photometry for HIP 9618 starting from the 2 minute cadence target pixel files. In place of the PDC algorithm, they then use a custom light curve detrending method similar to Vanderburg et al. (2019) in order to remove spacecraft systematics. For the sake of homogeneity in our analysis of each system, we forgo replicating their custom light curve extraction and detrending, meaning that this work does not include the second transit of HIP 9618 b in Sector 17. We note that our measured transit parameters for HIP 9618 b are all consistent with the values reported by O23, and the primary reason for the difference in the size of our uncertainties on the radius of HIP 9618 b ($\pm 0.04 \, R_\oplus$ from O23 and $\pm 0.13 \, R_\oplus$ from this work) is the difference in the reported uncertainty on our stellar radius measurements ($\pm 0.005 \, R_\odot$ from O23 and $\pm 0.03 \, R_\odot$ from this
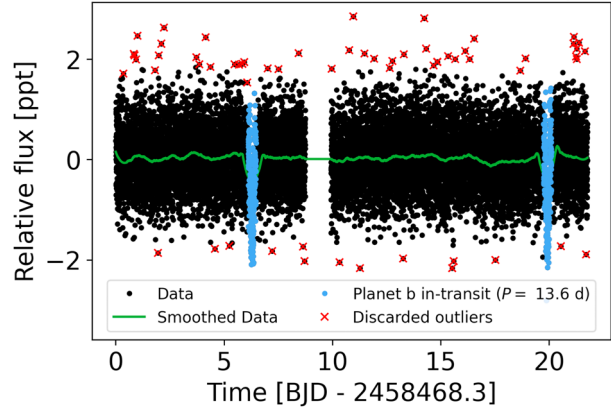

Figure 3. An example of our Savitzky–Golay filtering procedure for HD 42813's Sector 6 PDCSAP photometry. The black points are the PDCSAP data, the green line is the data after being smoothed by the Savitzky–Golay filter, and the blue points are the in-transit data, which are not subjected to the outlier rejection. Outliers are marked in red.

work, where our error estimate has been inflated according to Tayar et al. 2022). We compare our results for HIP 9618 with those from O23 in detail in Section 10.6.2.

6.2. Light Curve Cleaning and Initial Transit Fitting

After inspecting the TESS data for planet transits, we cleaned the photometry with an outlier rejection scheme. First, for each sector we smoothed the normalized TESS PDCSAP data in bins of 0.3 days with a cubic Savitzky–Golay filter (Savitzky & Golay 1964) and iteratively removed out-of-transit, $>3\sigma$ outliers until convergence. We used the SPOC-reported orbital period, time of transit, and transit duration to mask the planet transits, save for HIP 8152 c and HIP 9618 c, since their orbital properties are incorrect in the TOI catalog (see Section 6.1.2). For HIP 8152 c, we used the transit duration of a photometry-only fit to the TESS data (the same as the model described below) with a narrow Gaussian prior on the externally confirmed period of $P = 19.61$ days. For HIP 9618 c, we used the transit duration from O23. Figure 3 illustrates the results of the Savitzky–Golay filtering for HD 42813's Sector 6 PDCSAP data. Across all systems, the number of outliers removed per sector by the Savitzky–Golay filtering was 74 ± 14. For each system, this outlier rejection excluded $\lesssim 0.5\%$ of all of the available TESS data. In each case, our iterative Savitzky–Golay filtering routine converged in three iterations, save for HD 6061, which converged in four iterations.

Next, we performed an additional outlier rejection step by fitting an initial, photometry-only transit plus Gaussian process (GP) model (e.g., Rasmussen & Williams 2006) to the data and iteratively removing 7σ outliers about the fit. The transit model was implemented with a quadratic limb-darkening law (Kipping 2013) from starry (Luger et al. 2019) and the GP, used to remove low-frequency stellar variability and instrumental systematics, was constructed in celerite2 (Foreman-Mackey 2018). Following Kipping (2013), the limb-darkening coefficients are parameterized as $q_1 \equiv (u_1 + u_2)^2$ and $q_2 \equiv 0.5u_1(u_1 + u_2)^{-1}$, where u_1 and u_2 are the usual quadratic limb-darkening coefficients. The transit model is parameterized using $\ln P$, T_c, $\ln R_p/R_*$, b, and $\ln T_{dur}$. The parameters and priors of this initial, photometry-only model are

generally the same as for the final, joint model of the photometry and RVs (Table 6). The main difference between the two is that the joint model does not assume a circular orbit and explicitly uses $\sqrt{e}\cos\omega$ and $\sqrt{e}\sin\omega$ instead of $\ln T_{\rm dur}$. For this initial, photometry-only model, we placed a broad Gaussian prior on $\ln T_{\rm dur}$, the center of which was the logarithm of the transit duration as reported in the TOI catalog when accessed on 2022 October 4, and whose width was $\ln 10$ days. This initial transit model also assumed no information about the stellar mass, since by employing a circular orbit and fitting in terms of $T_{\rm dur}$ we imply a stellar density. We elaborate on the differences between this initial, photometry-only model and our joint model in Section 9.1.

The kernel of the GP used to flatten the light curve is in the form of an overdamped stochastic harmonic oscillator (SHO). The PSD of the SHO kernel can be written as

$$S(\omega_f) = \sqrt{\frac{2}{\pi}}\frac{S_0\omega_0^4}{(\omega_f^2 - \omega_0^2)^2 + \omega_0^2\omega_f^2/Q}, \quad (2)$$

where ω_f is the angular frequency, ω_0 is the undamped fundamental angular frequency, S_0 is the power at ω_0, and Q is the quality factor of oscillation. Following the reparameterization for the SHO PSD from the `celerite2` documentation, we define

$$\rho = \frac{2\pi}{\omega_0}, \quad (3)$$

$$\tau = \frac{2Q}{\omega_0}, \quad (4)$$

and

$$\eta = \sqrt{S_0\omega_0 Q}, \quad (5)$$

where ρ is interpreted as the undamped fundamental period of the oscillator, τ is the characteristic timescale of the damping, and η scales the amplitude of the GP (i.e., η^2 populates the diagonal of the GP covariance matrix). Rewriting Equation 2 in terms of ρ, τ, and η, we have

$$S(\omega_f) = 8\sqrt{2}\pi^{3/2}\frac{\eta^2}{\tau\rho^2}\left[\left(\omega_f^2 - \left(\frac{2\pi}{\rho}\right)^2\right)^2 + \left(\frac{2\omega_f}{\tau}\right)^2\right]^{-1}. \quad (6)$$

The parameters and priors for this GP kernel are the same as used for the GP that flattens the light curve in the joint model (see Section 9.1 and Table 6). We note that a lower bound of 1 day was placed on ρ and τ to prevent the GP from overfitting the transits (see Figure 5).

For HIP 8152, TOI-669, HD 135694, and HIP 9618, no 7σ outliers were identified about this initial photometry-only model. HD 42813, HD 25463, and HD 6061 each had one 7σ outlier that was removed, and TOI-1736 had three. For the systems for which we identified these outliers, we repeated the initial transit model fitting with the outliers removed and found no remaining outliers about the fit. The maximum a posteriori (MAP) values from our initial models, save for $T_{\rm dur}$, were used as the starting values in the MAP optimization routine for the corresponding parameters in the joint models.

6.3. Search for Transit Timing Variations

For completeness, we searched the TESS data for any signs of transit timing variations (TTVs; e.g., Hadden & Lithwick 2017). We used the best-fitting transit times and orbital periods from the initial photometry-only transit model (above) as references for the expected transit times. We performed an MAP fit of the photometry that was analogous to the initial transit model, but now, for each planet, $\ln P$ and $T_{\rm c}$ were replaced with free parameters for the midpoint of each individual transit. We placed a Gaussian prior on each of the observed transit times centered at the expected time with a width of 1 day.

For each of the 11 transiting planets in our sample, we found that the maximum of the absolute difference between the observed and expected transit time $(O - C)$ was <20 min and the median of these maximum values was about 1 min across all planets. None of the $O - C$ time series show an obvious trend or sinusoidal variation. HD 25463 b, TOI-669 b, and HD 135694 b each had a maximum absolute value of $O - C$ between 10 and 20 min, and the scatter in $O - C$ for each of these three planets was about 8 min. These systems may warrant further investigation to determine whether the differences in the observed and expected transit times are significant. However, in the absence of a clear periodic TTV signal, we leave this work to future investigations. For the three multitransiting planet systems in our sample (HIP 8152, HD 25463, and HIP 9618), we note that none of the planet pairs have a near-integer period ratio, so TTVs may not be expected for these systems a priori. Given the lack of obvious evidence for TTVs in each system, we exclude them in our joint model.

7. Search for RV Trends and Nontransiting Companions

With all of the transits accounted for and the photometry cleaned, next we conducted a systematic search for long-term RV trends and the full orbits of nontransiting[41] planetary signals in the RV time series. Long-term RV trends are indicative of massive, distant companions, which are more common for FGK hosts with close-in small planets (our sample) than for other stars (Zhu et al. 2018; Bryan et al. 2019). Our analysis identifies two systems with linear RV trends (HIP 9618 and TOI-1736) and one nontransiting, super-Jovian-mass planet on a moderately eccentric orbit (TOI-1736 c).

7.1. RV Trends

First, we attempted to determine which systems required a linear RV trend. We used the Akaike Information Criterion (AIC; Akaike 1974) to choose between models with and without a linear trend. The AIC is defined as

$$\text{AIC} = 2k - 2\ln\hat{\mathcal{L}}, \quad (7)$$

where k is the number of free parameters in the model, and $\hat{\mathcal{L}}$ is the maximum of the likelihood function with respect to the model parameters. In general, a lower AIC value is considered more favorable. Let $\Delta\text{AIC}_i \equiv \text{AIC}_i - \text{AIC}_{\rm min}$, where AIC_i is the AIC of the ith model under consideration and $\text{AIC}_{\rm min}$ is the lowest AIC value of all models considered. Burnham &

---

[41] We take "nontransiting" to mean that we did not observe a transit in the TESS photometry.

Anderson (2004) provided the following guidelines in interpreting ΔAIC values:

1. If $\Delta\mathrm{AIC}_i < 2$, the two models are nearly indistinguishable.
2. If $2 < \Delta\mathrm{AIC}_i < 10$, the ith model is disfavored.
3. If $\Delta\mathrm{AIC}_i > 10$, the ith model is essentially ruled out.

When two models had $\Delta\mathrm{AIC} < 4$, we chose the simpler model (e.g., even if including a linear RV trend reduces the AIC, if $\Delta\mathrm{AIC} < 4$, we adopted the model without a trend). There are only two systems that demand a linear RV trend: HIP 9618 and TOI-1736. For these systems, we also attempted to include a quadratic term in addition to the linear trend, and while the AIC could not rule out models with curvature, there was no evidence to justify its inclusion.

7.2. Nontransiting Companions

With linear RV trends either excluded or identified, we next used RVSearch (Rosenthal et al. 2021) to search for the full orbits of nontransiting planet candidates in the RV time series. RVSearch employs an iterative generalized Lomb–Scargle (GLS; Lomb 1976; Scargle 1982; Zechmeister & Kürster 2009) periodogram analysis to search for significant periodicity in the RV residuals. Significance is determined following the detection methodology of Howard & Fulton (2016), where an empirical false-alarm probability (FAP) threshold of 0.1% is computed via the Bayesian information criterion (BIC; Schwarz 1978).

The BIC is defined as

$$\mathrm{BIC} = k \ln n - 2 \ln \hat{\mathcal{L}}, \qquad (8)$$

where n is the size of the data, and k and $\hat{\mathcal{L}}$ are the same as in Equation 7. While we could have also used the BIC to determine whether or not to include linear trends in our RV models, simulation studies suggest that for finite sample sizes, the BIC may be at risk of selecting very poor models (Burnham & Anderson 2004; Vrieze 2012). In our analysis, the two comparison statistics typically agreed and could be used relatively interchangeably.

Before applying RVSearch to our RV time series, we removed the signals of the transiting planets and, for HIP 9618 and TOI-1736, the linear RV trends. RVSearch identified no signals above the 0.1% FAP threshold in the RV residuals for all systems except HIP 8152, HD 135694, and TOI-1736. However, for all but TOI-1736, it seems that the signals identified are related to the RV window function. We discuss our interpretation of the detections below.

In the case of HIP 8152, RVSearch identified an eccentric signal ($e \approx 0.7$, $K \approx 4.5$ m s^{-1}) at $P = 122$ days. This is likely the second harmonic of the yearly observing alias (i.e., $122 \times 3 = 366$), and we do not interpret it as planetary in nature. Visually, it is clear that the Keck-HIRES observations of HIP 8152 can be roughly grouped into three observing seasons (see Figure 6, right). This is probably contributing to the power in the RV window function around 365 days (Figure 7). It should also be mentioned that $P = 122$ days is an alias commonly seen in archival Keck-HIRES RV time series (Rosenthal et al. 2021). Furthermore, at periastron passage, a planet with $P = 122$ days and $e = 0.7$ would have a very close (<0.01 au) encounter with the orbit of HIP 8152 c ($P_c = 19.6053 \pm 0.0003$ days), suggesting that such an architecture is not stable.

For HD 135694, RVSearch identified a moderately eccentric signal ($e \approx 0.3$, $K \approx 3.5$ m s^{-1}) at 45.6 days. However, like HIP 8152, there is significant power related to the yearly alias in the periodogram of HD 135694's RV window function (in this case, at 2×365 days; Figure 20), and the supposed period is likely a harmonic of this signal ($365.25/45.60 = 8.00$). Therefore, we also interpret the 45.6 day signal as an artifact of our RV sampling. If the $P = 45.6$ day signal truly is a planet, however, it would not cross orbits with HD 135694 b ($P_b = 15.92346 \pm 0.00002$ days).

The moderately eccentric orbit of the nontransiting super-Jovian, TOI-1736 c, near $P = 570$ days is visible in TOI-1736's RV time series (Figure 25, right). For completeness, we conducted a blind search for the orbit of TOI-1736 c after removing the transiting planet, TOI-1736 b, and the system's linear RV trend. RVSearch recovers the orbit of TOI-1736 c with $P_c = 573.6$ days, $T_c = 2272.4$ BTJD, $K_c = 195$ m s^{-1}, $e_c = 0.37$, and $\omega_c = 162°$. Models of the RVs that either replaced the linear RV trend with the partial orbit of an even longer-period giant planet or included a curvature term in addition to the linear trend were not preferred by the AIC. After removing the linear RV trend and the orbits of planets b and c, RVSearch failed to identify any other signals above the 0.1% FAP threshold in the RV residuals.

8. Stellar Activity Considerations

Stellar activity mitigation is a key component of RV mass measurements for small planets, especially when the stellar rotation period or one of its harmonics is close to the period of the planet in question (e.g., Vanderburg et al. 2016). Most of the hosts in our sample show little Ca II H and K emission, implying that they are relatively inactive—this is in part why they were chosen for Doppler monitoring (Chontos et al. 2022). Using our Keck-HIRES spectra, we measure $\log_{10} R'_{\mathrm{HK}}$ (Middelkoop 1982; Noyes et al. 1984) for each system and find a median value across all eight hosts of -5.00. For reference, over its magnetic cycle, the Sun oscillates between $\log_{10} R'_{\mathrm{HK}} = -5.05$ and -4.84 at the solar minimum and maximum, respectively (Meunier et al. 2010).

With each Keck-HIRES spectrum, we also measured S_{HK} values, which trace Ca II H and K emission strength (Isaacson & Fischer 2010; H. Isaacson et al. 2023, in preparation). While photometry can act as a proxy for stellar activity (e.g., Aigrain et al. 2012; Haywood et al. 2014; Grunblatt et al. 2015), if photometric and spectroscopic monitoring are not contemporaneous, the connection between the time-varying activity signal during the two sampling periods can be unclear (Kosiarek & Crossfield 2020). Because the RV and S_{HK} measurements are simultaneous, they offer a real-time view of the star's behavior and serve as a useful supplement to the TESS photometry.

8.1. Correlated S_{HK} Values and RV Residuals?

As a first step toward understanding the connection between stellar activity and our RV measurements, we examined the correlation between the Keck-HIRES S_{HK} values and the Keck-HIRES RVs after the planetary-attributed RV signals were removed. By "planetary-attributed," we mean the RV signals from transiting planets and, for HIP 9618 and TOI-1736, linear RV trends that we assume are caused by distant giant companions. We attributed the strong linear trends in the RV
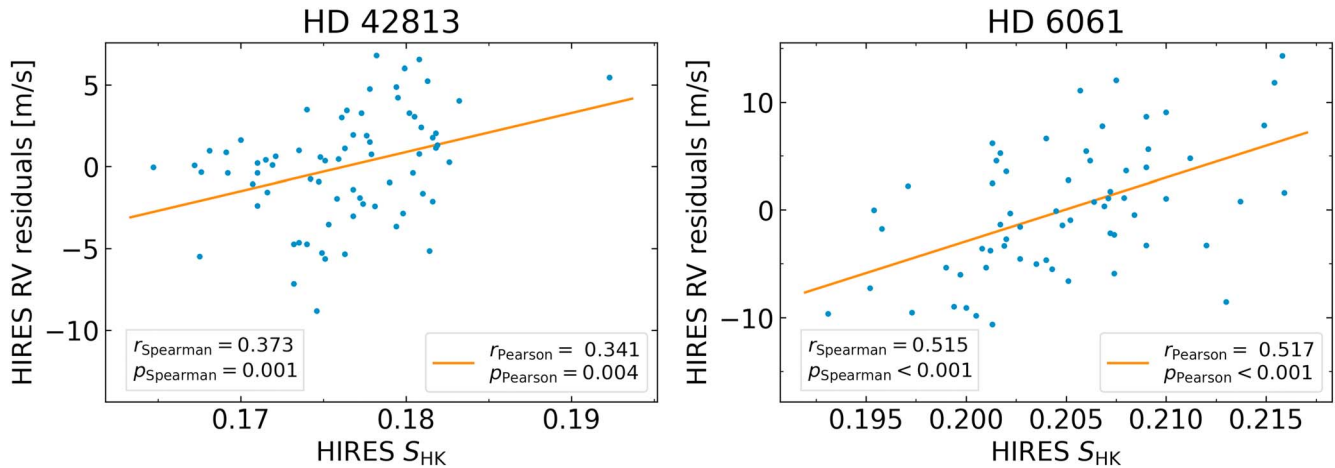
Figure 4. HD 42813 (left) and HD 6061 (right) are the only two systems where the p-value of either the Spearman or Pearson test (and in their cases, both) was <0.05 for the Keck-HIRES RV residuals and S_{HK} values. In each panel, the Keck-HIRES RVs are shown in blue and a linear least-squares fit to the data is plotted in orange. We note that for HD 42813, we removed the one observation with $S_{HK} > 0.19$ and refit the data, but still find $p_{Spearman}$ and $p_{Pearson}$ are both <0.05. The correlation between the RV residuals and the S_{HK} values suggests that stellar activity might be manifesting itself in the RVs, but we emphasize that p-value testing can be unreliable (e.g., Colquhoun 2014). This test is just one point of reference in our broader investigation into stellar activity contamination in the RVs.

time series for HIP 9618 and TOI-1736 to distant giants rather than stellar activity, because for these quiet stars (which have $\log_{10} R'_{HK} = -4.99 \pm 0.05$ and $\log_{10} R'_{HK} = -5.02 \pm 0.05$, respectively) we would expect the amplitude of the stellar activity signal to be on the order of a few meters per second (e.g., Wright 2005; Wright et al. 2008). However, the change in RV over the observing baselines for these systems is closer to $100 \mathrm{~m~s^{-1}}$, and the corresponding change in S_{HK} value is <0.02, so it does not seem like stellar activity could be responsible for the large RV trends. For TOI-1736, we also removed the RV signal of TOI-1736 c, a nontransiting, massive planet on a moderately eccentric orbit near $P = 570$ days, because it is clearly planetary.

With planetary signals removed from the RV time series, we calculated both the Spearman rank-order correlation coefficient ($r_{Spearman}$) and the Pearson correlation coefficient ($r_{Pearson}$) for the Keck-HIRES S_{HK} values and the Keck-HIRES RV residuals (e.g., Press et al. 1992). There were only two systems, HD 42813 and HD 6061, where the p-value for either the Spearman or Pearson test was <0.05 (Figure 4). These p-values may not be trustworthy given the relatively small sizes of the data sets ($N_{HIRES} = 71$ and 64 for HD 42813 and HD 6061, respectively) and concerns regarding p-value testing in general (e.g., Colquhoun 2014), but the apparent correlation between the RV residuals and S_{HK} values in these systems spurred further investigation. According to Ca II H and K emission, HD 42813 is relatively inactive ($\log_{10} R'_{HK} = -4.98 \pm 0.05$), while HD 6061 shows signs of moderate activity ($\log_{10} R'_{HK} = -4.76 \pm 0.05$). For the other systems in our sample, while there appears to be no correlation between the RVs and the Keck-HIRES S_{HK} values, we still conducted a holistic examination of stellar activity.

8.2. Periodogram Analysis

Periodograms are a powerful tool for identifying periodic signals in time series data, though, as we saw with our search for nontransiting planets in Section 7, the physical interpretation of peaks in their power spectra should be treated with care. Caution should also be exercised when searching for signals across complementary data sets. Kosiarek & Crossfield (2020)

found that their periodogram and autocorrelation analyses of solar photometry correctly identify the solar rotation period less than half of the time. With these caveats in mind, we computed GLS periodograms to search for signs of periodicity related to stellar activity in the out-of-transit (OoT) PDCSAP TESS photometry and the Keck-HIRES S_{HK} values for each system. As we did for the periodograms of the RV residuals from RVSearch, we also compared these to the periodogram of the RV window function to place purported signals in context with our imperfect time sampling. Periodograms for each system can be found in Appendix A. FAPs were calculated for these periodograms following Baluev (2008).

In general, we do not see an obvious stellar rotation period in the TESS PDCSAP (or SAP) photometry for any of our hosts. HD 6061 is the only system whose PDCSAP light curve seems to exhibit rotational modulation by eye. The periodogram analysis from Fetherolf et al. (2023) finds that HD 6061's Sector 17 PDCSAP light curve is well fit by a single sinusoid with a period of 4.8 ± 0.4 days and an amplitude of about 0.2 ppt. This $P \approx 5$ day signal coincides with the strong peak we see in our own periodogram of the Sector 17 and 57 OoT PDCSAP photometry (Figure 24). However, the activity–rotation relation from Noyes et al. (1984) suggests that the rotation period of this early-G dwarf should be closer to $P_{rot} \approx 16$ days and the PDC algorithm is known to suppress stellar activity signals with $P \gtrsim 10$ days. A rotation period is not clear in HD 6061's SAP light curve, which seems to be heavily impacted by spacecraft and/or detector systematics (the light curve has sharp ramps and a low-frequency trend). In the end, perhaps the $P \approx 5$ day signal is a harmonic of the rotation period, or an artifact of the interplay between the PDC algorithm and the true astrophysical signal (if any).

Similar to the case for the TESS photometry, none of the systems exhibit a clear and obvious activity signal in the GLS periodogram of their Keck-HIRES S_{HK} values. For every system, the highest peak in the S_{HK} periodogram is either the nightly alias or related to the yearly alias. We comment on other, seemingly inconsequential features of each system's S_{HK} periodogram in Section 10.

8.3. The Case of HD 6061

While most of the stars in our sample are relatively inactive ($\log_{10} R'_{HK} \lesssim -5.0$), HD 6061 is the only host that would sit firmly among the "active" stars ($-5.0 < \log_{10} R'_{HK} < -4.3$) in the activity–rotation analysis of Mamajek & Hillenbrand (2008). HD 6061 is a G0 dwarf (Cannon & Pickering 1993) with moderate Ca II H and K emission ($\log_{10} R'_{HK} = -4.76 \pm 0.05$). The HD 6061 Keck-HIRES RV residuals and S_{HK} measurements are strongly correlated, indicating that a stellar activity signal may be contaminating the RVs. What, then, is the star's rotation period and how does it compare to the orbital period of HD 6061 b ($P_b = 5.25$ days)?

As mentioned in Section 8.2, there appears to be some sort rotational modulation in HD 6061's TESS photometry (with $P \approx 5$ days), but its connection to the stellar rotation period is unclear. The activity–rotation relation from Noyes et al. (1984) suggests $P_{rot} \approx 16$ days, so perhaps the signal in the TESS photometry is a harmonic of the true rotation period. Using `SpecMatch-Syn`, we find $v \sin i_* = 2.4 \pm 1.0$ km s^{-1}. After combining this with our stellar radius measurement ($R_* = 1.03 \pm 0.03\ R_\odot$) and marginalizing over the inclination of the stellar spin axis, HD 6061's projected rotational velocity implies $P_{rot} = 14^{+13}_{-9}$ days. While HD 6061's true rotation period remains uncertain, all of these clues suggest it is reasonable to expect that P_{rot} or its harmonics are in the neighborhood of the orbital period for planet b.

The GLS periodograms of the HD 6061 observations do not point to a clear and obvious stellar rotation period, but they do appear to hint at unresolved signals. After accounting for instrumental offsets and removing the Keplerian signal of HD 6061 b, there are several peaks in the GLS periodogram of the RV residuals. The highest peak is located at $P = 5.5$ days and rises above the 1% FAP level. There are also peaks at the 10% FAP level near $P = 7$, 10, and 16 days. In the GLS periodogram of the Keck-HIRES S_{HK} values, the highest peak between $P = 2$ days and $P = 100$ days (contributions from the window function dominate the power spectrum beyond this range) is a peak at $P = 13$ days that reaches the 10% FAP level. If the stellar rotation period is somewhere between $P = 12$–17 days, this would seem to agree with the Noyes et al. (1984) estimate, our $v \sin i_*$ measurement, and the peaks in the periodograms of the RV residuals and S_{HK} values.

To summarize, for each system we explored the possibility of stellar activity contaminating the RV time series. We checked for a correlation between the Keck-HIRES RV residuals and the S_{HK} values. We also searched for signals in the GLS periodograms of the TESS photometry, S_{HK} values, and RV residuals. HD 6061 is the only system that seems to show an activity signal. Though the principal period of the activity signal is not entirely obvious, various estimates seem to suggest that the stellar rotation period is in the neighborhood of $P = 12$–17 days. In Section 9.3 we describe our formal approach for including a GP model of stellar activity in our joint model of the photometry, RVs, and S_{HK} values.

9. Joint Photometry, Radial Velocity, and Activity Modeling

Here we describe our method for deriving planet properties. In short, we used a custom analysis pipeline based on the Python package `exoplanet` (Foreman-Mackey 2018) to jointly model each system's photometry, radial velocities, and,

if necessary, Keck-HIRES S_{HK} stellar activity indicators. We applied this framework homogeneously to each system in our sample. Our code and worked examples are publicly available (Akana Murphy 2023).

We summarize our joint model of each system in Tables 6 and 7. All model parameters had relatively broad priors, save for the stellar mass and radius, whose informed Gaussian priors stemmed from our high-resolution spectroscopy and isochrone modeling (see Section 4). The likelihood function of the joint model is the product of the likelihood of the transit model and the RV model and, if applicable, the S_{HK} model, all of which assume Gaussian residuals.

9.1. Transits

We parameterize the transit portion of the joint model in terms of $\ln P$, T_c, $\ln R_p/R_*$, b, and $\sqrt{e} \cos \omega$ and $\sqrt{e} \sin \omega$. As in our initial transit modeling, we use the quadratic limb-darkening law from Kipping (2013). When modeling photometry alone, orbital eccentricity, argument of periastron, and impact parameter can be highly degenerate for low to moderate S/N transits (Petigura 2020). This e–ω–b degeneracy can lead to multimodal MAP solutions and create regions of very high curvature on the posterior surface (i.e., the dreaded "funnel" geometry known to plague hierarchical models; Neal 2003). One of the main advantages that our joint model has over separate models of the photometry and RVs is that in most cases, the RVs are able to quickly rule out highly eccentric orbits for the transiting planets, thereby restricting the e–ω–b phase space and alleviating this degeneracy.

We note that when *both* the planet's transit and RV signals are low to moderate S/N, our joint model can still fall victim to the e–ω–b degeneracy because the RVs are not able to rule out cases of high e. For example, when fitting our joint model to HD 42813, we found that a funnel would form at moderate impact parameter ($b \gtrsim 0.7$) and moderate eccentricity ($e \gtrsim 0.2$) because the planet's RV detection is not significant enough ($K/\sigma_K \approx 2.5$) to exclude orbits with large e and small K. In this case, we fixed $e \equiv 0$, which removed the funnel and improved sampling reliability and performance. We encountered a similar situation for HD 25463. In any case, RV-only models of these systems show that the orbits are consistent with being circular (see Section 11).

Assumptions of circular orbits, parameterizing with transit duration (which implies a stellar density), and importance sampling can be used to derive constraints on e and ω when combined with a known stellar density from spectroscopy, for example. This strategy circumvents the e–ω–b degeneracy entirely (e.g., MacDougall et al. 2021). This is the approach we used for our initial photometric model (see Section 6.2) when removing outliers so as to avoid the e–ω–b degeneracy when fitting for the initial MAP solution. While the parameterization in MacDougall et al. (2021) offers a robust method of modeling the photometry alone in the presence of this degeneracy, we chose to fit a joint model for simplicity rather than fitting the photometry and RVs in series. As a sanity check, the posteriors of the transit parameters resulting from of our joint model were all 1σ, consistent with the corresponding MAP values we found from the photometry-only fit.

As we did with our initial transit modeling (Section 6.2), we fit the transit model simultaneously with a GP using a kernel in the form of an overdamped SHO (Equation 6) in order to flatten the light curve. To prevent the GP from absorbing part of the

Table 6
Joint Model of the Photometry and RVs

Parameter	Symbol	Units	Prior	Notes
Light Curve Parameters				
Light curve mean offset	μ_{phot}	ppt	$\mathcal{N}(0, 10)$	
Log photometric jitter	$\ln \sigma_{phot}$	ln ppt	$\mathcal{N}(\ln s_{phot}, 2)$	A
RV instrument parameters				
Offset for RV instrument i	γ_i	m s^{-1}	$\mathcal{U}[-250, 250]$	
Log jitter for RV instrument i	$\ln \sigma_{RV,i}$	m s^{-1}	$\mathcal{N}(\ln s_{RV,i}, 2)[\ln 0.1, \ln 20]$	A
Stellar parameters				
Limb-darkening parameter 1	q_1		$\mathcal{U}[0, 1]$	B
Limb-darkening parameter 2	q_2		$\mathcal{U}[0, 1]$	B
Stellar mass	M_*	$M_\odot$	$\mathcal{N}(M_*, \sigma_{M_*})[0, 3]$	C
Stellar radius	R_*	$R_\odot$	$\mathcal{N}(R_*, \sigma_{R_*})[0, 3]$	C
Transiting planet parameters				
Log orbital period	$\ln P$	ln day	$\mathcal{N}(\ln P_{TOI}, 1)$	D
Time of inferior conjunction	T_c	day	$\mathcal{N}(T_{c,TOI}, 1)$	D
Log occultation fraction	$\ln \frac{R_p}{R_*}$		$\mathcal{N}(\ln \frac{R_p}{R_{*TOI}}, \ln 10)$	D
Impact parameter	b		$\mathcal{U}[0, 1]$	
$\sqrt{e}\cos(\omega)$	ξ_1		$\mathcal{D}(\xi_1, \xi_2)[0, 1], \mathrm{VE}(e\vert\theta)$	E
$\sqrt{e}\sin(\omega)$	ξ_2		$\mathcal{D}(\xi_1, \xi_2)[0, 1], \mathrm{VE}(e\vert\theta)$	E
Log RV semiamplitude	$\ln K$	m s^{-1}	$\mathcal{N}(\ln s_{RV}, \ln 50)$	A
Light curve GP hyperparameters				
Log GP amplitude	$\ln \eta_{phot}$	ln ppt	$\mathcal{N}(0, 10)$	F
Log GP undamped period	$\ln \rho_{phot}$	ln day	$\mathcal{N}(\ln 10, \ln 50)[\ln 1, \ln 200]$	F
Log GP damping timescale	$\ln \tau_{phot}$	ln day	$\mathcal{N}(\ln 10, \ln 50)[\ln 1, \ln 200]$	F

Notes. $\mathcal{N}(X, Y)$ refers to a Gaussian distribution with mean X and standard deviation Y. $\mathcal{N}(X, Y)[A, B]$ refers to a bounded Gaussian with mean X, standard deviation Y, and hard bounds at A and B. $\mathcal{U}[X, Y]$ refers to a uniform distribution inclusive on the interval X and Y.

A: σ_{phot} is treated as a uniform pointwise flux measurement error. s_{phot} refers to the sample standard deviation of the PDCSAP light curve flux. $s_{RV,i}$ refers to the same for the RVs of instrument i.

B: The parameterization $q_1 \equiv (u_1 + u_2)^2$ and $q_2 \equiv 0.5u_1(u_1 + u_2)^{-1}$, where u_1 and u_2 are the usual quadratic limb-darkening coefficients, follows the prescription by Kipping (2013).

C: The bounded Gaussian priors on stellar mass and radius have centers and widths corresponding to our derivation of the stellar parameters in Section 4.

D: For some parameter, x, x_{TOI} refers to the value of that parameter as reported in the TOI catalog when accessed on 2022 October 4. The TOI catalog contains erroneous orbital properties for HIP 8152 c and HIP 9618 c, but the correct orbital ephemerides are known from CHEOPS observations.

E: $\mathcal{D}(\xi_1, \xi_2)[0, 1]$ refers to a uniform distribution over the unit disk (i.e., $\sqrt{\xi_1^2 + \xi_2^2} \leqslant 1$). $\mathrm{VE}(e\vert\theta)$ refers to the mixture distribution from Van Eylen et al. (2019), which is used as a prior on e and whose hyperparameters, θ, are fixed to the posterior medians from that work.

F: The hyperparameters of the GP used to flatten the light curve, which has a kernel whose power spectral density (PSD) is in the form of a stochastic harmonic oscillator (SHO; see Equation 2). ρ_{phot} and τ_{phot}, the undamped period and damping timescale of the SHO, respectively, are forced to be >1 day to prevent the GP from overfitting low signal-to-noise transits.

transit signal, we enforced that the GP's undamped period (ρ) and damping timescale (τ) must both be >1 days. For each system, we also visually inspected each transit to ensure that the GP's prediction was sufficiently smooth across the transit duration. Figure 5 illustrates the simultaneous transit and GP fitting for HD 42813 b's second transit in Sector 6.

9.2. Radial Velocities

To describe the spectroscopic orbits of transiting planets, we used $\ln P$, T_c, $\sqrt{e}\cos\omega$ and $\sqrt{e}\sin\omega$, and $\ln K$, where all but $\ln K$ were shared with the transit model. For each RV instrument we also included an offset (γ) and RV jitter term (σ), where the latter is added in quadrature with the pointwise RV measurement errors. As mentioned in Section 7, for each system, we calculated the AIC of models that included or excluded a linear RV trend, $\dot{\gamma}$. HIP 9618 and TOI-1736 are the only two systems where the AIC ruled out models without a trend. For these systems, we also tried adding a quadratic term to the background trend, but the AIC did not support including the curvature.

TOI-1736 is the only system for which our adopted joint model includes a nontransiting planet. We treated the spectroscopic orbit of the nontransiting planet, TOI-1736 c, in the same way as was done for transiting planets, save for the fact that we broadened the Gaussian priors on $\ln P$ and T_c. The initial guesses for $\ln P$ and T_c were taken from our RVSearch results for the system (see Section 7), and their priors were given a width of ln 50 days and 100 days, respectively. The parameters and priors for the RV signals of nontransiting companions in our joint model are found at the top of Table 7.

9.3. Gaussian Process Modeling of Stellar Activity

GPs are a popular tool for modeling correlated noise in RV data due to stellar activity (e.g., Robertson et al. 2013; Haywood et al. 2014; Grunblatt et al. 2015; Kosiarek & Crossfield 2020). To further investigate contamination from stellar activity in our RV time series beyond our exploratory analysis in Section 8, we added a multidimensional GP to our joint model. We refer to this GP as multidimensional because it is fit to the RVs and Keck-HIRES S_{HK} values simultaneously.

Each instrument (APF-Levy RVs, Keck-HIRES RVs, and Keck-HIRES $S_{\rm HK}$) is assigned its own GP kernel, which shares all hyperparameters with the other kernels, save for the GP amplitude (which we denote with η). In addition to the GP, the Keck-HIRES $S_{\rm HK}$ values are also fit with an offset and jitter term.

While APF-Levy and Keck-HIRES are both iodine-based RV instruments (i.e., they measure RVs in the same spectral region), we use different amplitude hyperparameters for their RV GP kernels. This is done as a catch-all to account for systematic differences in the manifestation of the stellar activity signal in their RV time series (e.g., perhaps those pertaining to their difference in spectral resolution, or differences in long-term spectrograph stability). The practice of using independent GP amplitude hyperparameters for separate RV instruments that cover a similar spectral range is commonplace in the literature (e.g., Grunblatt et al. 2015; Kosiarek et al. 2019, 2021).

The kernel of the multidimensional GP we used to model the stellar activity signal in the RVs and Keck-HIRES $S_{\rm HK}$ values is a mixture of three terms, each of which has a PSD in the form of an SHO (the kernel is the sum of `celerite2`'s `SHOTerm` and `RotationTerm`; Foreman-Mackey 2018). The first term is an overdamped oscillator, meant to describe exponentially decaying behavior such as spot evolution, and is the same as the kernel of the GP used to flatten the light curve (Equation 6). The only difference is that we fix the quality factor to $Q \equiv \frac{1}{\sqrt{2}}$ (which effectively sets the characteristic damping timescale, τ), since this gives the SHO the same PSD as stellar granulation (Harvey 1985; Kallinger et al. 2014). Plugging into and rearranging Equation 6, for instrument i, we have

$$S_{{\rm dec},i}(\omega_f) = 16\sqrt{2}\,\pi^{5/2}\frac{\eta_{{\rm dec},i}^2}{\rho^3}\left[\left(\omega_f^2 - \left(\frac{2\pi}{\rho}\right)^2\right)^2 + \left(\frac{2\sqrt{2}\,\pi\omega_f}{\rho}\right)^2\right]^{-1}.$$

(9)

The second and third terms of the kernel are underdamped SHOs, with fundamental frequencies corresponding to the stellar rotation period and its first harmonic, respectively. For instrument i, the PSDs of these terms can be written as

$$S_{P_{\rm rot},i}(\omega_f) = \sqrt{\frac{2}{\pi}}\frac{S_{1,i}\,\omega_1^4}{(\omega_f^2 - \omega_1^2)^2 + \omega_1^2\omega_f^2/Q_1^2}$$

(10)

and

$$S_{P_{\rm rot}/2,i}(\omega_f) = \sqrt{\frac{2}{\pi}}\frac{S_{2,i}\,\omega_2^4}{(\omega_f^2 - \omega_2^2)^2 + \omega_2^2\omega_f^2/Q_2^2}.$$

(11)

The hyperparameters of $S_{P_{\rm rot},i}$ and $S_{P_{\rm rot}/2,i}$ are related via

$$Q_1 = \frac{1}{2} + Q_0 + \delta Q$$

(12)

$$\omega_1 = \frac{4\pi Q_1}{P_{\rm rot}\sqrt{4Q_1^2 - 1}}$$

(13)

$$S_{1,i} = \frac{\eta_{{\rm rot},i}^2}{(1+f)\omega_1 Q_1}$$

(14)

and

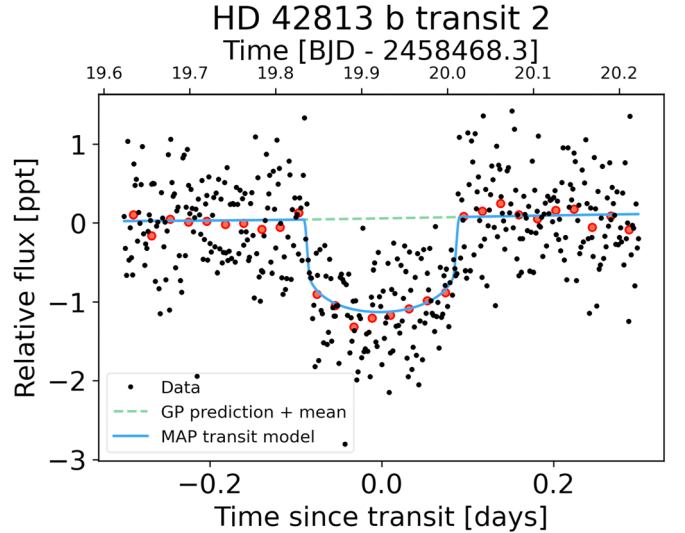$$Q_2 = \frac{1}{2} + Q_0$$

(15)

Figure 5. An example of our simultaneous transit and GP fitting for the second transit of HD 42813 b in Sector 6. The PDCSAP data are shown in black, and data in 30 minute bins are shown in red. The GP prediction across the transit (plus a small global offset fit to the data) is shown as the green dashed line, and the best-fitting transit model is shown as the blue line. We visually inspected each transit across all systems to ensure that the GP prediction did not absorb any of the transit signal.

$$\omega_2 = \frac{8\pi Q_1}{P_{\rm rot}\sqrt{4Q_1^2 - 1}}$$

(16)

$$S_{2,i} = \frac{f\eta_{{\rm rot},i}^2}{(1+f)\omega_1 Q_1},$$

(17)

where $\eta_{{\rm rot},i}$ is the amplitude of $S_{P_{\rm rot},i} + S_{P_{\rm rot}/2,i}$ relative to $S_{{\rm dec},i}$, Q_0 is the quality factor minus $1/2$ for the oscillator at $P_{\rm rot}/2$, δQ is the difference between the quality factors of the oscillators at $P_{\rm rot}$ and $P_{\rm rot}/2$, $P_{\rm rot}$ is the primary period of variability (meant to represent the stellar rotation period), and f is the fractional amplitude of the SHO at $P_{\rm rot}/2$ relative to the SHO at $P_{\rm rot}$.

Putting it all together, the PSD of the GP kernel for instrument i is the sum of a term describing exponentially decaying behavior ($S_{{\rm dec},i}$) and a term describing periodic behavior ($S_{{\rm rot},i}$):

$$S_i(\omega_f) = S_{{\rm dec},i}(\omega_f) + (S_{P_{\rm rot},i}(\omega_f) + S_{P_{\rm rot}/2,i}(\omega_f))$$

(18)

$$= S_{{\rm dec},i}(\omega_f) + S_{{\rm rot},i}(\omega_f).$$

(19)

The GP parameters and priors are summarized in Table 7. We experimented with variants of this kernel (e.g., removing the exponentially decaying term, removing the first-harmonic term, removing the underdamped oscillators, and adding a second overdamped oscillator), but found that this kernel was best at describing both the exponentially decaying and periodic behavior.

9.4. Posterior Estimation

We use No-U-Turn sampling (NUTS; Hoffman & Gelman 2014), an adaptive form of Hamiltonian Monte Carlo (HMC; Duane et al. 1987; Neal 2012) implemented with `exoplanet` and `pymc3` (Salvatier et al. 2016), to estimate the posterior distributions of the parameters in our joint model. HMC sampling uses the gradient of the posterior to help inform

Table 7
Additional Parameters for Nontransiting Planets and Joint GP Modeling of the RVs and Keck-HIRES S_{HK} Values

Parameter	Symbol	Units	Prior	Notes
Nontransiting planet parameters				
Log orbital period	$\ln P$	ln day	$\mathcal{N}(\ln P_{NT}, \ln 50)$	A
Time of inferior conjunction	T_c	day	$\mathcal{N}(T_{c,NT}, 100)$	A
$\sqrt{e}\cos(\omega)$	ξ_1		$\mathcal{D}(\xi_1, \xi_2)[0, 1], \mathrm{VE}(e\|\theta)$	B
$\sqrt{e}\sin(\omega)$	ξ_2		$\mathcal{D}(\xi_1, \xi_2)[0, 1], \mathrm{VE}(e\|\theta)$	B
Log RV semiamplitude	$\ln K$	m s^{-1}	$\mathcal{N}(\ln s_{RV}, \ln 50)$	C
RV trends				
Linear RV trend	$\dot{\gamma}$	m s^{-1} d^{-1}	$\mathcal{N}(0, 10)$	
S_{HK} instrument parameters				
Offset for Keck-HIRES S_{HK} values	$\gamma_{S_{HK},HIRES}$		$\mathcal{U}[0, 1]$	
Log jitter for Keck-HIRES S_{HK} values	$\ln \sigma_{S_{HK},HIRES}$		$\mathcal{N}(\ln s_{S_{HK},HIRES}, 2)$	C
Instrument-specific GP hyperparameters				
GP amplitude of rotation term for Keck-HIRES S_{HK} values	$\eta_{rot,S_{HK},HIRES}$		Inv-$\Gamma(\alpha = 0.85, \beta = 0.004)$	D
Log GP amplitude of exponential decay term for Keck-HIRES S_{HK} values	$\ln \eta_{dec,S_{HK},HIRES}$		$\mathcal{N}(0, 10)$	
Log GP amplitude of rotation term for RV instrument i	$\ln \eta_{rot,RV,i}$	ln m s^{-1}	$\mathcal{N}(0, 10)$	
Log GP amplitude of exponential decay term for RV instrument i	$\ln \eta_{dec,RV,i}$	ln m s^{-1}	$\mathcal{N}(0, 10)$	
RV and S_{HK} shared hyperparameters for GP rotation term				
Log GP rotation period	$\ln P_{rot}$	ln day	$\mathcal{N}(\ln P_{rot,guess}, \ln 1.5)[\ln 1, \ln 60]$	E
Log quality factor of secondary mode	$\ln Q_0$		$\mathcal{N}(0, 2)$	
Log quality factor offset between primary and secondary modes	$\ln \delta Q$		$\mathcal{N}(0, 2)$	
Fractional amplitude of secondary mode relative to primary mode	f		$\mathcal{U}[0.01, 1]$	
RV and S_{HK} shared hyperparameters for GP exponential decay term				
Log undamped period of exponential decay term	$\ln \rho_{dec}$	ln day	$\mathcal{N}(\ln 10, \ln 50)[\ln 1, \ln 100]$	
Quality factor of exponential decay term	Q_{dec}		$\equiv 1/\sqrt{2}$	F

Notes. Notation in this table mirrors that in Table 6.

A: P_{NT} and $T_{c,NT}$ refer to initial guesses for the values of the period and time of inferior conjunction, respectively, for a nontransiting planet's orbit. These were taken as the MAP values from our RVSearch results. Each prior's width is such that we do not expect the initial guesses to bias the best-fitting nontransiting planet orbital parameters.

B: $\mathcal{D}(\xi_1, \xi_2)[0, 1]$ refers to a uniform distribution over the unit disk (i.e., $\sqrt{\xi_1^2 + \xi_2^2} \leqslant 1$). VE$(e|\theta)$ refers to the mixture distribution from Van Eylen et al. (2019), which is used as a prior on e and whose hyperparameters, θ, are fixed to the posterior medians from Van Eylen et al. (2019).

C: s_{RV} refers to the sample standard deviation of the RV time series across all instruments. $s_{S_{HK},HIRES}$ is the sample standard deviation of the Keck-HIRES S_{HK} activity indices.

D: Inv-Γ refers to the inverse Gamma distribution, the parameters of which have been chosen to define the tails of the distribution such that $p(x < 0.001) < 0.01$ and $p(x > 1) < 0.01$. This prior helps keep the amplitude of this GP component positive though with a lighter tail near zero as opposed to a Gamma distribution.

E: $P_{rot,guess}$ is chosen using a periodogram analysis on a case-by-case basis. The default prescription is to assign the value to the period with the peak power in a GLS periodogram of the TESS photometry, though this can be superseded in the context of signals in the RV residuals and/or Keck-HIRES S_{HK} values.

F: Fixing $Q_{dec} \equiv 1/\sqrt{2}$, gives this (overdamped) SHO the same PSD as stellar granulation (Harvey 1985; Kallinger et al. 2014).

Markov transitions, enabling more efficient exploration of high-dimensional posterior surfaces than brute-force, guess-and-check methods like Metropolis-Hastings (Metropolis et al. 1953; Hastings 1970).

For each system, an NUTS sampler ran eight parallel chains with each chain taking at least 8000 "tuning" steps before drawing 6000 samples. Samples drawn during the tuning period were discarded, similar to how various Markov Chain Monte Carlo (MCMC) methods discard burn-in samples. The chains were concatenated to produce a total of $N = 4.8 \times 10^4$ samples from the marginal posteriors of each model parameter.

During the tuning stage, the NUTS sampler optimizes hyperparameters, such as step size, to meet a targeted sample acceptance rate (in our case, 90%) as it explores the posterior surface. This can help prevent the sampler from taking too large of a step while exploring a funnel on the posterior surface (Neal 2003), where the gradient calculation can otherwise diverge and lead to biased inference (Betancourt & Girolami 2013). We found that the posterior geometries of the models of some systems were more prone to regions of high curvature than others, which prompted us to increase the number of tuning steps to prevent divergences (hence why each chain for each sampler took "at least" 8000 tuning steps).

In addition to being conscious of the number of tuning steps, for many joint model parameters that are strictly nonnegative (e.g., planet orbital period, occultation fraction, and RV semiamplitude), we fit and explored the posterior of the natural logarithm of the parameter of interest rather than the parameter itself. We employed this parameterization because imposing hard bounds on the domains of model parameters can encourage the formation of a funnel.

We assessed convergence of the HMC sampling through multiple diagnostic statistics. Vehtari et al. (2021) pointed out serious flaws with the standard Gelman-Rubin statistic ($\hat{R}$; Gelman & Rubin 1992), which is conventionally used to determine convergence for iterative stochastic algorithms like MCMC. Following their prescription, we instead assessed convergence by verifying a sufficiently small (<1.001) *rank-normalized* $\hat{R}$ for each model parameter. In brief, a rank-normalized $\hat{R}$ statistic is computed by calculating $\hat{R}$ on the normalized, rank-transformed chains of the parameter, rather

Table 8
Summary of Derived Planet Properties from Our Joint Analysis

Planet Name	P (d)	T_c (BTJD)	e	R_p ($R_\oplus$)	M_p ($M_\oplus$)	T_{eq} (K)
HIP 8152 b	10.75101 ± 0.00006	1758.620 ± 0.002	<0.14	2.56 ± 0.19	7.8 ± 1.8	855 ± 28
HIP 8152 c	19.6053 ± 0.0003	1751.195 ± 0.005	<0.28	2.48 ± 0.19	9.4 ± 2.2	699 ± 23
HD 42813 b	13.63083 ± 0.00003	1842.6015 ± 0.0007	$\equiv 0$	3.36 ± 0.14	5.8 ± 2.4	755 ± 21
HD 25463 b	7.049144 ± 0.000009	1978.3531 ± 0.0006	$\equiv 0$	2.62 ± 0.16	8.5 ± 3.1	1290 ± 41
HD 25463 c	3.044050 ± 0.000008	1980.314 ± 0.001	$\equiv 0$	1.50 ± 0.12	<4.1	1707 ± 54
TOI-669 b	3.94515 ± 0.00002	1913.041 ± 0.002	<0.23	2.60 ± 0.17	9.8 ± 1.5	1235 ± 37
HD 135694 b	15.92346 ± 0.00002	2324.5878 ± 0.0007	<0.42	2.51 ± 0.14	5.7 ± 2.1	815 ± 27
HIP 9618 b	20.77288 ± 0.00005	2120.5612 ± 0.0008	<0.13	3.75 ± 0.13	8.4 ± 2.0	685 ± 17
HIP 9618 c	52.5636 ± 0.0002	2094.572 ± 0.001	<0.12	3.34 ± 0.13	<7.9	503 ± 13
HD 6061 b	5.254467 ± 0.000009	2321.505 ± 0.001	$\equiv 0$	2.45 ± 0.09	10.8 ± 2.7	1194 ± 28
TOI-1736 b	7.073091 ± 0.000008	2740.5891 ± 0.0007	<0.16	3.05 ± 0.19	11.9 ± 1.6	1186 ± 41
TOI-1736 c	571.3 ± 0.5	2273.1 ± 0.4	0.369 ± 0.002	$\cdots$	2477 ± 118[a]	274 ± 10

Note. A summary of the results of our joint modeling framework. The full results of our stellar characterization and joints analysis for each system can be found in Appendix A. BTJD = BJD − 2457000. Upper limits reflect 98% confidence. T_{eq} is calculated assuming zero Bond albedo and full day–night heat redistribution.
[a] TOI-1736 c is nontransiting, meaning that this value is in fact $M_p \sin i_p$.

than the values of the parameter itself. To ensure the chains could offer reliable confidence intervals, we also calculated the rank-normalized bulk and tail effective sample sizes from Vehtari et al. (2021) for each of the marginal posteriors (roughly, the effective sample sizes are the number of "independent" samples obtained in the bulk and tails of the posterior). Vehtari et al. (2021) recommend that the effective sample size should be larger than 400 in both the bulk and tails of the posterior. For every parameter, we find that the minimum between the bulk and tail effective sample sizes was comfortably larger than the recommended minimum threshold (typically we find $N_{eff} \gtrsim 10^4$).

10. Joint Modeling Results

Here we describe the results of our stellar characterization, joint modeling, and posterior estimation for each system. In this section we include figures of the joint modeling results and periodograms for HIP 8152 to inform their general format, but the rest can be found in Appendix A. Table 8 contains a brief summary of the physical properties for all 12 planets. Tables of all measured and derived planet properties, as well as stellar properties, can be found for each system in Appendix A.

10.1. HIP 8152 (TOI-266)

HIP 8152 is an inactive G dwarf for which we report the discovery of twin sub-Neptunes, HIP 8152 b and HIP 8152 c. Figure 6 summarizes our joint analysis and Table 10 summarizes the system properties.

As mentioned in Section 6.1.2, before CHEOPS follow-up, HIP 8152 c constituted a duotransit scenario. TESS observed only two transits of HIP 8152 c, one in Sector 3 and one in Sector 33, initially obfuscating the planet's true period. In 2022 May, a GLS periodogram analysis of the RVs with planet b removed showed a clear peak at $P = 19.6$ days. We built a joint model of the TESS photometry and Keck-HIRES RVs with MonoTools (Osborn et al. 2022), which statistically ruled out all aliases other than the 19.6 day period. CHEOPS then confirmed the period of HIP 8152 c by observing an additional transit in 2022 August (via private communication with the CHEOPS GTO team, point of contact H. Osborn).

We do not include a GP to model stellar activity in the RVs. HIP 8152 is inactive according to Ca II H and K emission, and the Keck-HIRES RVs and S_{HK} values are not correlated. Furthermore, there are no peaks rising above the 0.1% FAP threshold in a GLS periodogram of the Keck-HIRES S_{HK} values. As discussed in Section 7, the only peak that rises above the 0.1% FAP threshold in the RV residuals is near 120 days and is likely related to the RV window function. Figure 7 shows the GLS periodograms for the system.

HIP 8152 b and c sit near the peak of the sub-Neptune distribution in the mass–radius plane and are on orbits slightly short of a 2:1 mean-motion resonance (MMR; $P_c/P_b = 1.8$). With nearly identical physical properties, these planets are attractive candidates for comparative studies in planet composition. Interestingly, HIP 8152 b, though closer to the G dwarf host, is slightly less dense than HIP 8152 c.

10.2. HD 42813 (TOI-469)

HD 42813 is an inactive, metal-rich K0V dwarf (Houk & Smith-Moore 1988). We report the discovery of a transiting sub-Neptune in the system, HD 42813 b. Our adopted model assumes a circular orbit for HD 42813 b since posterior estimation for a model that included eccentricity was hindered by the planet's modest RV detection (see Section 9.1). In any case, a simpler, RV-only model that includes eccentricity finds that the planet's orbit is consistent with being circular (see Section 11). Figure 13 summarizes our joint analysis and Table 11 summarizes the system properties.

While the Keck-HIRES RVs appear to be slightly correlated with the Keck-HIRES S_{HK} values (see Figure 4, left panel), we decided to leave out a GP fit to the RVs and S_{HK} values in our joint model. HD 42813 is seemingly inactive according to Ca II H and K emission to begin with. Furthermore, we do not find significant peaks in the GLS periodogram of the residuals of the Keplerian-only RV model. There are no peaks rising above the 0.1% FAP threshold in the GLS periodogram of the Keck-HIRES S_{HK} values save for broad peaks that are consistent with the yearly alias and its harmonics. In addition, the GLS periodogram of the RV window function shows significant power at the yearly and lunar monthly aliases, making it difficult to disentangle a would-be activity signal in the RV
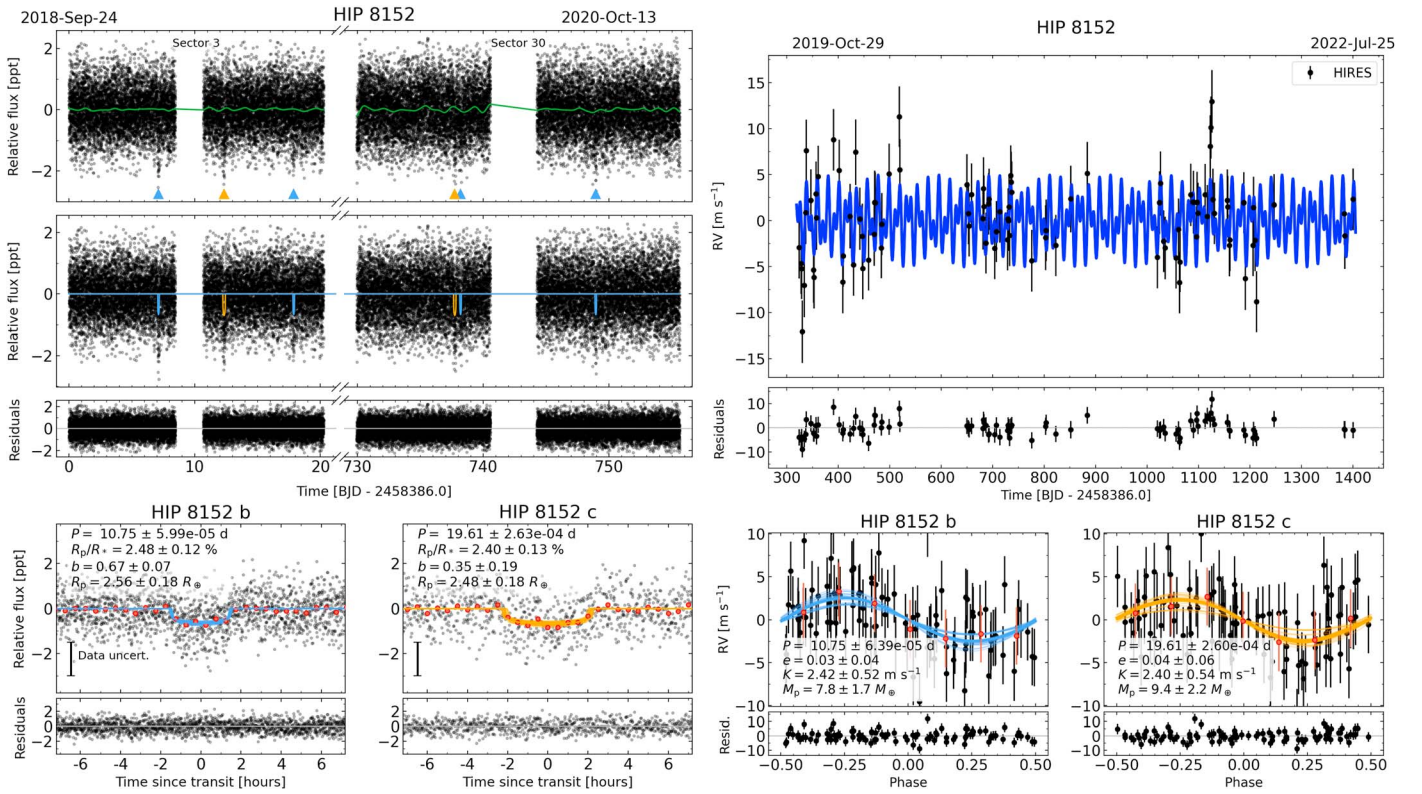
Figure 6. Our joint modeling results for HIP 8152. Left: the photometric model. The top panel shows the PDCSAP light curve as the black points, with the GP used to flatten the light curve plotted as the green line. Triangles mark transits for planets b (blue) and c (orange). The middle panel shows the flattened light curve in black and the best-fitting transit models for planets b and c in blue and orange, respectively. Residuals are shown below. Phase-folded light curves and residuals are shown in the bottom panels for planets b (left) and c (right), with data in 30 minute bins shown in red. The phase-folded best-fitting transit models for each planet are shown as the slightly thicker blue and orange lines, with 25 random posterior draws overplotted as the thinner lines. Right: the RV model. The top panel shows the RV time series with Keck-HIRES data in black and the RV model in blue. Residuals are shown below. Phase-folded RV curves for planets b and c are shown in the bottom panels. Red points are data binned in 0.125 units of orbital phase. The phase-folded best-fitting RV models for each planet are shown as the slightly thicker blue and orange lines, with 25 random posterior draws overplotted as the thinner lines.
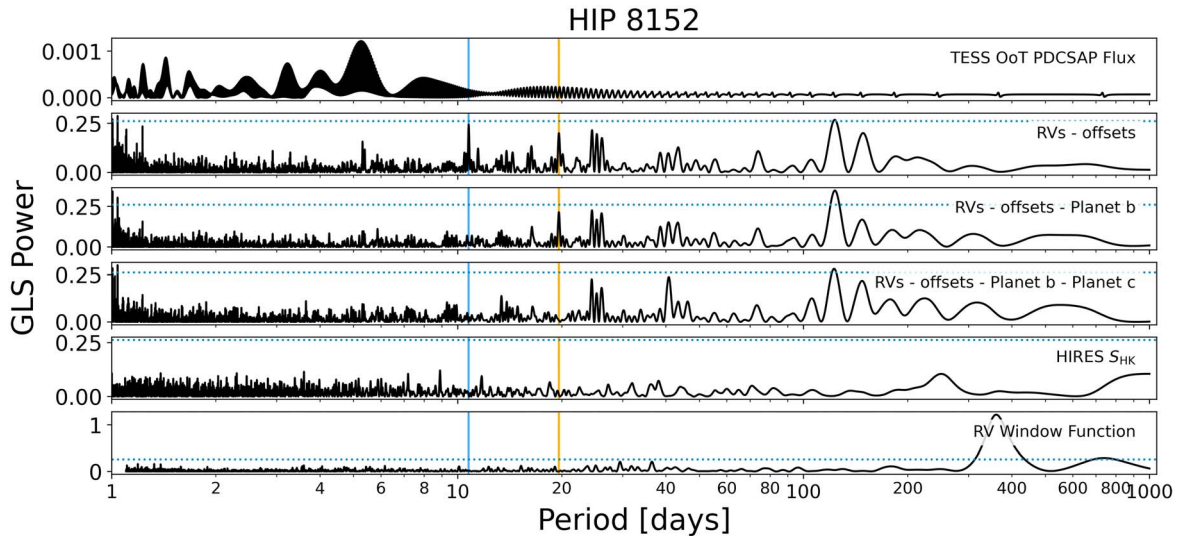
Figure 7. GLS periodograms for HIP 8152 are shown in black. The vertical blue and orange lines mark the orbital periods of planets b and c, respectively. The dashed horizontal line indicates the 0.1% FAP threshold (Baluev 2008). We compute the GLS periodogram of the RV window function with a minimum period slightly longer than 1 day to avoid the strong nightly alias, which otherwise skews the y-axis scale.

residuals from artifacts of the RV time sampling (Figure 14). We fit a joint model to the data that included a GP and recovered a mass measurement for HD 42813 b that was entirely consistent with the results of our Keplerian-only model. We therefore adopt a joint model of the TESS photometry and Keck-HIRES RVs that does not include a GP fit to the RVs and S_{HK} values.

With its seemingly low density, HD 42813 b is a very attractive candidate for atmospheric follow-up (TSM >89 at 98% confidence). However, continued RV

monitoring is first required to refine the planet's mass measurement.

10.3. HD 25463 (TOI-554)

As an F8 dwarf (Cannon & Pickering 1993), HD 25463 has the earliest spectral type of all of the hosts in our sample. We report the discovery of two transiting planets orbiting HD 25463: the sub-Neptune HD 25463 b and the super-Earth HD 25463 c. Similar to HD 42813, we enforced circular orbits for planets b and c to avoid divergences during the HMC posterior estimation, though an RV-only model that included eccentricity found that the orbits were consistent with being circular (see Section 11). Figure 15 summarizes our joint analysis and Table 12 summarizes the system properties.

HD 25463 is seemingly inactive according to Ca II H and K emission ($\log_{10} R'_{HK} = -5.26 \pm 0.05$). However, we were prompted to explore a model that included a GP for activity mitigation because of the star's relatively rapid rotation. Using SpecMatch-Syn we find $v \sin i_* = 11.6 \pm 1.0$ km s^{-1}. When combining this with our stellar radius measurement and marginalizing over the inclination of the stellar spin axis, the star's projected rotation velocity implies $P_{rot} = 4.3^{+1.7}_{-2.8}$ days. If this simplistic estimate is to be trusted, the stellar rotation period is very close to the orbital periods of the transiting planets ($P_b = 7.0$ days and $P_c = 3.0$ days). Vanderburg et al. (2016) highlighted how stellar rotation can confuse the search for the Doppler signals of planets when P_{rot} and its first harmonic are in the neighborhood of the planets' orbital periods. Despite this concern, we do not find peaks above the 0.1% FAP threshold in a GLS periodogram of the RVs after removing planets b and c. There are also no peaks that rise above the 0.1% FAP threshold in a GLS periodogram of the Keck-HIRES S_{HK} values (see Figure 16). Nevertheless, we added a GP to our joint model of the system with a Gaussian prior of $\mathcal{N}(4, 1.5)$ days on P_{rot}, where 1.5 days is the Gaussian's standard deviation. The GP-enabled model finds best-fitting masses for planets b and c that are consistent with the posterior estimates of the non-GP model, but the HMC sampling had difficulty converging due to the large number of additional model parameters introduced by the GP kernel. We therefore adopt the non-GP model, whose HMC sampling does converge.

Given the brightness of the system ($V = 6.9$ mag, $J = 6.0$ mag), HD 25463 is highly amenable to both ground- and space-based follow-up. With planets on opposite sides of the radius valley (Fulton et al. 2017; Van Eylen et al. 2018), HD 25463 represents an opportunity for comparative studies in atmospheric mass loss. Though HD 25463 is too bright for single object slitless spectroscopy (SOSS) with JWST's Near Infrared Imager and Slitless Spectrograph (NIRISS; brightness limit of $J = 6.5$ mag), the system represents an attractive target for HST. The mass measurement precision for the planets must be improved, however, before they are subjected to detailed atmospheric characterization (Batalha et al. 2019).

10.4. TOI-669

TOI-669 is an inactive G dwarf for which we report the discovery of a hot transiting sub-Neptune, TOI-669 b. Figure 17 summarizes our joint analysis, and Table 13 summarizes the system properties.

We do not include a GP to model a stellar activity signal in the RVs and S_{HK} values. TOI-669 is inactive according to Ca II H and K emission, and the Keck-HIRES RVs and S_{HK} values are not correlated. Furthermore, there are no peaks rising above the 0.1% FAP threshold in a GLS periodogram of the Keck-HIRES S_{HK} values or the Keck-HIRES RV residuals (see Figure 18).

A less significant peak near 9.6 days is visible in the periodogram of the RV residuals, but it is unclear whether the signal is planetary or related to the RV window function, which has significant power near 180 days and 25 days. If the $P = 9.6$ day signal is in fact a planet, assuming a circular orbit, $b > 1$ would imply an orbital inclination of $i_p < 86°.8$. For reference, the orbit of TOI-669 b has $i_b = 88°.7 \pm 1°.0$. A two-planet fit to the RVs using RadVel (Fulton et al. 2018) does not result in a significant detection of the $P = 9.6$ day signal (it finds $M_p \sin i_p = 5.0 \pm 2.6$ $M_\oplus$ for a Keplerian at $P = 9.61 \pm 0.52$ days; the resulting mass of TOI-669 b in this two-planet fit is consistent with our adopted joint model). The ΔAIC between the one- and two-planet RadVel models is <1, so there does not appear to be evidence for including the $P = 9.6$ day signal.

TOI-669 is a relatively bright G dwarf ($J = 9.6$ mag) whose hot sub-Neptune ($T_{eq} = 1235 \pm 37$ K, $S_p = 388.2 \pm 47.1$ $S_\oplus$) lies just outside of the "sub-Neptune desert" (planets with $2.2 < R_p < 3.8$ $R_\oplus$ and $S_p > 650$ $S_\oplus$; Lundkvist et al. 2016). TOI-669 b's mass and radius measurements place it at the mode of the sub-Neptune mass–radius distribution.

10.5. HD 135694 (TOI-1247)

HD 135694 is a K0 dwarf (Cannon & Pickering 1993). We report the discovery of a warm sub-Neptune in the system, HD 135694 b. Figure 19 summarizes our joint analysis, and Table 14 summarizes the system properties.

We do not include a GP to model stellar activity in the RV time series. HD 135694's Ca II H and K emission ($\log_{10} R'_{HK} = -4.99 \pm 0.05$) indicates that the star is relatively inactive and the Keck-HIRES RV residuals and S_{HK} values do not appear to be correlated. Although there are 14 sectors of TESS photometry available, a stellar rotation period is not readily apparent in either the PDCSAP or SAP light curve. There is a strong peak (<0.1% FAP) in the RV residuals at 45.6 days (see Figure 20), but we attribute this power to the RV window function given that 45.6 is a near-perfect divisor of 365.25. It is unclear why our mass measurement is so imprecise (about 2.7σ) when we have nearly 200 RV measurements between APF-Levy and Keck-HIRES. Below, we discuss scenarios that may be the cause of model misspecification.

After the $P = 45.6$ days peak, second-highest peak in the GLS periodogram of the RV residuals rises above the 10% FAP threshold and is located at about $P = 32.5$ days. This period is not a clear harmonic of the yearly alias or the lunar monthly alias, but it is just about twice the period of HD 135694 b ($32.5/15.9 = 2.0$). The highest peak short of $P = 100$ days in the GLS periodogram of the Keck-HIRES S_{HK} values (beyond $P = 100$ days the GLS power is dominated by contributions from the RV window function) is at about $P = 31$ days and also rises above the 10% FAP threshold. While the $P = 32.5$ day peak in the RV residuals is not overwhelmingly significant, it could represent either a nontransiting planet in a near 2:1 MMR with HD 135694 b, or the stellar rotation period. The latter explanation seems slightly more preferable given the $P \approx 31$ days peak in the GLS

periodogram of the Keck-HIRES S_{HK} values. Furthermore, the activity–rotation relation from Noyes et al. (1984) suggests that HD 135694 has $P_{rot} \approx 29$ days, making a rotation period of roughly 31–33 days seem reasonable for this K0 dwarf.

For completeness, we added a GP component to our joint model following the methodology in Section 9.3. We placed a Gaussian prior on the GP rotation period at 32.5 days with a width of 1.5 days. The only other difference between this model and our adopted model of the photometry and RVs is that we forced HD 135694 b's orbit to be circular so as to prevent the HMC sampling from diverging (which it tended to do when allowing e_b and ω_b to float). This GP-enabled model returned $M_b = 6.1 \pm 2.1\ M_\oplus$, in agreement with the results of our adopted model.

We also explored the idea that the signal near 32 days could be a nontransiting planet in a near 2:1 MMR with planet b. We fit a joint model where the GP in the model above was replaced with a nontransiting planet on a circular orbit. This model finds $M_b = 6.6 \pm 2.1\ M_\oplus$ for HD 135694 b (which agrees with the results of our adopted, one-planet model) and $M_p \sin i_p = 10.6 \pm 2.6\ M_\oplus$ for the signal at $P = 32.5$ days. The AIC favors the one-planet plus GP model over the (adopted) one-planet model, which itself is favored over the two-planet model (all at the ΔAIC > 10 level). It should be noted, however, that GPs can be susceptible to overfitting (e.g., Blunt et al. 2023), which can muddle the interpretability of Bayesian model comparison statistics. In this context, the AIC's preference for the GP-enabled model is not entirely surprising. Setting aside the AIC comparison, if there was a nontransiting planet at 32.5 days, assuming a circular orbit, $b > 1$ for the planet would imply $i_p < 88°.6$. For reference, we find that planet b's orbit has $i_b = 89°.1 \pm 0°.5$. Simulations similar to those conducted by Lubin et al. (2022) could be used to place a lower limit on the inclination of the potential nontransiting planet, but these are beyond the scope of this work.

In summary, we cannot rule out the possibility that the $P = 32.5$ day signal represents either the stellar rotation period or a nontransiting planet. However, the signal's ambiguity, combined with the star's lack of Ca II H and K emission, encouraged us to adopt a model of the photometry and RVs that does not use a GP for stellar activity mitigation and does not include nontransiting planets. In any case, our experimentation with various models of the data reassures us that the mass measurement of planet b is seemingly insensitive to our choice of model. HD 135694 is a bright ($V = 9.1$ mag, $J = 7.9$ mag) K0 dwarf that adds another planet to the mode of the sub-Neptune mass–radius distribution. Continued Doppler monitoring is required to refine the planet's mass measurement precision.

10.6. HIP 9618 (TOI-1471)

10.6.1. Joint Analysis from This Work

HIP 9618 is a G5 dwarf (Cannon & Pickering 1993). The system is host to two warm sub-Neptunes, HIP 9618 b and HIP 9618 c. We robustly detect a linear RV trend, indicating that there is also a distant, massive companion in the system. Figure 21 summarizes our joint analysis, and Table 15 summarizes the system properties.

We exclude a GP fit to the RVs and Keck-HIRES S_{HK} values from our adopted model. HIP 9618 is nominally inactive based on

its Ca II H and K emission levels ($\log_{10} R'_{HK} = -4.99 \pm 0.05$), and the Keck-HIRES RV residuals and S_{HK} values are not correlated. Stellar activity does not seem to be a concern for HIP 9618 according to our GLS periodograms (Figure 22). There are no peaks that rise above the 0.1% FAP threshold in the RV residuals of our joint model. In the GLS periodogram of the Keck-HIRES S_{HK} values, there is a peak just long of 30 days that rises above the 0.1% FAP level, but it is unclear whether or not the power is related to the window function—the periodogram also shows significant power near 180 days and at $P > 700$ days. Even if the signal near $P = 30$ days in the S_{HK} values is related to the stellar rotation period for this late-G dwarf, the lack of power in the periodogram of the RV residuals indicates that activity is not greatly impacting the planet mass measurements.

The nature of the massive companion causing the linear RV trend is uncertain. We find that the companion must have $M \sin i_p \gtrsim 4.7\ M_{Jup}$ and $a \gtrsim 5.0$ au by making the following simplifying assumptions: (1) the RV trend is caused by a single companion, (2) the companion's orbit is circular, (3) the companion's orbital period is greater than four times our APF-Levy and Keck-HIRES RV baseline (about 1042 days), and (4) the RV semiamplitude of the companion's orbit is greater than the ΔRV caused by the trend over the baseline (about 62 m s^{-1}). A more detailed investigation is beyond the scope of this work—in Section 10.6.2 we summarize the results from O23, who conduct a thorough analysis of the trend that includes constraints from RVs, astrometry, and direct imaging. Continued RV monitoring is required to reveal the true nature of the distant companion.

HIP 9618 is perhaps the most exciting system in our sample for atmospheric follow-up with JWST. As noted by O23, HIP 9618 is one of only five multitransiting systems with $K_s < 8$ mag to host a planet with $P > 50$ days. Our mass constraints translate to TSM values of 161 ± 43 and >87 for planet b and c, respectively (with the lower limit for planet c reflecting 98% confidence). These values place both planets above the Kempton et al. (2018) TSM cutoff (>84) for follow-up of planets with $2.75 < R_p < 4\ R_\oplus$. Moreover, HIP 9618 b's TSM estimate places it in the top quartile of all planets in its radius range (top quartile cutoff of TSM >146).

10.6.2. Comparison with the O23 Results

O23 first reported the discovery and confirmation of HIP 9618 b and c using space-based photometry from TESS and CHEOPS in combination with a total of 49 RVs from CAFE, HARPS-N, and SOPHIE. The authors report masses of $M_b = 10.0 \pm 3.1\ M_\oplus$ and $M_c < 18\ M_\oplus$ (at 3σ confidence).

The only significant difference between the RV model presented in this work and the adopted model from O23 is that, in addition to including a linear trend in their model of the RVs, O23 also include a quadratic term ($\ddot\gamma$). O23 found $\dot\gamma = -0.067 \pm 0.001$ m s^{-1} day^{-1} and $\ddot\gamma = -4.99 \times 10^{-6} \pm 6.4 \times 10^{-7}$ m s^{-1} day^{-2}. O23 used orvara (Brandt et al. 2021) to translate their reported RV trend and curvature, the lack of an astrometric detection with Hipparcos (Lindegren et al. 1997) and Gaia, constraints from HRI, the lack of secondary lines in their high-resolution spectra of HIP 9618, and the assumed stability of the inner transiting planet system into orbital separation and mass ratio posteriors for a distant, massive, single companion. O23 suggest the companion is either a brown dwarf or low-mass M dwarf with $0.08^{+0.12}_{-0.05}\ M_\odot$ in an orbit at 26^{+19}_{-11} au.

The curvature reported by O23 is driven by just three SOPHIE RVs acquired between 2011 October and 2011 December—the next SOPHIE RV (which also happens to be the next RV from any of their three RV instruments) was taken 8 yr later in 2019 December. If we exclude the three SOPHIE RVs collected in 2011 from our RV analysis (either with our joint model or with `RadVel`), then the curvature detection disappears. Perruchot et al. (2008) quoted SOPHIE's RV stability as being $\approx$3 m s^{-1} over several months. To explore the possibility that the purported curvature is in fact due to the instrument's RV zero-point drift over the 8 yr ($\approx$100-month) gap between observations, we refit all of the available RVs in `RadVel`, included a linear RV trend (but no curvature), and treated the 2011 SOPHIE RVs as coming from their own instrument (i.e., we assigned them their own RV offset and jitter). This model finds a linear RV trend consistent with that of our adopted joint model of the APF-Levy and Keck-HIRES RVs. To enable this consistency, the 2011 SOPHIE RVs require about a 30 m s^{-1} offset. Our APF-Levy and Keck-HIRES RVs lack the baseline to independently confirm the RV curvature reported by O23. Additional, long-term monitoring is required to fully characterize the distant companion.

Finally, we added all of the RV data from O23 to a joint model of the TESS photometry and our APF-Levy and Keck-HIRES RVs. For better comparison with O23, we include the 2011 SOPHIE RVs and RV curvature in addition to the linear trend. We include RV jitter terms and offsets for each instrument and fit the same jitter and offset term to both the pre- and post-2012 SOPHIE data. Our joint model of the combined data set finds $M_b = 7.9 \pm 1.8$ $M_\oplus$ and $M_c < 8.0$ $M_\oplus$ at 98% confidence, which is consistent with our adopted joint model of the APF-Levy and Keck-HIRES RVs. The RV portion of this joint model can be seen in Figure 8. While we have discussed the results of modeling all of the available RV data for the sake of completeness, in the interest of homogeneity, the values found in Tables 8 and 15 stem from our joint model that includes only the APF-Levy and Keck-HIRES RVs.

10.7. HD 6061 (TOI-1473)

HD 6061 is a moderately active G0 dwarf (Cannon & Pickering 1993) for which we find an M4/5V dwarf companion, TIC 600433892, that is almost certainly gravitationally bound (see Section 3.4). We also report the discovery of the hot sub-Neptune, HD 6061 b. Figure 23 summarizes our joint analysis and Table 16 summarizes the system properties.

Following the methodology in Section 9.3, our adopted model includes a GP to address stellar activity. Since we include a GP in our model of the RVs, we assume a circular orbit for HD 6061 b to reduce model complexity and improve the performance of the HMC sampling. For a model that included both the GP and orbital eccentricity for HD 6061 b, the NUTS sampler suffered from divergences after tuning and failed to converge. For completeness, we fit a non-GP model of the system that included eccentricity and found that HD 6061 b's orbit is consistent with being circular.

HD 6061's Ca II H and K emission suggests that it is moderately active ($\log_{10} R'_{HK} = -4.76 \pm 0.05$). We also find that the Keck-HIRES RV residuals and S_{HK} values are strongly correlated (Figure 4, right). As discussed in Section 8.3, various lines of inquiry suggest that the stellar rotation period is in the neighborhood of $P_{rot} \approx 12$–17 days. For our adopted, GP-

enabled joint model, we placed a Gaussian prior on P_{rot} in the middle of this range, at $\mathcal{N}(14.5, 1.5)$ days. Figure 9 shows the GP model of the Keck-HIRES S_{HK} values, which is fit simultaneously with the GP of the RVs. After removing the GP and the orbit of planet b, the GLS periodogram of the RV residuals contains no peaks rising above the 0.1% FAP threshold (see Figure 24). Our posterior estimation finds $P_{rot} = 13.9 \pm 1.5$ days.

For completeness, we explored alternative models of the HD 6061 observations to check for model overfitting, which can plague GP-based planet mass measurements (e.g., Blunt et al. 2023). A joint model of the photometry and RVs that did not include a GP and did not assume a circular orbit for HD 6061 b finds $M_b = 7.8 \pm 2.9$ $M_\oplus$ and that e_b is consistent with zero. The mass measurement from this Keplerian-only model is nearly 1σ, consistent with the planet mass measurement from our adopted model. Perhaps the slightly lower-mass measurement from the Keplerian-only model suggests that our adopted, GP-enabled model is overfitting slightly, but not egregiously so. In Section 11.2, we explore a model of the RVs that uses a different GP kernel and find a planet mass measurement that is consistent with our adopted model.

HD 6061 is a bright ($V = 8.8$ mag, $J = 7.7$ mag) G dwarf with a close-in sub-Neptune planet that lands near the mode of the sub-Neptune mass–radius distribution. Continued RV monitoring is required to refine the planet mass measurement and better understand the stellar activity signal.

10.8. TOI-1736

TOI-1736 is a subgiant star for which we report the discovery of a transiting sub-Neptune, TOI-1736 b, and a temperate super-Jovian-mass planet on a moderately eccentric orbit, TOI-1736 c. We robustly detect a linear trend in the RVs, indicating that there is also a distant, massive companion in the system. Figure 25 summarizes our joint analysis and Table 17 summarizes the system properties.

We do not include a GP in our joint model. TOI-1736 is seemingly inactive according to Ca II H and K emission ($\log_{10} R'_{HK} = -5.02 \pm 0.05$) and the Keck-HIRES RVs and S_{HK} values do not appear to be correlated. Furthermore, there are no peaks in a GLS periodogram of the RV residuals that rise above the 0.1% FAP threshold. We note a peak in the RV residuals near 55 days that rises above the 1% FAP level, but it is unclear whether this signal is planetary, activity-related, or related to the RV window function.

The nature of the massive companion causing the linear RV trend is uncertain. Over our observing baseline of 909 days, the linear RV trend causes a ΔRV of about 166 m s^{-1}. Using the same set of crude assumptions as we did for the case of HIP 9618, we find that the companion must have $M \sin i_p \gtrsim 12.9$ M_{Jup} and $a \gtrsim 4.7$ au, tentatively suggesting that it is too massive to be a planet. Relaxing the assumption that the companion is on a circular orbit, with $a = 4.7$ au, it must have $e \lesssim 0.6$ so as not to cross the orbit of TOI-1736 c, which implies a minimum mass limit of $M \sin i_p \gtrsim 10.3$ M_{Jup}. Dynamical simulations would better inform the allowed values for the orbital eccentricity of the massive companion to ensure stability, but these are beyond the scope of this work. In the end, continued RV monitoring is required to reveal the true nature of this companion.

TOI-1736 is the only star of our eight systems that is slightly evolved, and the only system for which we detect the full orbit
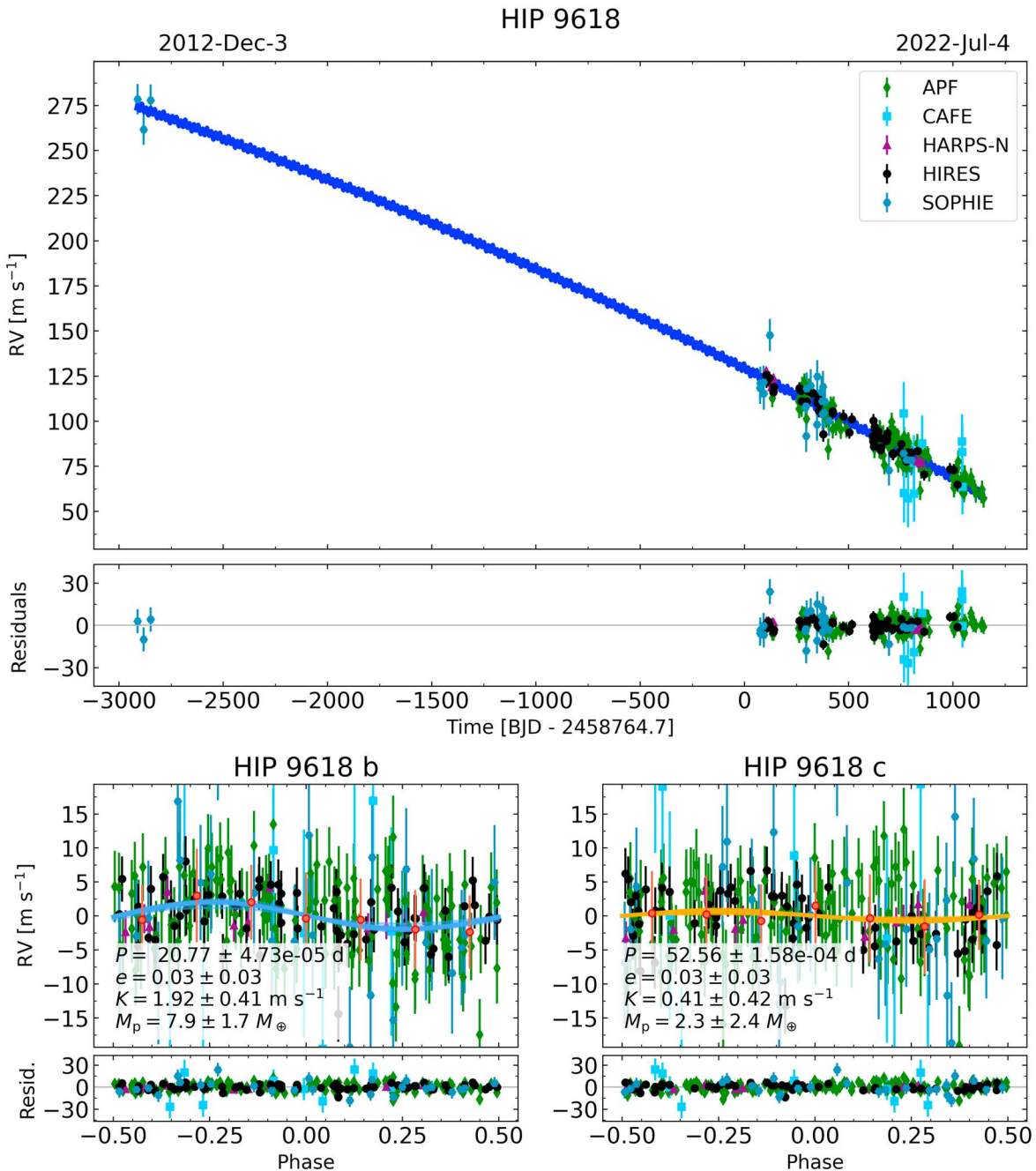
Figure 8. The RV portion of a joint model for HIP 9618 that includes the CAFE, HARPS-N, and SOPHIE RVs from O23 in addition to the APF-Levy and Keck-HIRES data from this work. The figure description is the same as for Figure 6. This RV model also includes a curvature term in addition to the linear trend, in order to mimic the adopted solution from O23. The results of this model are consistent with our joint model of the APF-Levy and Keck-HIRES RVs alone.

of a massive, presumably nontransiting planet. The system's architecture is intriguing: a transiting sub-Neptune interior to a temperate super-Jovian and a massive, potentially nonplanetary companion. Given the system's architecture, evolutionary state, and precise physical properties, TOI-1736 b (TSM = 55 ± 11) represents an attractive opportunity for atmospheric observations with JWST.

11. RV Modeling with `RadVel`

As alluded to in Section 10, we also used the `RadVel` software package (Fulton et al. 2018) to measure the masses of the planets in our sample. We did this in order to compare the planet mass measurements from our custom joint modeling

framework with a more established RV modeling tool (e.g., Rosenthal et al. 2021; Teske et al. 2021). For each system, we used `RadVel` to model the RVs independent of the TESS photometry. We also used `RadVel` to experiment with a GP kernel that has fewer free parameters than that described in Section 9.3. In general, we find all of the `RadVel` results are consistent with our adopted joint models.

11.1. Keplerian-only Modeling

First, we attempted to replicate the results of our joint models with Keplerian-only `RadVel` models of the RVs (i.e., no GPs). For each system, we used P, T_c, K, and $\sqrt{e}\cos\omega$ and $\sqrt{e}\sin\omega$ to describe the orbit of each planet. For transiting planets,
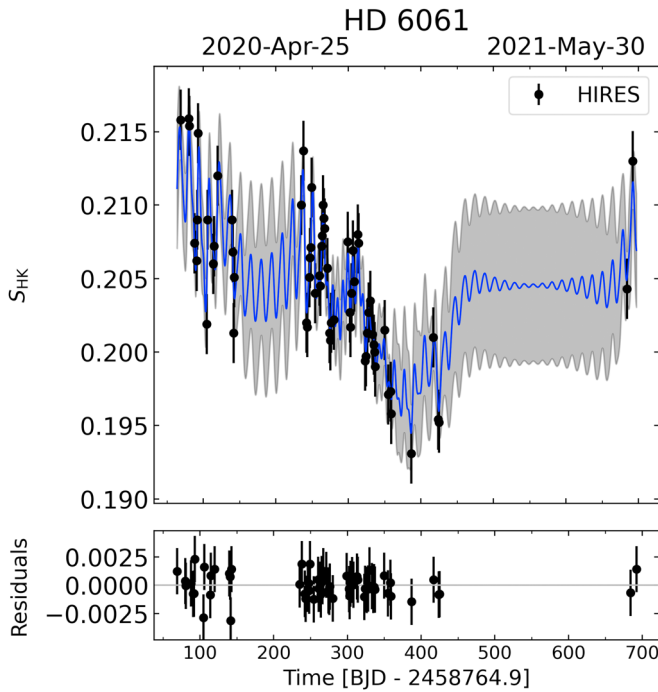
HD 6061

Figure 9. The S_{HK} portion of the joint model for HD 6061, in which GPs with some shared hyperparameters are simultaneously fit to the RVs and the Keck-HIRES S_{HK} values. The GP kernel is described in Section 9.3. The best-fitting value of the GP period is $P_{rot} = 13.9 \pm 1.5$ days. See Figure 23 for the photometry and RV portions of this joint model. The GP posterior prediction is shown as the blue line surrounded by a 1σ error envelope. The Keck-HIRES S_{HK} values are shown as the black points with 1σ errors, where the measurement error on each S_{HK} value has been added in quadrature with the a jitter term that has been fit to the data. Residuals are shown in the bottom panel.

P and T_c were fixed to the posterior median values resulting from our adopted joint model. For the nontransiting planet TOI-1736 c, we placed Gaussian priors on P and T_c using the posteriors of our joint model. For each system, we included an offset (with prior $\mathcal{U}[-250, 250]$ m s^{-1}) and jitter term (with prior $\mathcal{U}[0, 20]$ m s^{-1}) for each RV instrument. We also included a linear RV trend to see whether or not it was favored by the AIC. The only other prior we included was to force $e < 0.99$.

We performed an MAP fit to the data and conducted posterior estimation with emcee (Foreman-Mackey et al. 2013). We followed the default prescriptions for burn-in criteria, number of walkers, number of steps, and convergence criteria from Fulton et al. (2018). We found that for each system, each planet's mass measurement was entirely consistent between our adopted joint model and our Keplerian-only RadVel model. The RadVel models show that the orbits of all planets (save for TOI-1736 c) are consistent with being circular and for all but HIP 9618 and TOI-1736, a linear RV trend is not favored by the AIC.

11.2. Gaussian Process Modeling

When using GPs for regression, choosing a kernel can be somewhat subjective, so it is useful to compare models that use different kernels in order to ensure that the results are not biased. In the case of our joint model, the kernel we employ (see Section 9.3) is relatively complex compared to, e.g., a squared exponential kernel or a Matérn 3/2 kernel. The kernel introduces 11 free parameters for a system with both APF-Levy

and Keck-HIRES data: six amplitude parameters ($\eta_{dec,i}$ and $\eta_{rot,i}$ for each instrument, i = APF-Levy RV, Keck-HIRES RV, and Keck-HIRES S_{HK}), four shared hyperparameters to describe the rotation term (Q_0, δQ, P_{rot}, and f), and one shared hyperparameter to describe the exponentially decaying term (ρ_{dec}). The GP hyperparameters are summarized in Table 7. As mentioned at the end of Section 9.3, we ultimately chose this kernel after experimenting with its variants. The authors of exoplanet also suggest that it is a good kernel for modeling stellar activity.[42]

As a sanity check, we attempted to model the RVs in RadVel using a GP kernel with fewer hyperparameters. For instrument i, the kernel (sometimes referred to as the "quasiperiodic" kernel; e.g., Grunblatt et al. 2015) quantifies covariance between data observed at times t and t' as

$$k_i(t, t') = \eta_{1,i}^2 \exp\left[-\frac{(t - t')^2}{\eta_2^2} - \frac{\sin^2\left(\frac{\pi(t - t')}{\eta_3}\right)}{2\eta_4^2}\right]. \quad (20)$$

η_{1-4} are the hyperparameters: $\eta_{1,i}$ represents the amplitude of the covariance for instrument i, η_2 is interpreted as the evolutionary timescale of active stellar regions, η_3 is interpreted as the stellar rotation period, and η_4 is the length scale of the covariance's periodicity. The hyperparameters are shared between instruments save for the amplitudes, $\eta_{1,i}$. To incorporate this GP into our RadVel models, we first trained the GP by fitting it to the Keck-HIRES S_{HK} values. The posteriors of η_2, η_3, and η_4 resulting from the training were then used as numerical priors for these hyperparameters when fitting the RVs. We also placed a uniform prior of $\mathcal{U}[0, 20]$ m s^{-1} on $\eta_{1,i}$. This process is an in-series analog to our joint model's simultaneous fitting of the RVs and Keck-HIRES S_{HK} values.

For the GP training on the S_{HK} values, we placed a uniform prior of $\mathcal{U}[0, 1]$ on $\eta_{1,i}$ and broad Jeffreys priors (Jeffreys 1946) of $\mathcal{J}[1, 500]$ days on η_2 and η_3. For η_4, we used the Gaussian prior $\mathcal{N}(0.5, 0.05)$ per Haywood et al. (2018). Training the GP on the Keck-HIRES S_{HK} values did not result in clear constraints on the hyperparameters for HD 25463, HD 135694, and HD 6061. For HD 25463, we also tried fitting the S_{HK} values using a prior of $\mathcal{N}(4, 1.5)$ days on η_3 (like we did for P_{rot} when using the joint model's more complicated kernel). However, posterior estimation with emcee failed to converge when adding the trained GP to the RadVel model of the RVs, which is likely a symptom of the lack of constraints on the other GP hyperparameters.

For HD 135694, during the GP training, we replaced the Jeffreys prior on η_3 with a relatively broad Gaussian, $\mathcal{N}(32.5, 7.5)$ days, to hone in on the 32.5 day signal that we identified in the GLS periodograms of the RV residuals and the Keck-HIRES S_{HK} values. Adding the trained GP to the RadVel model of the RVs described in Section 11.1, we find $M_b = 7.3 \pm 1.9$ $M_\oplus$ for HD 135694 b. This mass is consistent with our joint model's result of $M_b = 5.7 \pm 2.1$ $M_\oplus$.

For HD 6061, the GP training on the S_{HK} values resulted in a bimodal posterior for η_3 with peaks near 28 days and 14 days. Posterior estimation for a fit to the RVs using the trained GP did not converge due to walkers getting caught at one of the two η_3 peaks. As discussed in Section 8.3, it seems as though

---

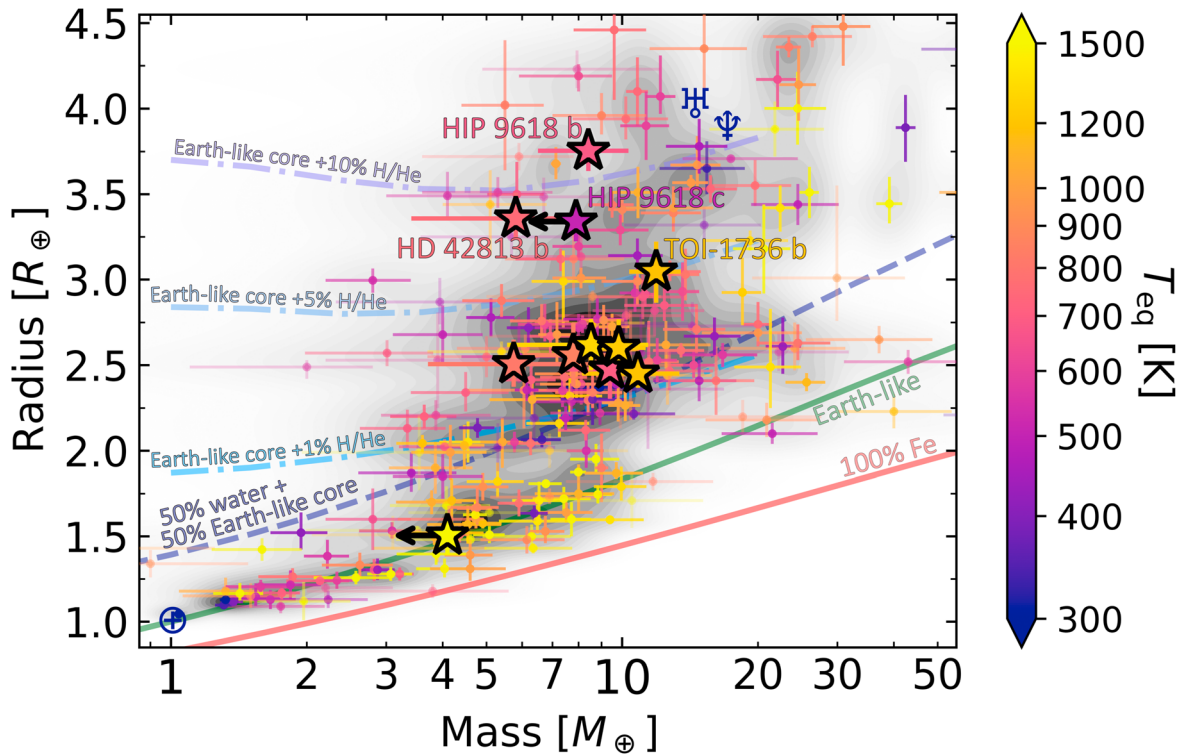[42] https://gallery.exoplanet.codes/tutorials/stellar-variability/

Figure 10. The mass–radius diagram for small planets. Data comes from the NASA Exoplanet Archive's planetary systems table, as accessed on 2022 November 17 (NASA Exoplanet Archive 2022). Planets with mass and radius measurements to better than 50% and 15% fractional precision, respectively, are shown as the circles with 1σ error bars. The opacity of the points is proportional to mass measurement precision (i.e., a less-precise mass measurement translates to a more transparent marker). Color corresponds to equilibrium temperature assuming zero Bond albedo and full day–night heat redistribution. Underlying contours come from Gaussian kernel density estimation of the confirmed planets described above. The 11 transiting planets from this work are overplotted as the stars. Mass upper limits (98% confidence) are plotted for HD 25463 c (yellow star near the radius valley) and HIP 9618 c (labeled). A handful of composition curves are plotted for reference (Lopez & Fortney 2014; Zeng et al. 2016, 2019). The curves of H/He envelopes atop Earth-like cores come from Lopez & Fortney (2014) and are chosen for a planet receiving 10× Earth's incident flux (i.e., $T_{eq} \approx 500$ K) orbiting a 10 Gyr-old, solar-metallicity star. The 50% water plus 50% Earth-like composition curve from Zeng et al. (2019) is calculated for a fixed temperature of 700 K at 100 bar, which determines the planetary model's specific entropy. Note that familiar features of the planet radius distribution are now visible as two-dimensional features in the mass–radius plane. These include the radius valley (Fulton et al. 2017; Van Eylen et al. 2018), with center near 6 $M_\oplus$ and 1.8 $R_\oplus$, and the radius cliff (e.g., Kite et al. 2019), as seen by in the steep drop-off in the number of planets around 3 $R_\oplus$.

$\eta_3 \approx 14$ days may be a better representation of the true rotation period for this G0 dwarf. As an experiment, we repeated the training but this time we replaced the Jeffreys prior on η_3 with $\mathcal{N}(14, 1.5)$ days. This is the same prior we placed on P_{rot} in our adopted joint model (see Section 10.7). Adding this trained GP to the RV model, we find $M_b = 12.6 \pm 2.4\ M_\oplus$ for HD 6061 b. This result is consistent with the mass measurement from our adopted, GP-enabled joint model of $M_b = 10.8 \pm 2.7\ M_\oplus$. On the other hand, this GP-enabled RadVel model is in slight disagreement with the results of our Keplerian-only joint model of the data, which finds $M_b = 7.8 \pm 2.9\ M_\oplus$. Continued Doppler monitoring of this moderately active system should help cast light on the nature of the stellar activity signal.

12. Planet Bulk Composition

Here we contextualize the 11 transiting planets from this sample in the mass–radius diagram (Figure 10). We compare the planets' locations relative to models from Lopez & Fortney (2014) and Zeng et al. (2016, 2019), and interpolate over theoretical grids of composition to infer planet bulk properties (Piaulet et al. 2021). The planets fall into three categories: super-Earths (HD 25463 c), typical sub-Neptunes (HIP 8152 b and c, HD 25463 b, TOI-669 b, HD 135694 b, and HD 6061 b), and puffy sub-Neptunes (HD 42813 b, HIP 9618 b and c, and TOI-1736 b).

12.1. The Mass–Radius Diagram

In our sample, HD 25463 c sits alone below the radius valley. While we do not measure a precise mass for the planet ($M_p < 4.1\ M_\oplus$ at 98% confidence), our upper limit implies that HD 25463 c's core contains some fraction of volatiles or ices. Alternatively, the planet's core could be iron-poor. The planet is an attractive target for follow-up, though its small Doppler signal ($< 1.5\ \mathrm{m\,s^{-1}}$) relative to the star's RV jitter ($\approx 7\ \mathrm{m\,s^{-1}}$) has frustrated our mass measurement efforts with APF-Levy and Keck-HIRES.

Six planets land on the mode of the sub-Neptune distribution near 8 $M_\oplus$ and 2.3 $R_\oplus$ (clockwise from left in Figure 10: HD 135694 b, HIP 8152 b, HD 25463 b, TOI-669 b, HD 6061 b, and HIP 8152 c). These planets have bulk densities that are roughly consistent with a 0.1%–2% H_2 envelope by mass sitting atop an Earth-like core. However, at low H_2 envelope mass fractions, the Lopez & Fortney (2014) models become degenerate with those invoking a water-rich bulk composition (i.e., an Earth-like core with a small H_2 envelope becomes indistinguishable from a planet made of half ice and half rock; Aguichine et al. 2021). Indeed, such "water worlds" are predicted by formation theory (e.g., Raymond et al. 2018).

The last four planets (HD 42813 b, HIP 9618 b, HIP 9618 c, and TOI-1736 c) sit just beyond the "radius cliff," the steep drop-off in planet occurrence around 3 $R_\oplus$ (e.g., Kite et al. 2019) and are all seemingly consistent with having a

Table 9
smint Results

Planet Name	LF14 f_{env}	Z16 f_{H_2O}	A21 f_{Fe}	A21 f_{H_2O}
HD 25463 c	<0.2	60 ± 30	52 ± 30	<15
HD 6061 b	0.9 ± 0.4	60 ± 24	45 ± 30	29 ± 11
HIP 8152 c	1.5 ± 0.8	67 ± 24	43 ± 30	44 ± 18
HD 135694 b	1.9 ± 0.7	83 ± 16	42 ± 30	57 ± 15
HIP 8152 b	1.9 ± 0.9	77 ± 20	43 ± 31	54 ± 18
TOI-669 b	1.4 ± 0.7	78 ± 19	42 ± 30	41 ± 14
HD 25463 b	1.6 ± 0.7	78 ± 20	44 ± 31	47 ± 16
TOI-1736 b	3.3 ± 0.9	⋯	⋯	⋯
HIP 9618 c	7.0 ± 1.2	⋯	⋯	⋯
HD 42813 b	6.3 ± 1.1	⋯	⋯	⋯
HIP 9618 b	9.2 ± 1.2	⋯	⋯	⋯

Note. Results from our interpolation on the grids of planet composition from Lopez & Fortney (2014), Zeng et al. (2016), and Aguichine et al. (2021). All values are shown in percent. Planets appear in order of increasing radius. For the LF14 grid, f_{env} is the fraction of the planet's mass contained in an H/He-dominated, solar-metallicity envelope, assuming a rocky core composition. For Z16, f_{H_2O} is the planet's core H_2O mass fraction, assuming the planet is composed of H_2O ice and silicates. For A21, f_{Fe} is the fraction of the planet's refractory core that is iron, with the rest of the core being made up of silicates (e.g., $f_{Fe} \approx 32\%$ for Earth). f_{H_2O} is the total mass fraction of the planet's H_2O content, which is contained in a supercritical fluid layer and a steam atmosphere. For HD 25463 c, the upper limit on f_{env} reflects 98% confidence for the case where S_p is fixed to 1000 $S_\oplus$ (the upper limit of the LF14 grid) in place of using the planet's actual installation, $S_p \approx 1400$ $S_\oplus$. Similarly, for the A21 grid, the f_{Fe} and f_{H_2O} values represent the case where T_{eq} has been fixed to 1300 K (the upper limit of the grid) in place of HD 25463 c's actual equilibrium temperature of $T_{eq} \approx 1700$ K. The upper limit on f_{H_2O} reflects 98% confidence. For the four puffy sub-Neptunes (TOI-1736 c, HIP 9618 b, HD 42813 b, and HIP 9618 c) their large radii demand an H/He envelope. Without one, both the Z16 and A21 f_{H_2O} values rail to 100%, and the planet mass is inflated such that it is inconsistent with the results of our joint photometry and RV analysis.

substantial (>2%) fraction of their mass in an H_2 envelope. Curiously, the densest of these planets, TOI-1736 b, is also the only planet orbiting a subgiant star. The in-transit detection of He I absorption for TOI-1736 b would provide evidence of ongoing photoevaporation (e.g., Zhang et al. 2022), which might have started when TOI-1736 evolved off the main sequence.

12.2. smint Analysis

To make more quantitative statements about possible planet bulk properties, we used the Structure Model INTerpolator tool (smint; Piaulet et al. 2021) to interpolate over the theoretical grids of planet composition from Lopez & Fortney (2014), Zeng et al. (2016), and Aguichine et al. (2021). Hereafter, we refer to these works as LF14, Z16, and A21, respectively.

The LF14 grid assumes a planet is composed of an H/He-dominated, solar metallicity, envelope atop a rocky core. The planet is then thermally evolved over time according to the methods of Lopez et al. (2012), but ignoring the influence of XUV- and EUV-driven photoevaporation. To interpolate over the LF14 grid, smint takes inputs of planet mass, installation flux, and system age and determines an H/He envelope mass fraction (f_{env}) that best matches the observed planet radius. For each of the transiting planets in our system, we placed Gaussian priors on planet mass, radius, and installation flux according to
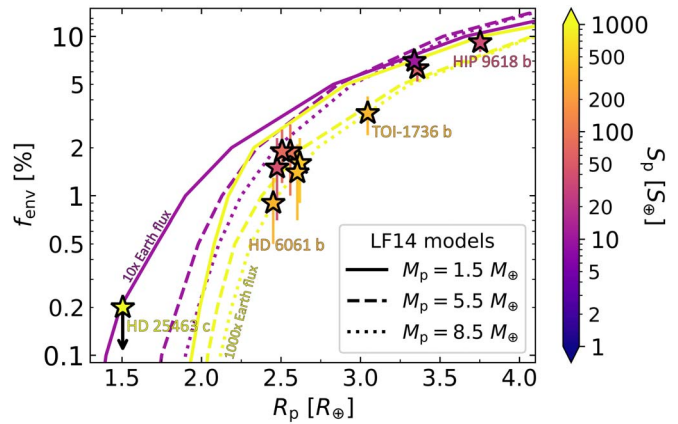

Figure 11. Inferred values of f_{env} as a function of planet radius for the 11 transiting planets. f_{env} values are estimated by applying smint to the grid of thermal evolution from LF14. Several slices of the LF14 grid are plotted for reference. Color corresponds to installation flux in Earth units. An upper limit (which reflects 98% confidence) is shown for HD 25463 c, whose actual installation ($S_p \approx 1400$ $S_\oplus$) surpasses the upper limit of the LF14 grid ($S_p = 1000$ $S_\oplus$).

our joint modeling results and a uniform prior on f_{env} from 0.1%–20%. Since age is typically difficult to infer for main-sequence stars, we placed a uniform prior on the age of each system between 1 and 10 Gyr (including for the subgiant TOI-1736).

We explored the posteriors of planet mass, installation flux, system age, and f_{env} using emcee. Each emcee sampler used 50 chains with each chain taking at least 5000 steps. Chains continued sampling until they converged or the chains reached 10^4 steps. Convergence was determined by enforcing that each chain was at least $50\times$ longer than the maximum autocorrelation time across all parameters (τ_{max}; Goodman & Weare 2010) and that the maximum relative change in τ_{max} between convergence checks (every 100 steps) was <1%. After sampling was complete, the first 60% of steps in each chain were discarded as burn-in and the remaining samples were concatenated. The inferred values of f_{env} for each planet are summarized in Table 9. Figure 11 plots the inferred f_{env} values as a function of planet radius.

For HD 25463 c, the planet is too highly irradiated ($S_p \approx 1400$ $S_\oplus$) for the LF14 grid (which has an upper limit of $S_p = 1000$ $S_\oplus$). To place an upper limit on f_{env} for HD 25463 c, we fixed $S_p = 1000$ and placed a uniform prior on M_p between 1.5 $M_\oplus$ and 4.1 $M_\oplus$, where the lower limit comes from the mass of a 1.5 $R_\oplus$ planet lying on the 50% water and 50% rock isocomposition curve from Zeng et al. (2016), and the upper limit comes from our Doppler observations. We use the 50% water and 50% rock isocomposition curve as a fiducial lower bound on the mass of HD 25463 c because cosmic abundance measurements suggests that 50% should be an upper limit on planet core water mass fractions.

Recently, the idea that small planets may owe a substantial fraction of their mass to H_2O ice, liquid, and/or vapor—as opposed to strictly being composed of rock and H/He—has found observational evidence (e.g., Zeng et al. 2019; Luque & Pallé 2022) to support theories of ice-rich core formation (e.g., Raymond et al. 2018). To explore these so-called "water world" compositions, we also applied smint to the grid from Z16, which models planets as a mixture of liquid H_2O, high pressure H_2O ice, and silicates. Such a composition resembles
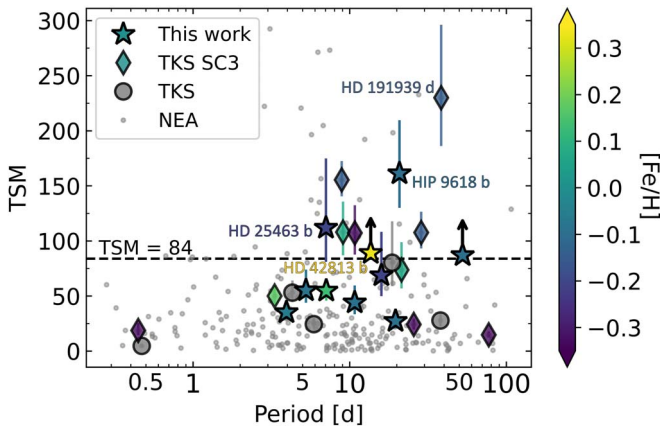
Figure 12. The same planets from Figure 10 but now plotted in terms of orbital period vs. TSM, a JWST S/N proxy (Kempton et al. 2018). Planets from the NASA Exoplanet Archive (NEA) are shown as the gray dots. Confirmed planets from the TESS-Keck Survey (TKS) are shown as the gray circles. Planets from TKS Science Case 3 (SC3), TKS' follow-up of targets amenable to atmospheric characterization, are shown as the diamonds and stars where marker color represents host star metallicity, as measured using [Fe/H]. TKS SC3 planets from this work are the stars, where the lower limits for HD 42813 b and HIP 9618 c reflect 98% confidence. HD 25463 c is not shown because its mass constraint is too uninformative. The horizontal dashed line at TSM = 84 marks the TSM cutoff suggested by Kempton et al. (2018) for scheduling atmospheric observations of planets with $2.75 < R_p < 4 R_\oplus$.

that of the solar system's icy moons. To interpolate over the Z16 grid, smint tunes planet mass and core H_2O mass fraction (f_{H_2O}) to best-fit the observed planet radius. We placed a uniform prior on f_{H_2O} between 0% and 100%. The posterior estimation was analogous to our procedure for the LF14 grid. f_{H_2O} estimates are summarized in Table 9.

One caveat of the Z16 model is that it does not necessarily apply to the short-period sub-Neptunes identified by TESS, since these planets are generally too highly irradiated to have all of their H_2O in the solid and liquid phases. More applicable are the models of A21, in which Earth-like cores are surrounded by a supercritical H_2O fluid layer and a steam-dominated envelope. To interpolate on the A21 grid, we fit the following free parameters to match the measured planet radius: the planet core mass fraction (f_{Fe}; the fraction of the planet's refractory core that is iron, with the rest of the core being made up of silicates), planet water mass fraction (f_{H_2O}; which includes both the supercritical fluid and steam envelope components), irradiation temperature (for which we use T_{eq} assuming zero Bond albedo and full day–night heat redistribution), and planet mass. We placed uniform priors on f_{Fe} and f_{H_2O} between 0% and 100% and used informed Gaussian priors on T_{eq} and M_p according to the results of our stellar characterization and joint photometry and RV analysis. The emcee sampling then proceeded following our method for the LF14 and Z16 grids. f_{Fe} and f_{H_2O} estimates are summarized in Table 9.

Similar to the case of HD 25463 c and the LF14 grid, the A21 grid has an upper limit of $T_{eq} = 1300$ K, yet the planet has $T_{eq} \approx 1700$ K. To estimate an upper limit on f_{H_2O} for HD 25463 c, we fixed T_{eq} to 1300 K and placed a uniform prior on M_c between 1.5 $M_\oplus$ and 4.1 $M_\oplus$ (where we have again bounded M_p below by the 50% water and 50% rock isocomposition curve and above by our Doppler observations).

Our interpolation on the Z16 grid results in systematically higher f_{H_2O} values as compared to the A21 grid (typically 60%–

80% versus 30%–50%). We interpret this as a symptom of the distinction made above, where the A21 model is better-suited to describe highly irradiated water worlds while the Z16 grid is more applicable to planets at low instellation flux. Since the A21 model can place water in an extended envelope, less overall water is needed to match a planet's radius. In the Z16 model, however, all of the water must go into the liquid and solid phases, which makes it difficult to replicate intermediate- to low-density sub-Neptunes without large values for f_{H_2O}. Cosmic abundance measurements suggest that planetesimals forming beyond the snow line should be a 1:1 mixture of H_2O ice and rock. To this end, we note that $f_{H_2O} \gtrsim 50\%$ is unphysical, so the results of our interpolation on the Z16 grid should be treated with care. For primordially icy cores, thermal processes such as radiogenic heating also work to reduce f_{H_2O} below 50% (Grimm & McSween 1993; Monteux et al. 2018).

Here we summarize the results of our bulk composition analysis. The super-Earth HD 25463 c is too low-mass and too highly irradiated to host a volatile envelope. The Z16 grid suggests that the planet's core has a high water content, but given our comments above, the Z16 f_{H_2O} estimates should be treated with care at the high equilibrium temperatures of the planets in our sample. This is not to necessarily say that HD 25463 c's core is not ice-rich, however. Indeed, the planet's core may contain some amount of volatiles given our mass upper limit ($M_p < 4.1 M_\oplus$). Perhaps volatiles have been dissolved into the planet's core as a result of the interaction between a reactive iron core, silicate mantle, and a primordial envelope, which has since been stripped away (Schlichting & Young 2022). Alternatively, HD 25463 c may have a rocky core that is iron-poor; using our high-resolution, iodine-free Keck-HIRES spectra, we find that HD 25463 has [Fe/H] = -0.20 ± 0.09 dex.

For the planets at the mode of the sub-Neptune mass–radius distribution (HIP 8152 b and c, HD 25463 b, TOI-669 b, HD 135694 b, and HD 6061 b), f_{env} and f_{H_2O} are degenerate. These planets can be reasonably explained either as an Earth-like core with a small ($1\% \lesssim f_{env} \lesssim 2\%$) H/He envelope or as an irradiated water world consisting of an Earth-like core and roughly 30%–50% of their mass in a supercritical water layer beneath a steam atmosphere. Again, while the Z16 grid suggests that these planets have $f_{H_2O} \gtrsim 60\%$, this is an overestimate of the water content. Transmission spectroscopy to measure the atmospheric H/O ratio may help break the degeneracy between these two compositions.

Finally, we find that the puffy sub-Neptunes (HD 42813 b, HIP 9618 b and c, and TOI-1736 b) all demand a massive H/He envelope ($3\% \lesssim f_{env} \lesssim 10\%$). Attempting to explain these planets using the Z16 and A21 models resulted in planet masses that were inconsistent with our joint photometry and RV analysis and water mass fractions that railed to 100%. These planets could also have a slightly less-massive H/He envelope if their cores contain some fraction of H_2O ice, but they must host some sort of H/He envelope regardless of their water content.

13. Prospects for Atmospheric Characterization

The sub-Neptune regime of the mass–radius plane is host to a confluence of theoretical models of bulk composition, making it difficult to infer the interiors of these planets from mass and radius measurements alone (Valencia et al. 2007; Adams et al. 2008; Zeng et al. 2019; Otegi et al. 2020). Measurements of
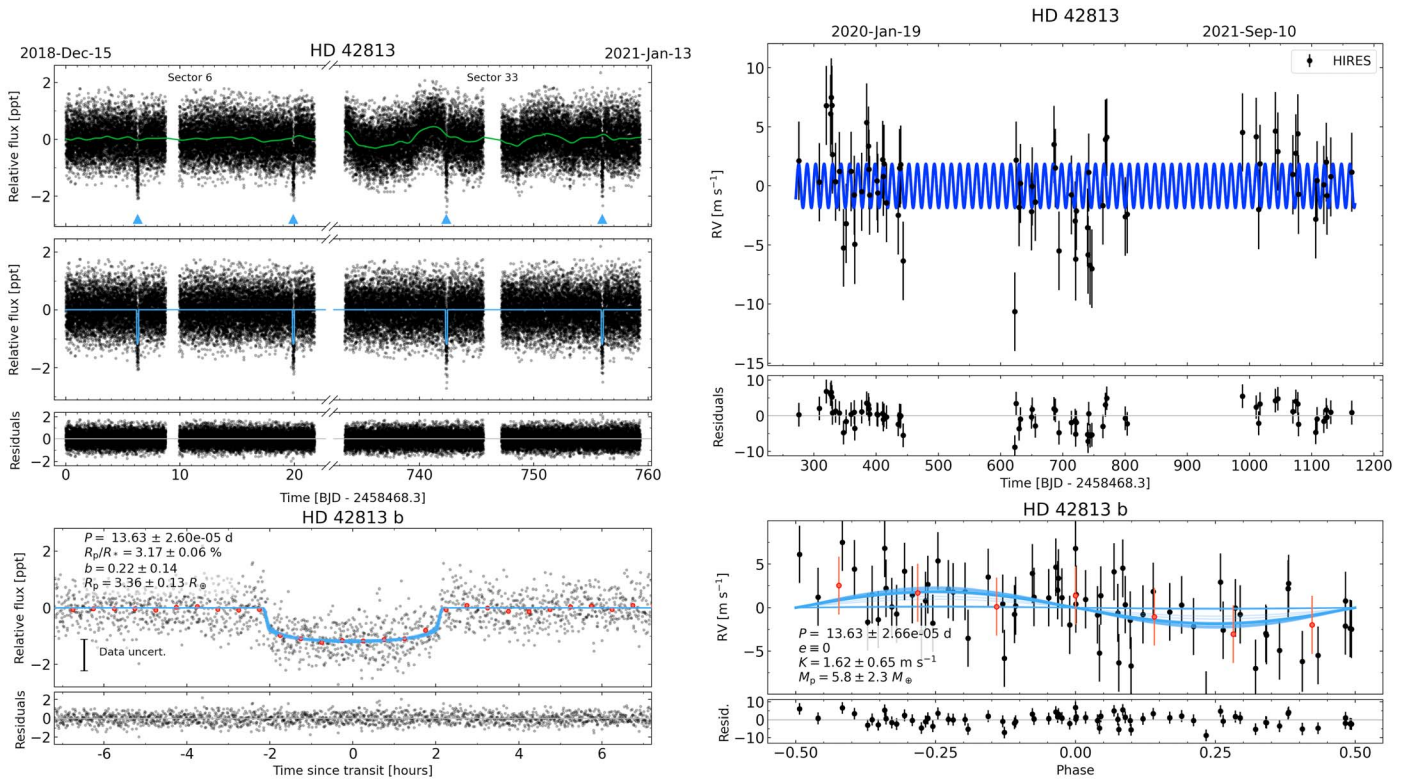
Figure 13. Our joint modeling results for HD 42813. The figure description is the same as for Figure 6.
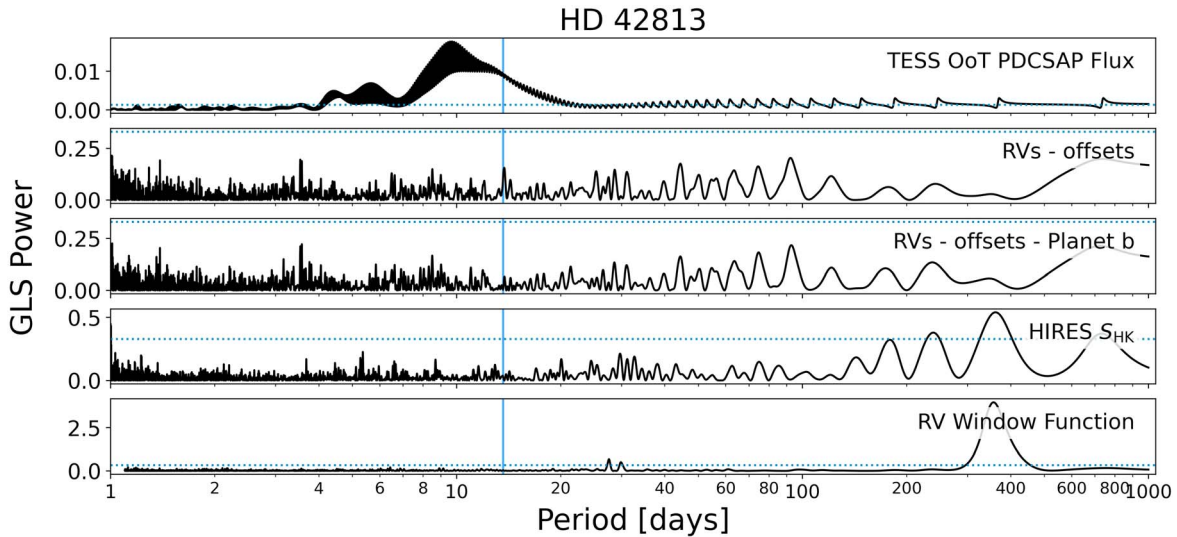

Figure 14. GLS periodograms for HD 42813. The figure description is the same as for Figure 7.

atmospheric metallicity, however, may be able to break these degeneracies and cast light on planet composition, which can, in turn, inform theories of formation and evolution (Rogers & Seager 2010). What are the prospects for characterizing the atmospheres of the transiting planets presented in this work?

Kempton et al. (2018) introduced the now widely used TSM (see Equation 1) to quantify how amenable a planet might be to transit observations with JWST. TSM is a proxy for the expected S/N of a 10 hr JWST NIRISS-SOSS observing program assuming a cloud-free, solar-metallicity, H_2-dominated planet atmosphere. Figure 12 shows the same planets from Figure 10

but now plotted by TSM as a function of orbital period. Confirmed planets from the TKS SC3 program (the survey's planet atmospheres science theme) are plotted as diamonds, and transiting planets from this work are shown as stars. Based on TSM value, some of the most exciting TKS SC3 systems for atmospheric characterization include the multitransiting planet systems HD 191939 (Badenas-Agusti et al. 2020; Lubin et al. 2022; Orell-Miquel et al. 2023) and HIP 9618 (O23; this work).

As mentioned in Section 1.2, while not every planet from this work has an extraordinarily high TSM value (e.g., HIP 8152 b and c), we emphasize the results of Batalha et al.

(2023). The authors stress that the best samples for inferring population-level characteristics of small planets via transmission spectroscopy are not necessarily composed of the best individual targets. Furthermore, a high TSM value is not a guarantee for the detection of atmospheric molecular features given the seeming ubiquity of clouds and hazes (e.g., Gao et al. 2021 and references therein). Multiple factors should be considered in addition to TSM value when selecting targets for atmospheric follow-up observations, including a planet's location in the mass–radius plane, host star properties, and system multiplicity, among others. To these ends, the transiting planets in this work represent a valuable addition to the sample of viable targets for space-based atmospheric observations.

Detailed characterization of small planet transmission spectra requires a precise planet mass measurement in order to break the degeneracy between planet surface gravity and atmospheric mean molecular weight. Batalha et al. (2019) demonstrated that with a 5σ planet mass, uncertainty in the atmospheric characterization process is dominated by the quality of the transmission spectra. On the other hand, a 2σ mass is still useful for atmospheric characterization, but the dominant source of uncertainty remains the degeneracy between surface gravity and mean molecular weight. Note that 5σ precision is still lacking for several planets presented in this work. We encourage future Doppler surveys to continue to monitor these targets in order to improve their mass measurements. It is unclear why we did not reach higher precision for some of the planet mass measurements given our large number of RVs (at least 60 Keck-HIRES RVs for each target), but the possible culprits may include unmitigated stellar activity (e.g., perhaps for HD 6061 b) and/or inadequate RV measurement precision (e.g., in the case of the low-mass planet, HD 25463 c).

Planets are often selected for Doppler follow-up and subsequent atmospheric characterization because of their novelty. This selection bias disfavors targets that are in fact the most common products of planet formation in our Galaxy. The mode of the sub-Neptune mass–radius distribution can now be clearly identified around 8 $M_\oplus$ and 2.3 $R_\oplus$. With mass and radius held fixed, how might changes in installation, host star metallicity, and/or system multiplicity affect the (atmospheric) composition of different planets on the mode? Much of the JWST Cycle 1 exoplanet transit observations are dedicated to hot, giant planets and small planets orbiting cool stars, yet few are earmarked for planets sitting on the mode of the sub-Neptune mass–radius distribution (HD 15337 c is the only such planet in Cycle 1). Six planets from this work all land on the mode (HIP 8152 b and c, HD 25463 b, TOI-669 b, HD 135694 b, and HD 6061 b). These planets have similar masses and radii, but span more than an order of magnitude in installation flux. Furthermore, the five host stars are all similar in mass and $T_{\rm eff}$. Precisely characterized planets sitting on the mode of the sub-Neptune mass–radius distribution offer a unique opportunity for inter-system comparison of atmospheric composition by way of their commonality.

Regarding planet multiplicity, three of the eight systems in this work, HIP 8152, HD 25463, and HIP 9618, host multiple transiting planets. Multiplanet systems are testbeds for theories of planet formation and evolution. Systems with multiple transiting planets are even more valuable, as they enable the intra-system comparison of atmospheric composition. HIP 8152 b and c are nearly identical in physical properties save for installation flux, offering a rare opportunity to compare the atmospheric composition of two planets while freezing out all other nuisance parameters (e.g., planet bulk density, stellar properties, and system age). HD 63935 b and c, and also TKS SC3 planets, represent a similar case of precisely characterized twin sub-Neptunes orbiting a G dwarf (Scarsdale et al. 2021). Like HIP 8152 and HD 63935, HIP 9618 is G dwarf with multiple transiting sub-Neptunes but at lower installation flux.

14. Conclusion

In this paper, we used nearly 2 yr' worth of Doppler monitoring to report mass measurements for 11 planets transiting eight bright host stars. We also reported the discovery and confirmation of a super-Jovian-mass planet on a moderately eccentric orbit. Four systems, HIP 8152, HD 25463, HIP 9618, and TOI-1736, host multiple planets, with the first three systems hosting multiple transiting planets. Two systems, HIP 9618 and TOI-1736, also exhibit long-term RV trends, indicative of distant, massive companions. In addition to these planet confirmations, we also report what is likely a gravitationally bound mid-M dwarf companion (TIC 600433892) to HD 6061. The two stars have a sky-projected separation of 200 au.

Planet properties were derived in a homogeneous manner using a joint photometry and RV modeling framework, and careful consideration was given to mitigating signs of stellar activity in the spectroscopic data. We contextualized these planets in the mass–radius diagram and examined their prospects for future atmospheric characterization. We highlight HIP 9618 b as a very attractive target for atmospheric characterization with JWST. A summary of derived planet properties can be found in Table 8. A full list of system parameters, including stellar properties, can be found in Tables 10–17.

Thanks in large part to the wealth of new discoveries from TESS, long-term Doppler follow-up continues to enrich the mass–radius diagram. As we enter the era of JWST, measurements of atmospheric metallicity will hopefully disambiguate the interior compositions of these planets and inform our understanding of the physics of their formation.

Appendix A
Joint Modeling Results

This appendix contains the figures (Figures 15–26) that summarize the results of our joint analysis, as well as tables (Tables 10–17) of measured and derived stellar and planetary parameters.

Table 10
HIP 8152 System Parameters

Stellar Parameters				
Parameter	Symbol	Units	Value	Provenance
Identifying information				
TOI ID			266	Guerrero
TIC ID			164767175	Guerrero
R.A.		deg (J2000)	26.20	Gaia DR3
Decl.		deg (J2000)	−18.40	Gaia DR3
Parallax	π	mas	9.83 ± 0.01	Gaia DR3
Johnson *V*-band apparent magnitude	V	mag	10.07 ± 0.03	TIC
J-band apparent magnitude	J	mag	8.85 ± 0.03	2MASS
K_s-band apparent magnitude	K_s	mag	8.45 ± 0.02	2MASS
Spectroscopy				
Effective temperature	$T_{\rm eff}$	K	5530 ± 110	SpecMatch-Emp
Metallicity	[Fe/H]	dex	-0.09 ± 0.09	SpecMatch-Emp
Ca II H & K emission	$\log_{10} R'_{\rm HK}$		-5.02 ± 0.05	Isaacson
Isochrone modeling				
Mass	M_*	$M_\odot$	0.91 ± 0.06	isoclassify
Radius	R_*	$R_\odot$	0.95 ± 0.04	isoclassify
Age		Gyr	8.2 ± 3.1	isoclassify
Transit modeling				
Limb-darkening parameter 1	u_1		0.46 ± 0.37	Joint model
Limb-darkening parameter 2	u_2		0.09 ± 0.39	Joint model
Planet Parameters				
Parameter	Symbol	Units	HIP 8152 b value	HIP 8152 c value
Measured quantities				
Orbital period	P	day	10.75101 ± 0.00006	19.6053 ± 0.0003
Time of inferior conjunction	T_c	BTJD	1758.620 ± 0.002	1751.195 ± 0.005
Occultation fraction	R_p/R_*		0.025 ± 0.001	0.024 ± 0.001
Impact parameter	b		0.67 ± 0.07	0.35 ± 0.19
Orbital eccentricity	e		<0.14	<0.28
Argument of periastron	ω	deg	161.8 ± 137.1	153.1 ± 83.2
RV semiamplitude	K	m s^{-1}	2.42 ± 0.53	2.40 ± 0.55
Derived quantities				
Orbital separation	a/R_*		20.9 ± 1.0	31.2 ± 1.5
Orbital semimajor axis	a	au	0.092 ± 0.002	0.138 ± 0.003
Radius	R_p	$R_\oplus$	2.56 ± 0.19	2.48 ± 0.19
Mass	M_p	$M_\oplus$	7.8 ± 1.8	9.4 ± 2.2
Bulk density	ρ	g cm^{-3}	2.5 ± 0.8	3.4 ± 1.1
Equilibrium temperature	$T_{\rm eq}$	K	855 ± 28	699 ± 23
Instellation flux	S_p	$S_\oplus$	88.9 ± 11.6	39.9 ± 5.2
Transit duration	$T_{\rm dur}$	hr	2.9 ± 0.1	4.3 ± 0.3
TSM			44 ± 14	27 ± 9
Additional Parameters				
Parameter	Symbol	Units	Value	
TESS photometric offset	$\mu_{\rm TESS}$	ppt	0.009 ± 0.006	
TESS photometric jitter	$\sigma_{\rm TESS}$	ppt	0.01 ± 0.01	
Keck-HIRES RV offset	$\gamma_{\rm HIRES}$	m s^{-1}	-1.44 ± 0.37	
Keck-HIRES RV jitter	$\sigma_{\rm HIRES}$	m s^{-1}	3.15 ± 0.30	

Note. Errors on stellar mass and radius have been inflated according to Tayar et al. (2022). Upper limits reflect 98% confidence. $T_{\rm eq}$ is calculated assuming zero Bond albedo and full day–night heat redistribution. The transmission spectroscopy metric (TSM) from Kempton et al. (2018) is a JWST S/N proxy. References for the provenance values in the order in which they appear in the table are as follows: "Guerrero" refers to the TESS Primary Mission TOI Catalog (Guerrero et al. 2021), TIC (TESS Input Catalog; Stassun et al. 2019), Gaia DR3 (Gaia Collaboration et al. 2016, 2023), 2MASS (Skrutskie et al. 2006), SpecMatch-Emp (Yee et al. 2017), "Isaacson" refers to the methods described in Isaacson & Fischer (2010), and isoclassify (Huber et al. 2017; Berger et al. 2020).

Table 11
HD 42813 System Parameters

			Stellar Parameters	
Parameter	Symbol	Units	Value	Provenance
Identifying information				
TOI ID			469	Guerrero
TIC ID			33692729	Guerrero
R.A.		deg (J2000)	93.05	Gaia DR3
Decl.		deg (J2000)	−14.64	Gaia DR3
Parallax	π	mas	14.71 ± 0.02	Gaia DR3
Johnson *V*-band apparent magnitude	V	mag	9.49 ± 0.03	TIC
J-band apparent magnitude	J	mag	8.06 ± 0.03	2MASS
K_s-band apparent magnitude	K_s	mag	7.59 ± 0.02	2MASS
Spectroscopy				
Effective temperature	$T_{\rm eff}$	K	5240 ± 110	SpecMatch-Emp
Metallicity	[Fe/H]	dex	0.33 ± 0.09	SpecMatch-Emp
Ca II H & K emission	$\log_{10} R'_{\rm HK}$		-4.98 ± 0.05	Isaacson
Isochrone modeling				
Mass	M_*	$M_\odot$	0.94 ± 0.06	isoclassify
Radius	R_*	$R_\odot$	0.97 ± 0.03	isoclassify
Age		Gyr	9.1 ± 3.5	isoclassify
Transit modeling				
Limb-darkening parameter 1	u_1		0.37 ± 0.23	Joint model
Limb-darkening parameter 2	u_2		0.18 ± 0.36	Joint model
		Planet Parameters		
Parameter	Symbol	Units	HD 42813 b value	
Measured quantities				
Orbital period	P	day	13.63083 ± 0.00003	
Time of inferior conjunction	$T_{\rm c}$	BTJD	1842.6015 ± 0.0007	
Occultation fraction	$R_{\rm p}/R_*$		0.0317 ± 0.0006	
Impact parameter	b		0.22 ± 0.15	
Orbital eccentricity	e		$\equiv 0$	
Argument of periastron	ω	deg	$\cdots$	
RV semiamplitude	K	m s^{-1}	1.62 ± 0.67	
Derived quantities				
Orbital separation	a/R_*		24.3 ± 0.8	
Orbital semimajor axis	a	au	0.109 ± 0.002	
Radius	$R_{\rm p}$	$R_\oplus$	3.36 ± 0.14	
Mass	$M_{\rm p}$	$M_\oplus$	5.8 ± 2.4	
Bulk density	ρ	g cm^{-3}	0.8 ± 0.4	
Equilibrium temperature	$T_{\rm eq}$	K	755 ± 21	
Instellation flux	$S_{\rm p}$	$S_\oplus$	54.1 ± 5.9	
Transit duration	$T_{\rm dur}$	hr	4.18 ± 0.05	
TSM			>89	
		Additional Parameters		
Parameter	Symbol	Units	Value	
TESS photometric offset	$\mu_{\rm TESS}$	ppt	0.02 ± 0.03	
TESS photometric jitter	$\sigma_{\rm TESS}$	ppt	0.170 ± 0.008	
Keck-HIRES RV offset	$\gamma_{\rm HIRES}$	m s^{-1}	-0.39 ± 0.42	
Keck-HIRES RV jitter	$\sigma_{\rm HIRES}$	m s^{-1}	3.21 ± 0.32	

Note. Table notes are the same as found at the bottom of Table 10. The lower limit on TSM reflects 98% confidence.

Table 12
HD 25463 System Parameters

Parameter	Symbol	Units	Value	Provenance
Stellar Parameters				
Identifying information				
TOI ID			554	Guerrero
TIC ID			407966340	Guerrero
R.A.		deg (J2000)	60.74	Gaia DR3
Decl.		deg (J2000)	9.20	Gaia DR3
Parallax	π	mas	22.13 ± 0.02	Gaia DR3
Johnson *V*-band apparent magnitude	V	mag	6.91 ± 0.02	TIC
J-band apparent magnitude	J	mag	5.95 ± 0.02	2MASS
K_s-band apparent magnitude	K_s	mag	5.71 ± 0.02	2MASS
Spectroscopy				
Effective temperature	$T_{\rm eff}$	K	6220 ± 110	SpecMatch-Emp
Metallicity	[Fe/H]	dex	-0.20 ± 0.09	SpecMatch-Emp
Ca II H & K emission	$\log_{10} R'_{\rm HK}$		-5.26 ± 0.05	Isaacson
Isochrone modeling				
Mass	M_*	$M_\odot$	1.19 ± 0.07	isoclassify
Radius	R_*	$R_\odot$	1.41 ± 0.07	isoclassify
Age		Gyr	3.1 ± 0.7	isoclassify
Transit modeling				
Limb-darkening parameter 1	u_1		0.42 ± 0.31	Joint model
Limb-darkening parameter 2	u_2		0.05 ± 0.33	Joint model

Parameter	Symbol	Units	HD 25463 b value	HD 25463 c value
Planet Parameters				
Measured quantities				
Orbital period	P	day	7.049144 ± 0.000009	3.044050 ± 0.000008
Time of inferior conjunction	T_c	BTJD	1978.3531 ± 0.0006	1980.314 ± 0.001
Occultation fraction	R_p/R_*		0.0170 ± 0.0004	0.0098 ± 0.0006
Impact parameter	b		0.72 ± 0.04	0.93 ± 0.01
Orbital eccentricity	e		$\equiv 0$	$\equiv 0$
Argument of periastron	ω	deg	$\cdots$	$\cdots$
RV semiamplitude	K	m s^{-1}	2.54 ± 0.90	<1.60
Derived quantities				
Orbital separation	a/R_*		11.6 ± 0.6	6.6 ± 0.3
Orbital semimajor axis	a	au	0.076 ± 0.002	0.0435 ± 0.0009
Radius	R_p	$R_\oplus$	2.62 ± 0.16	1.50 ± 0.12
Mass	M_p	$M_\oplus$	8.5 ± 3.1	<4.1
Bulk density	ρ	g cm^{-3}	2.6 ± 1.1	<7.1
Equilibrium temperature	$T_{\rm eq}$	K	1290 ± 41	1707 ± 54
Instellation flux	S_p	$S_\oplus$	461.4 ± 58.7	1413.5 ± 179.7
Transit duration	$T_{\rm dur}$	hr	3.23 ± 0.04	1.30 ± 0.05
TSM			112 ± 51	$\cdots$

Parameter	Symbol	Units	Value
Additional Parameters			
TESS photometric offset	$\mu_{\rm TESS}$	ppt	0.006 ± 0.005
TESS photometric jitter	$\sigma_{\rm TESS}$	ppt	0.122 ± 0.001
Keck-HIRES RV offset	$\gamma_{\rm HIRES}$	m s^{-1}	-1.97 ± 0.80
Keck-HIRES RV jitter	$\sigma_{\rm HIRES}$	m s^{-1}	7.31 ± 0.61
APF-Levy RV offset	$\gamma_{\rm APF}$	m s^{-1}	0.33 ± 0.88
APF-Levy RV jitter	$\sigma_{\rm APF}$	m s^{-1}	7.34 ± 0.80

Note. Table notes are the same as found at the bottom of Table 10. The upper limits on the RV semiamplitude, mass, and bulk density of planet c reflect 98% confidence. We choose not to report a TSM value for planet c because its mass is too unconstrained. Planet properties come from the joint model shown in Figure 15, which uses the iGrand reduction method to compute RVs from the APF-Levy spectra.

Table 13
TOI-669 System Parameters

Parameter	Symbol	Units	Value	Provenance
		Stellar Parameters		
Identifying information				
TOI ID			669	Guerrero
TIC ID			124573851	Guerrero
R.A.		deg (J2000)	158.90	Gaia DR3
Decl.		deg (J2000)	−5.18	Gaia DR3
Parallax	π	mas	7.01 ± 0.01	Gaia DR3
Johnson V-band apparent magnitude	V	mag	10.61 ± 0.01	TIC
J-band apparent magnitude	J	mag	9.56 ± 0.02	2MASS
K_s-band apparent magnitude	K_s	mag	9.13 ± 0.02	2MASS
Spectroscopy				
Effective temperature	T_{eff}	K	5600 ± 110	SpecMatch-Emp
Metallicity	[Fe/H]	dex	-0.06 ± 0.09	SpecMatch-Emp
Ca II H & K emission	$\log_{10} R'_{\text{HK}}$		-5.01 ± 0.05	Isaacson
Isochrone modeling				
Mass	M_*	$M_\odot$	0.90 ± 0.06	isoclassify
Radius	R_*	$R_\odot$	0.99 ± 0.04	isoclassify
Age		Gyr	8.6 ± 2.9	isoclassify
Transit modeling				
Limb-darkening parameter 1	u_1		0.88 ± 0.43	Joint model
Limb-darkening parameter 2	u_2		-0.18 ± 0.41	Joint model

Parameter	Symbol	Units	TOI-669 b value
		Planet Parameters	
Measured quantities			
Orbital period	P	day	3.94515 ± 0.00002
Time of inferior conjunction	T_c	BTJD	1913.041 ± 0.002
Occultation fraction	R_p/R_*		0.024 ± 0.001
Impact parameter	b		0.23 ± 0.18
Orbital eccentricity	e		<0.23
Argument of periastron	ω	deg	196.2 ± 64.3
RV semiamplitude	K	m s^{-1}	4.30 ± 0.62
Derived quantities			
Orbital separation	a/R_*		10.3 ± 0.5
Orbital semimajor axis	a	au	0.047 ± 0.001
Radius	R_p	$R_\oplus$	2.60 ± 0.17
Mass	M_p	$M_\oplus$	9.8 ± 1.5
Bulk density	ρ	g cm^{-3}	3.0 ± 0.7
Equilibrium temperature	T_{eq}	K	1235 ± 37
Instellation flux	S_p	$S_\oplus$	388.2 ± 47.1
Transit duration	T_{dur}	hr	2.9 ± 0.1
TSM			35 ± 8

Parameter	Symbol	Units	Value
		Additional Parameters	
TESS photometric offset	μ_{TESS}	ppt	0.02 ± 0.01
TESS photometric jitter	σ_{TESS}	ppt	0.02 ± 0.02
Keck-HIRES RV offset	γ_{HIRES}	m s^{-1}	-2.25 ± 0.43
Keck-HIRES RV jitter	σ_{HIRES}	m s^{-1}	2.88 ± 0.36

Note. Table notes are the same as found at the bottom of Table 10.

Table 14
HD 135694 System Parameters

Parameter	Symbol	Units	Value	Provenance
Stellar Parameters				
Identifying information				
TOI ID			1247	Guerrero
TIC ID			232540264	Guerrero
R.A.		deg (J2000)	227.87	Gaia DR3
Decl.		deg (J2000)	71.84	Gaia DR3
Parallax	π	mas	13.63 ± 0.01	Gaia DR3
Johnson *V*-band apparent magnitude	V	mag	9.08 ± 0.03	TIC
J-band apparent magnitude	J	mag	7.87 ± 0.02	2MASS
K_s-band apparent magnitude	K_s	mag	7.50 ± 0.02	2MASS
Spectroscopy				
Effective temperature	$T_{\rm eff}$	K	5710 ± 110	SpecMatch-Emp
Metallicity	[Fe/H]	dex	-0.21 ± 0.09	SpecMatch-Emp
Ca II H & K emission	$\log_{10} R'_{\rm HK}$		-4.99 ± 0.05	Isaacson
Isochrone modeling				
Mass	M_*	$M_\odot$	0.90 ± 0.06	isoclassify
Radius	R_*	$R_\odot$	1.05 ± 0.05	isoclassify
Age		Gyr	9.6 ± 2.4	isoclassify
Transit modeling				
Limb-darkening parameter 1	u_1		0.15 ± 0.16	Joint model
Limb-darkening parameter 2	u_2		0.51 ± 0.28	Joint model

Parameter	Symbol	Units	HD 135694 b value
Planet Parameters			
Measured quantities			
Orbital period	P	day	15.92346 ± 0.00002
Time of inferior conjunction	$T_{\rm c}$	BTJD	2324.5878 ± 0.0007
Occultation fraction	$R_{\rm p}/R_*$		0.0219 ± 0.0005
Impact parameter	b		0.37 ± 0.23
Orbital eccentricity	e		<0.42
Argument of periastron	ω	deg	82.5 ± 152.4
RV semiamplitude	K	m s^{-1}	1.60 ± 0.58
Derived quantities			
Orbital separation	a/R_*		24.5 ± 1.3
Orbital semimajor axis	a	au	0.120 ± 0.003
Radius	$R_{\rm p}$	$R_\oplus$	2.51 ± 0.14
Mass	$M_{\rm p}$	$M_\oplus$	5.7 ± 2.1
Bulk density	ρ	g cm^{-3}	2.0 ± 0.8
Equilibrium temperature	$T_{\rm eq}$	K	815 ± 27
Instellation flux	$S_{\rm p}$	$S_\oplus$	73.7 ± 9.9
Transit duration	$T_{\rm dur}$	hr	4.29 ± 0.05
TSM			69 ± 32

Parameter	Symbol	Units	Value
Additional Parameters			
TESS photometric offset	$\mu_{\rm TESS}$	ppt	0.012 ± 0.004
TESS photometric jitter	$\sigma_{\rm TESS}$	ppt	0.074 ± 0.005
Keck-HIRES RV offset	$\gamma_{\rm HIRES}$	m s^{-1}	0.03 ± 0.47
Keck-HIRES RV jitter	$\sigma_{\rm HIRES}$	m s^{-1}	3.78 ± 0.36
APF-Levy RV offset	$\gamma_{\rm APF}$	m s^{-1}	0.50 ± 0.71
APF-Levy RV jitter	$\sigma_{\rm APF}$	m s^{-1}	7.08 ± 0.54

Note. Table notes are the same as found at the bottom of Table 10.

Table 15
HIP 9618 System Parameters

			Stellar Parameters	
Parameter	Symbol	Units	Value	Provenance
Identifying information				
TOI ID			1471	Guerrero
TIC ID			306263608	Guerrero
R.A.		deg (J2000)	30.91	Gaia DR3
Decl.		deg (J2000)	21.28	Gaia DR3
Parallax	π	mas	14.86 ± 0.02	Gaia DR3
Johnson V-band apparent magnitude	V	mag	9.20 ± 0.03	TIC
J-band apparent magnitude	J	mag	7.92 ± 0.03	2MASS
K_s-band apparent magnitude	K_s	mag	7.56 ± 0.02	2MASS
Spectroscopy				
Effective temperature	$T_{\rm eff}$	K	5550 ± 110	SpecMatch-Emp
Metallicity	[Fe/H]	dex	-0.1 ± 0.09	SpecMatch-Emp
Ca II H & K emission	$\log_{10} R'_{\rm HK}$		-4.99 ± 0.05	Isaacson
Isochrone modeling				
Mass	M_*	$M_\odot$	0.93 ± 0.06	isoclassify
Radius	R_*	$R_\odot$	0.95 ± 0.03	isoclassify
Age		Gyr	5.2 ± 2.7	isoclassify
Transit modeling				
Limb-darkening parameter 1	u_1		0.37 ± 0.19	Joint model
Limb-darkening parameter 2	u_2		0.17 ± 0.31	Joint model

			Planet Parameters	
Parameter	Symbol	Units	HIP 9618 b value	HIP 9618 c value
Measured quantities				
Orbital period	P	day	20.77288 ± 0.00005	52.5636 ± 0.0002
Time of inferior conjunction	T_c	BTJD	2120.5612 ± 0.0008	2094.572 ± 0.001
Occultation fraction	$R_{\rm p}/R_*$		0.0364 ± 0.0005	0.0324 ± 0.0006
Impact parameter	b		0.17 ± 0.13	0.24 ± 0.14
Orbital eccentricity	e		<0.13	<0.12
Argument of periastron	ω	deg	206.6 ± 147.8	165.6 ± 130.8
RV semiamplitude	K	m s^{-1}	2.06 ± 0.48	<1.41
Derived quantities				
Orbital separation	a/R_*		32.9 ± 0.9	61.0 ± 1.7
Orbital semimajor axis	a	au	0.144 ± 0.003	0.268 ± 0.006
Radius	$R_{\rm p}$	$R_\oplus$	3.75 ± 0.13	3.34 ± 0.13
Mass	$M_{\rm p}$	$M_\oplus$	8.4 ± 2.0	<7.9
Bulk density	ρ	g cm^{-3}	0.9 ± 0.2	<1.2
Equilibrium temperature	$T_{\rm eq}$	K	685 ± 17	503 ± 13
Instellation flux	$S_{\rm p}$	$S_\oplus$	36.8 ± 3.7	10.7 ± 1.1
Transit duration	$T_{\rm dur}$	hr	4.74 ± 0.05	6.34 ± 0.06
TSM			161 ± 43	>87

			Additional Parameters
Parameter	Symbol	Units	Value
TESS photometric offset	$\mu_{\rm TESS}$	ppt	0.022 ± 0.009
TESS photometric jitter	$\sigma_{\rm TESS}$	ppt	0.148 ± 0.006
Keck-HIRES RV offset	$\gamma_{\rm HIRES}$	m s^{-1}	0.57 ± 0.48
Keck-HIRES RV jitter	$\sigma_{\rm HIRES}$	m s^{-1}	3.34 ± 0.42
APF-Levy RV offset	$\gamma_{\rm APF}$	m s^{-1}	11.34 ± 0.52
APF-Levy RV jitter	$\sigma_{\rm APF}$	m s^{-1}	4.81 ± 0.38
Linear RV trend	$\dot{\gamma}$	m s^{-1} day^{-1}	-0.059 ± 0.001

Note. Table notes are the same as found at the bottom of Table 10. All limits reflect 98% confidence.

Table 16
HD 6061 System Parameters

		Stellar Parameters		
Parameter	Symbol	Units	Value	Provenance
Identifying information				
TOI ID			1473	Guerrero
TIC ID			352413427	Guerrero
R.A.		deg (J2000)	15.60	Gaia DR3
Decl.		deg (J2000)	37.19	Gaia DR3
Parallax	π	mas	14.77 ± 0.02	Gaia DR3
Johnson *V*-band apparent magnitude	V	mag	8.84 ± 0.01	TIC
J-band apparent magnitude	J	mag	7.72 ± 0.03	AO
K_s-band apparent magnitude	K_s	mag	7.41 ± 0.02	AO
Spectroscopy				
Effective temperature	$T_{\rm eff}$	K	5920 ± 110	SpecMatch-Emp
Metallicity	[Fe/H]	dex	-0.08 ± 0.09	SpecMatch-Emp
Ca II H & K emission	$\log_{10} R'_{\rm HK}$		-4.76 ± 0.05	Isaacson
Isochrone modeling				
Mass	M_*	$M_\odot$	1.00 ± 0.06	isoclassify
Radius	R_*	$R_\odot$	1.03 ± 0.03	isoclassify
Age		Gyr	2.4 ± 1.7	isoclassify
Transit modeling				
Limb-darkening parameter 1	u_1		0.28 ± 0.24	Joint model
Limb-darkening parameter 2	u_2		0.35 ± 0.36	Joint model
		Planet Parameters		
Parameter	Symbol	Units	HD 6061 b value	
Measured quantities				
Orbital period	P	day	5.254467 ± 0.000009	
Time of inferior conjunction	T_c	BTJD	2321.505 ± 0.001	
Occultation fraction	R_p/R_*		0.0218 ± 0.0006	
Impact parameter	b		0.14 ± 0.12	
Orbital eccentricity	e		$\equiv 0$	
Argument of periastron	ω	deg	$\cdots$	
RV semiamplitude	K	m s^{-1}	4.00 ± 0.99	
Derived quantities				
Orbital separation	a/R_*		12.3 ± 0.3	
Orbital semimajor axis	a	au	0.059 ± 0.001	
Radius	R_p	$R_\oplus$	2.45 ± 0.09	
Mass	M_p	$M_\oplus$	10.8 ± 2.7	
Bulk density	ρ	g cm^{-3}	4.0 ± 1.1	
Equilibrium temperature	$T_{\rm eq}$	K	1194 ± 28	
Instellation flux	S_p	$S_\oplus$	339.1 ± 31.9	
Transit duration	$T_{\rm dur}$	hr	3.21 ± 0.06	
TSM			55 ± 16	
		Additional Parameters		
Parameter	Symbol	Units	Value	
TESS photometric offset	$\mu_{\rm TESS}$	ppt	0.03 ± 0.05	
TESS photometric jitter	$\sigma_{\rm TESS}$	ppt	0.150 ± 0.005	
Keck-HIRES RV offset	$\gamma_{\rm HIRES}$	m s^{-1}	-2.57 ± 1.02	
Keck-HIRES RV jitter	$\sigma_{\rm HIRES}$	m s^{-1}	2.17 ± 2.01	
APF-Levy RV offset	$\gamma_{\rm APF}$	m s^{-1}	0.58 ± 1.79	
APF-Levy RV jitter	$\sigma_{\rm APF}$	m s^{-1}	2.80 ± 3.96	

Note. Table notes are the same as found at the bottom of Table 10. For HD 6061 's *J* and K_s apparent magnitudes, the "AO" provenance denotes that these values have been deblended using our AO imaging observations to account for the M4/5V companion, TIC 600433892.

Table 17
TOI-1736 System Parameters

		Stellar Parameters		
Parameter	Symbol	Units	Value	Provenance
Identifying information				
TOI ID			1736	Guerrero
TIC ID			408618999	Guerrero
R.A.		deg (J2000)	43.43	Gaia DR3
Decl.		deg (J2000)	69.10	Gaia DR3
Parallax	π	mas	11.34 ± 0.02	Gaia DR3
Johnson V-band apparent magnitude	V	mag	8.953 ± 0.002	TIC
J-band apparent magnitude	J	mag	7.69 ± 0.02	2MASS
K_s-band apparent magnitude	K_s	mag	7.28 ± 0.02	2MASS
Spectroscopy				
Effective temperature	$T_{\rm eff}$	K	5670 ± 110	SpecMatch-Emp
Metallicity	[Fe/H]	dex	0.13 ± 0.09	SpecMatch-Emp
Ca II H & K emission	$\log_{10} R'_{\rm HK}$		-5.02 ± 0.05	Isaacson
Isochrone modeling				
Mass	M_*	$M_\odot$	1.06 ± 0.08	isoclassify
Radius	R_*	$R_\odot$	1.38 ± 0.07	isoclassify
Age		Gyr	8.6 ± 1.7	isoclassify
Transit modeling				
Limb-darkening parameter 1	u_1		0.19 ± 0.19	Joint model
Limb-darkening parameter 2	u_2		0.26 ± 0.27	Joint model

		Planet Parameters		
Parameter	Symbol	Units	TOI-1736 b value	TOI-1736 c value
Measured quantities				
Orbital period	P	day	7.073091 ± 0.000008	571.3 ± 0.5
Time of inferior conjunction	T_c	BTJD	2740.5891 ± 0.0007	2273.1 ± 0.4
Occultation fraction	R_p/R_*		0.0202 ± 0.0004	⋯
Impact parameter	b		0.53 ± 0.11	⋯
Orbital eccentricity	e		<0.16	0.369 ± 0.002
Argument of periastron	ω	deg	136.4 ± 94.5	162.1 ± 0.5
RV semiamplitude	K	m s^{-1}	3.82 ± 0.49	197.6 ± 0.6
Derived quantities				
Orbital separation	a/R_*		11.4 ± 0.6	213.4 ± 12.1
Orbital semimajor axis	a	au	0.074 ± 0.002	1.37 ± 0.03
Radius	R_p	$R_\oplus$	3.05 ± 0.19	⋯
Minimum mass	$M_p \sin i$	$M_\oplus$	11.9 ± 1.6	2477 ± 118
Minimum mass	$M_p \sin i$	$M_{\rm Jup}$	0.037 ± 0.005	7.8 ± 0.4
Mass	M_p	$M_\oplus$	11.9 ± 1.6	⋯
Bulk density	ρ	g cm^{-3}	2.3 ± 0.5	⋯
Equilibrium temperature	$T_{\rm eq}$	K	1186 ± 41	274 ± 10
Instellation flux	S_p	$S_\oplus$	329.6 ± 46.0	0.9 ± 0.1
Transit duration	$T_{\rm dur}$	hr	3.94 ± 0.04	⋯
TSM			55 ± 11	⋯

		Additional Parameters	
Parameter	Symbol	Units	Value
TESS photometric offset	$\mu_{\rm TESS}$	ppt	0.012 ± 0.006
TESS photometric jitter	$\sigma_{\rm TESS}$	ppt	0.117 ± 0.004
Keck-HIRES RV offset	$\gamma_{\rm HIRES}$	m s^{-1}	19.99 ± 0.59
Keck-HIRES RV jitter	$\sigma_{\rm HIRES}$	m s^{-1}	4.34 ± 0.45
APF-Levy RV offset	$\gamma_{\rm APF}$	m s^{-1}	23.59 ± 0.80
APF-Levy RV jitter	$\sigma_{\rm APF}$	m s^{-1}	6.15 ± 0.32
Linear RV trend	$\dot{\gamma}$	m s^{-1} day^{-1}	-0.183 ± 0.002

Note. Table notes are the same as found at the bottom of Table 10.
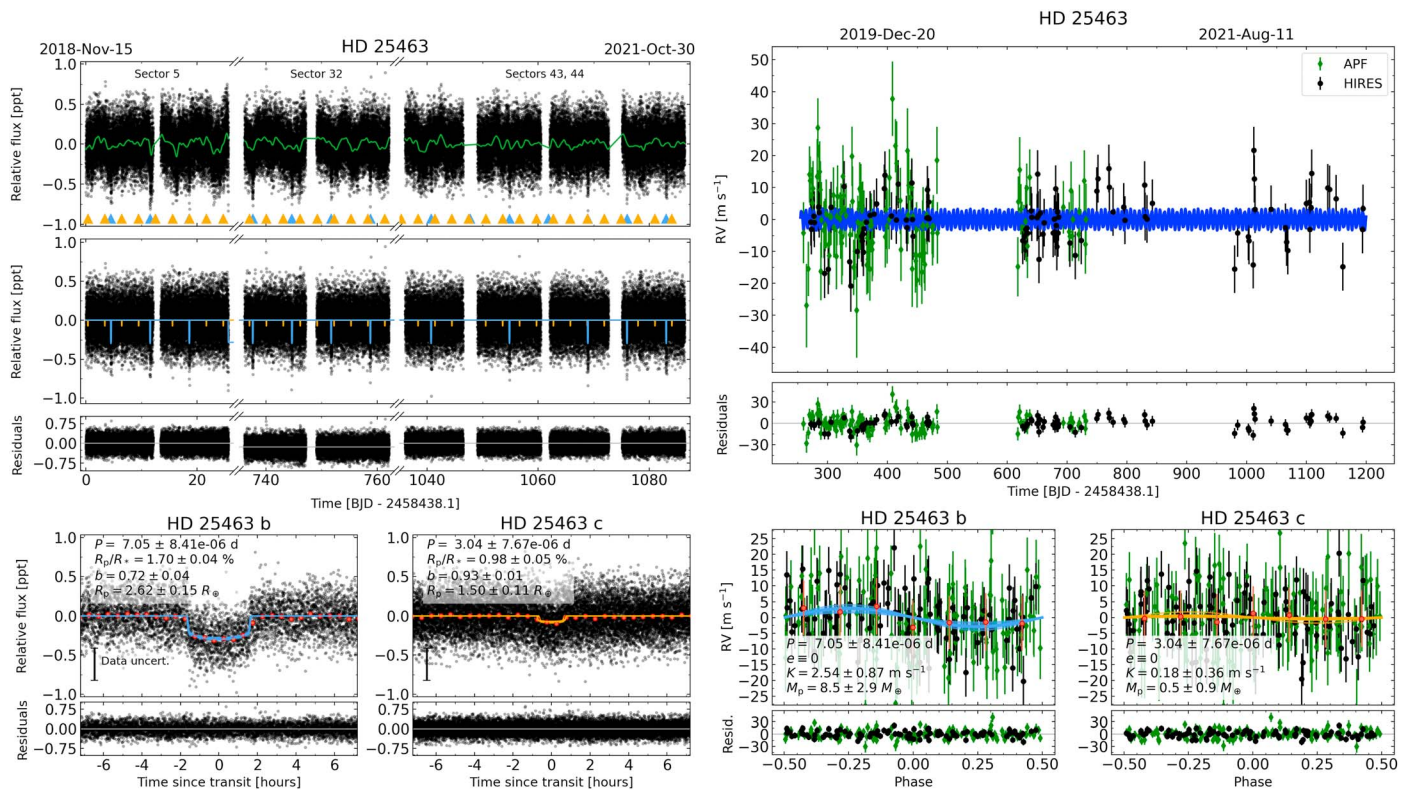
Figure 15. Our joint modeling results for HD 25463. The figure description is the same as for Figure 6.
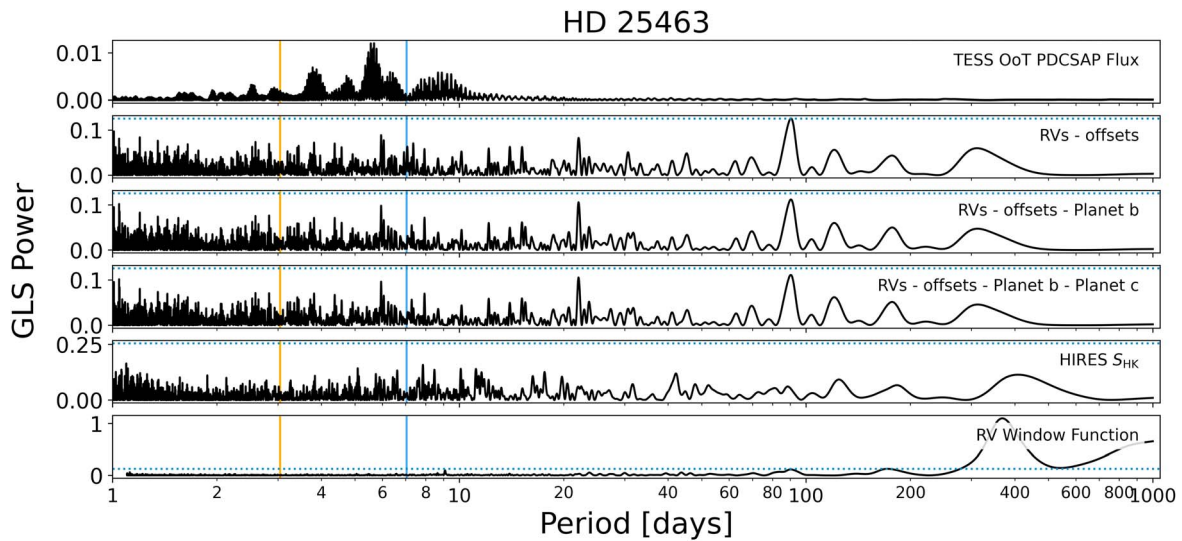

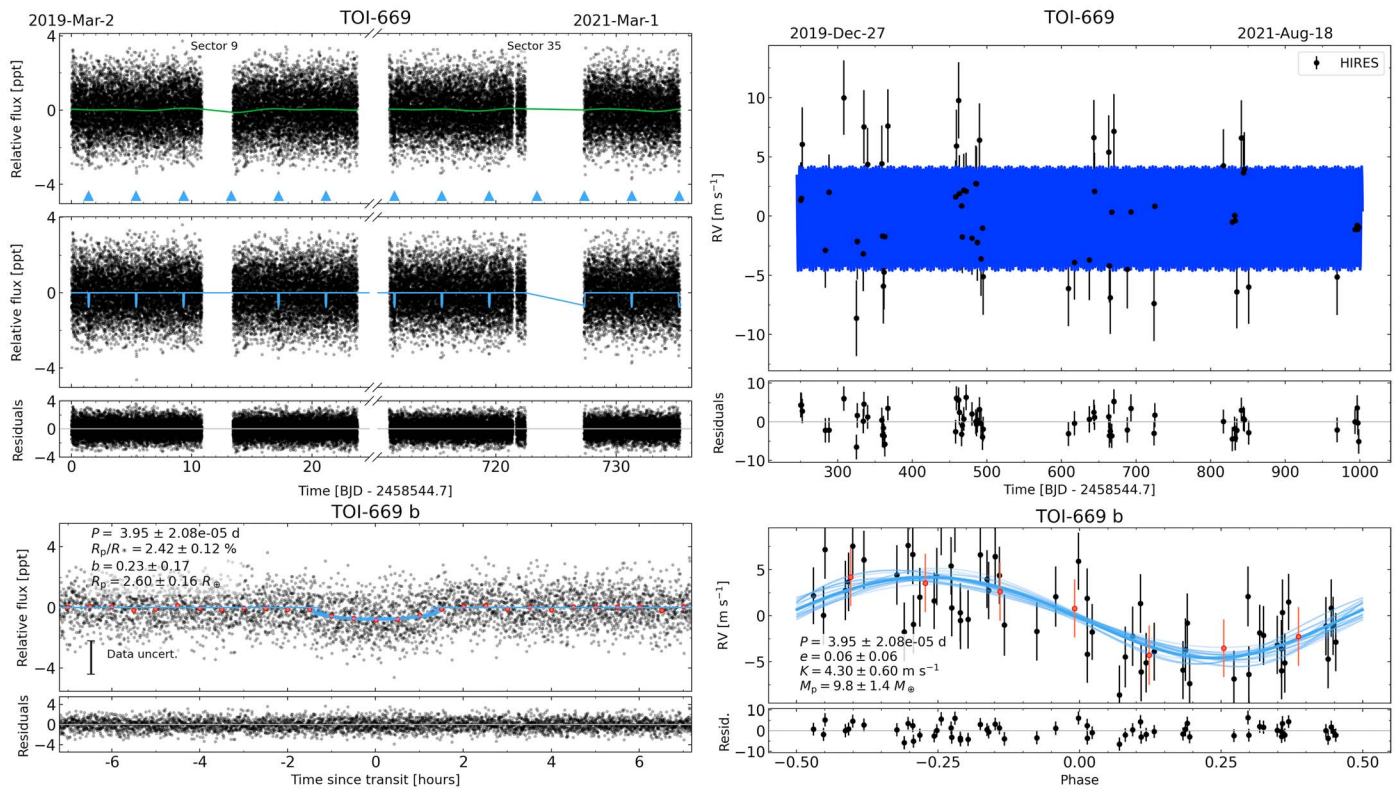**Figure 16.** GLS periodograms for HD 25463. The figure description is the same as for Figure 7.

Figure 17. Our joint modeling results for TOI-669. The figure description is the same as for Figure 6.
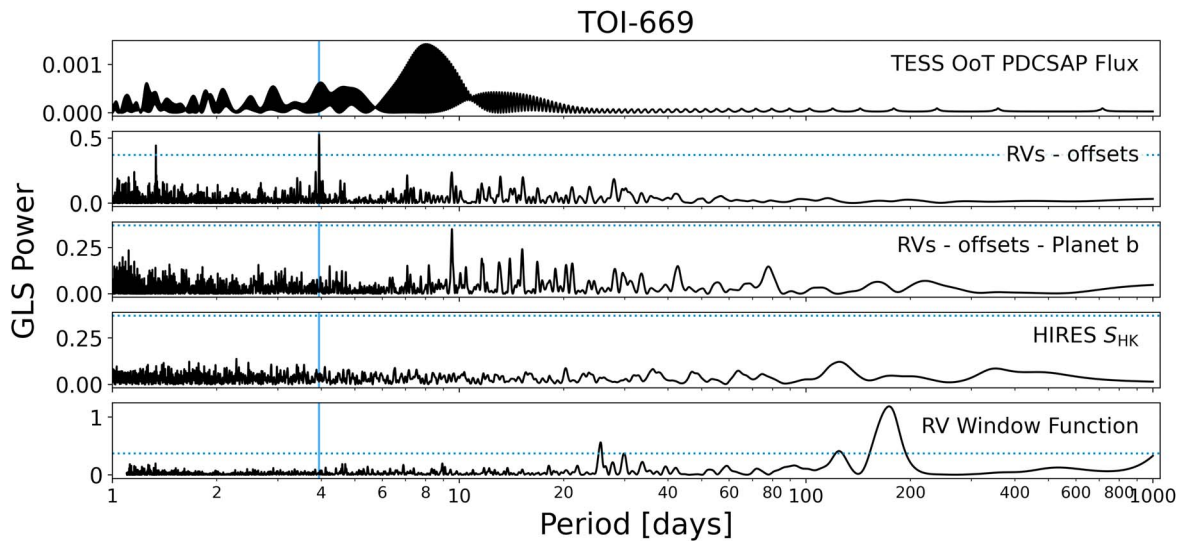

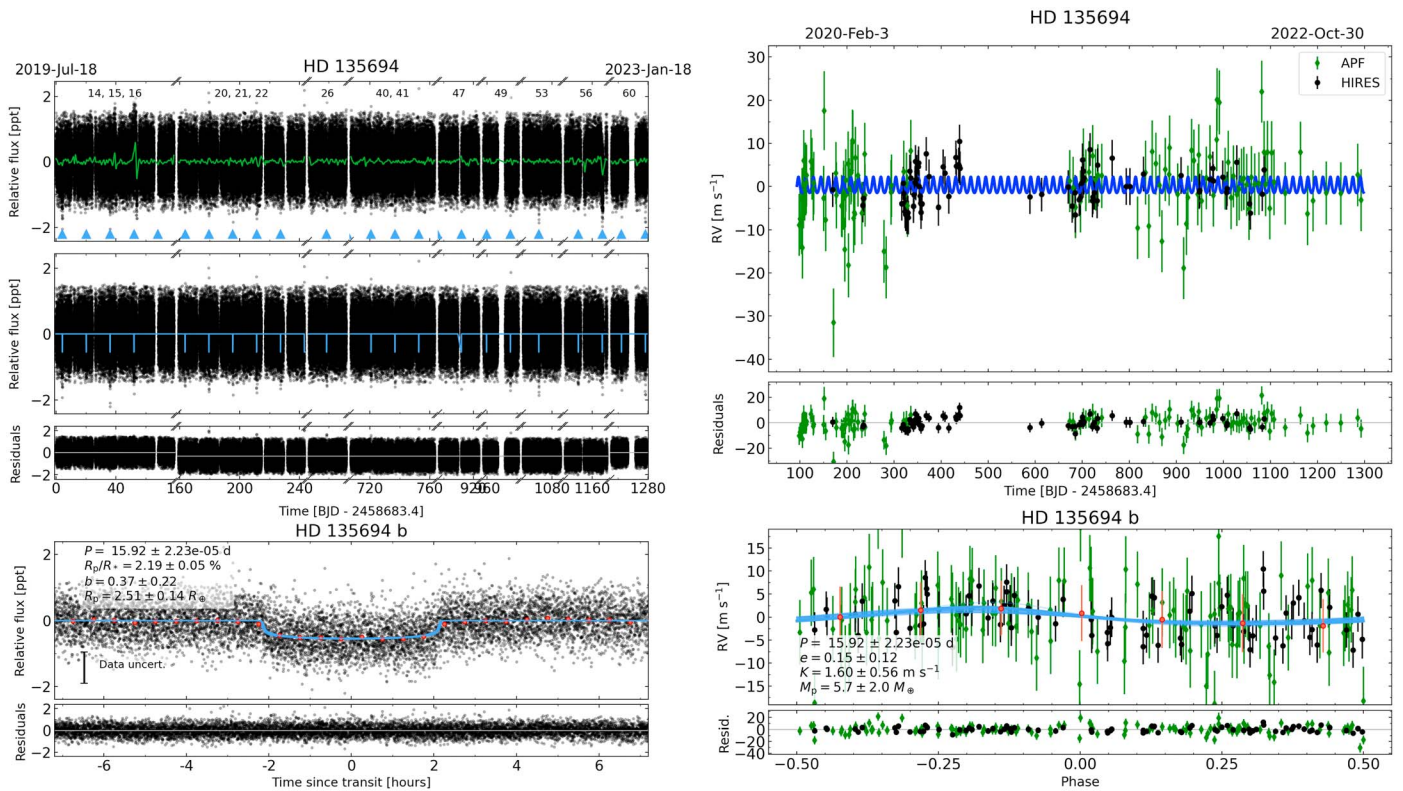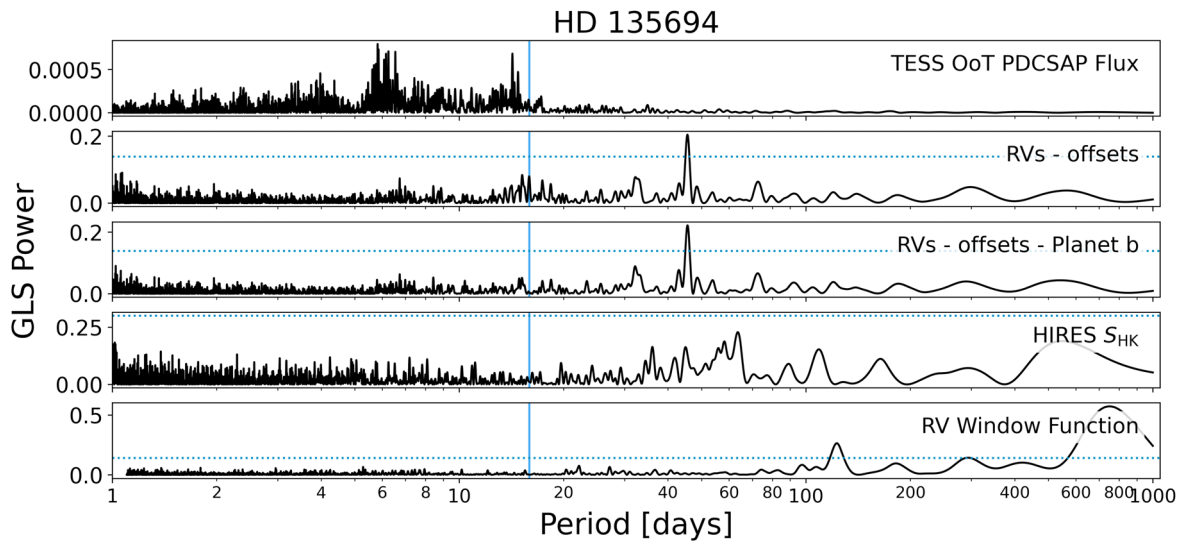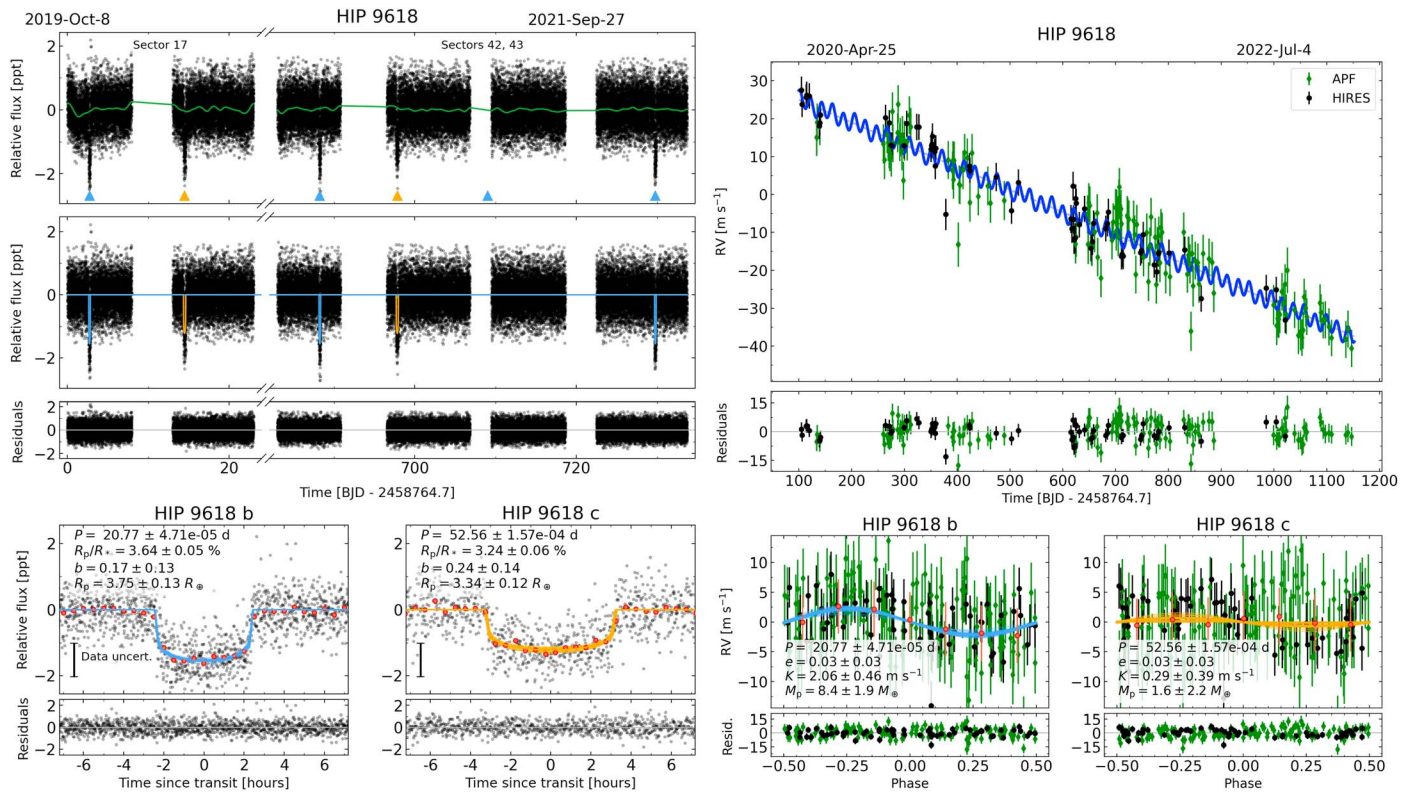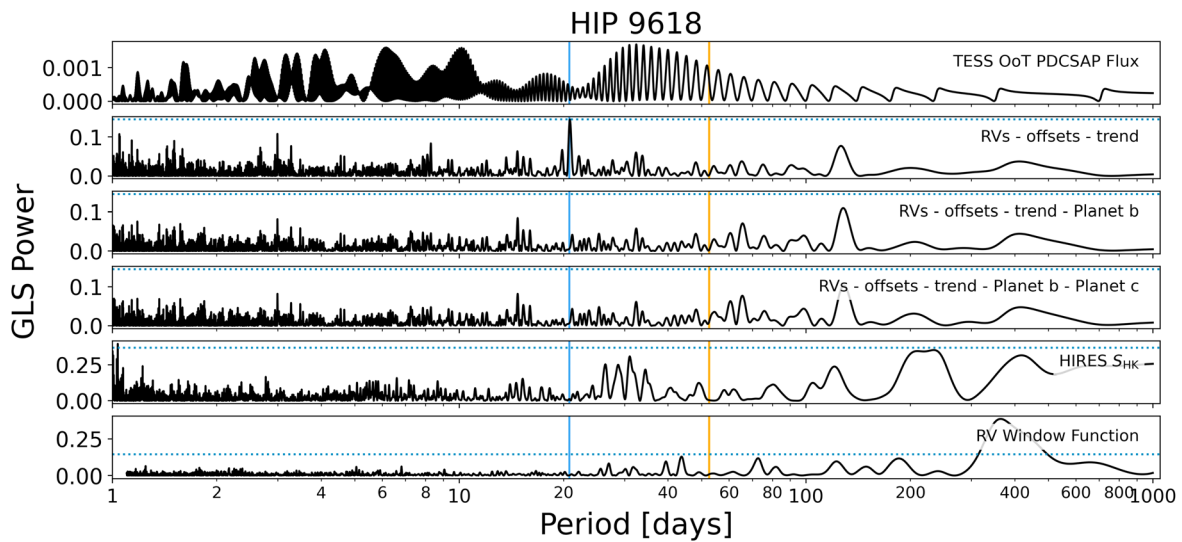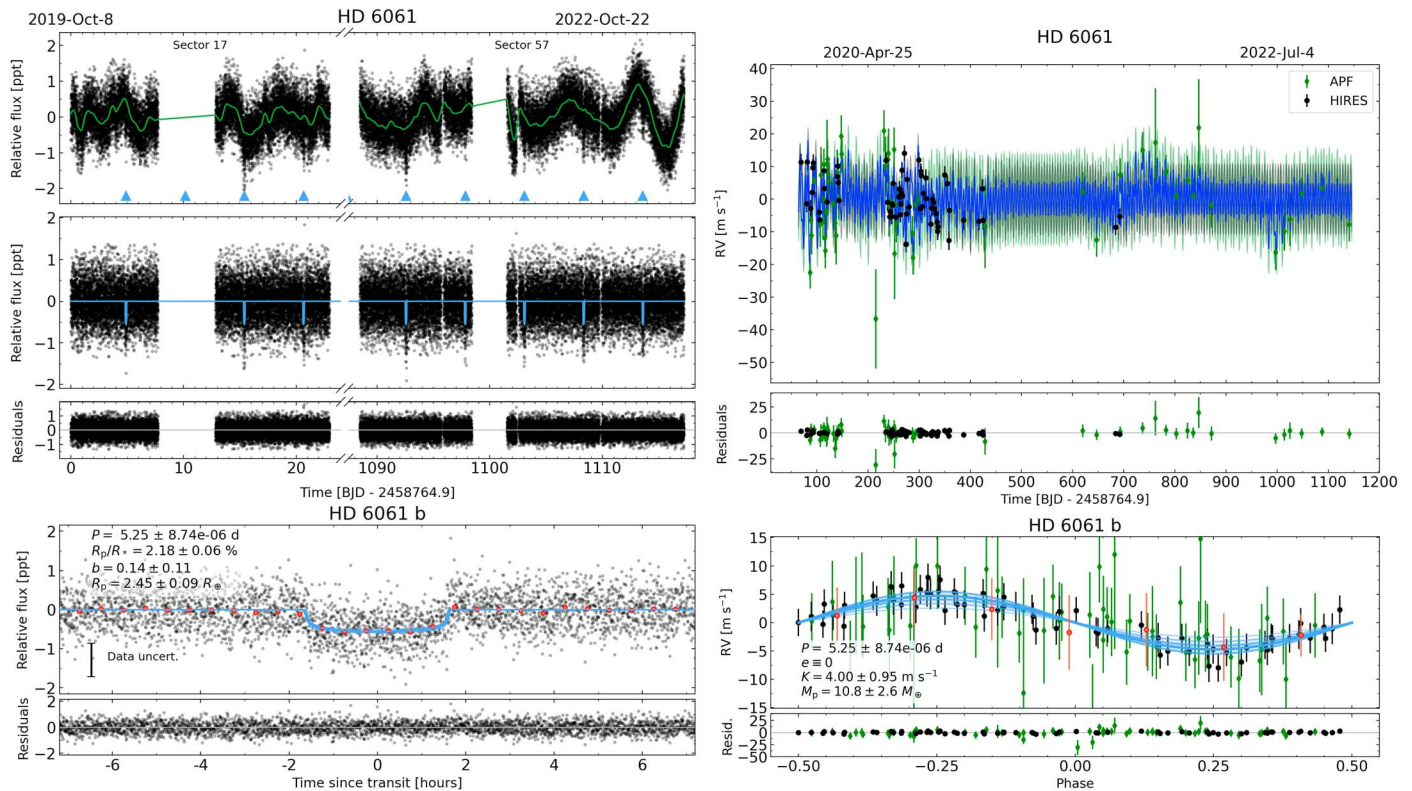**Figure 18.** GLS periodograms for TOI-669. The figure description is the same as for Figure 7.

Figure 19. Our joint modeling results for HD 135694. The figure description is the same as for Figure 6.

Figure 20. GLS periodograms for HD 135694. The figure description is the same as for Figure 7.

Figure 21. Our joint modeling results for HIP 9618. The figure description is the same as for Figure 6.

Figure 22. GLS periodograms for HIP 9618. The figure description is the same as for Figure 7.

Figure 23. Our joint modeling results for HD 6061. The figure description is the same as for Figure 6, save for the RV model (right), which also shows the GP model of stellar activity. The combined Keplerian plus GP predictions for Keck-HIRES and APF-Levy are shown in blue, with 1σ error envelopes in gray and green, respectively.
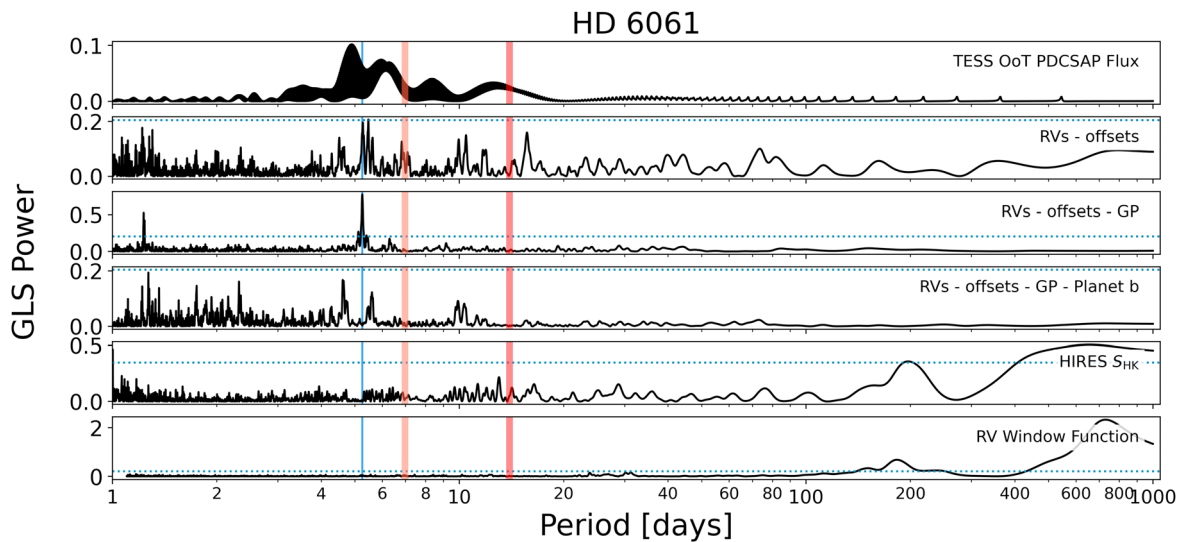
Figure 24. GLS periodograms for HD 6061. The figure description is the same as for Figure 7. The period of the GP used to model stellar activity in the RVs is marked with the red vertical line, and its first harmonic is marked with the light-red line.
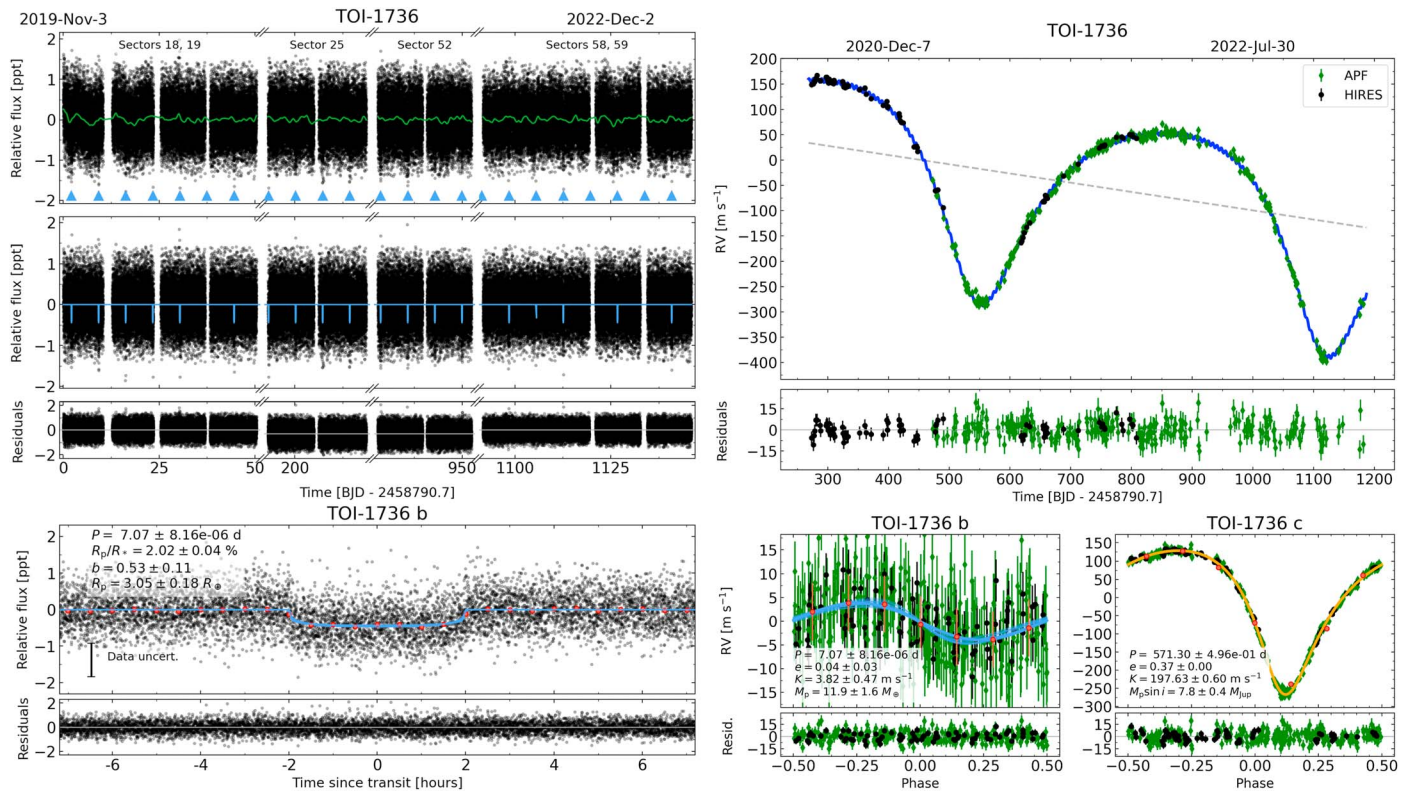
Figure 25. Our joint modeling results for TOI-1736. The figure description is the same as for Figure 6. The dashed gray line in the top panel of the RV figure represents the linear RV trend detected in the system.
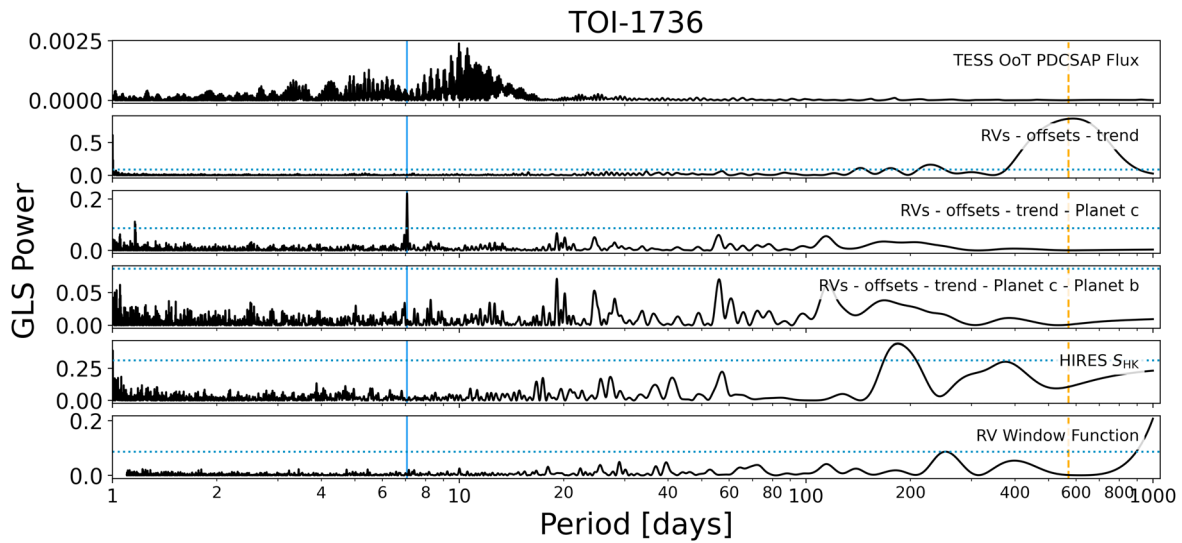
Figure 26. GLS periodograms for TOI-1736. The figure description is the same as for Figure 7. The dashed vertical line for planet c indicates that it is nontransiting.

Appendix B
Default HD 25463 APF-Levy Radial Velocity Measurements

As described in Section 5.2.2, the default Doppler reduction pipeline (Howard et al. 2010) fails when computing APF-Levy RVs for HD 25463, in part due to the star's rapid rotation ($v \sin i_* = 11.6 \pm 1.0$ km s^{-1}). To circumvent this failure, we slightly alter the default reduction method to fit entire echelle orders of the APF-Levy spectra simultaneously, rather than in series using small chunks. In Figure 27 we compare the default reduction method's RVs with those from the alternative pipeline (iGrand) and the system's Keck-HIRES RVs. In addition to containing the iGrand-derived APF-Levy velocities for HD 25463, Table 5 also holds RVs for the system that were derived following the default reduction method (in that table, the RVs are found under the label "HD 25463 Default"). We do not suggest using these velocities in future analyses for the reasons described in Section 5.2, and they are only included for completeness. Figure 28 shows the RV portion of a joint model that is entirely similar to our adopted model for HD 25463 (Figure 15), except the default APF-Levy RVs are used.
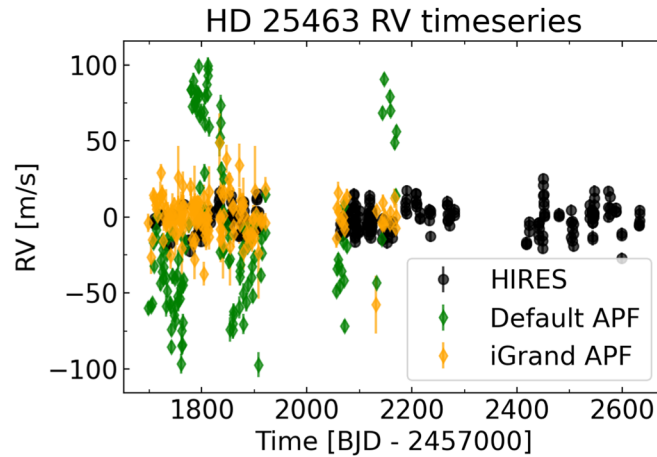

Figure 27. The HD 25463 RVs. Keck-HIRES RVs are shown as the black circles, the default pipeline's APF-Levy RVs are shown as the green diamonds, and the iGrand pipeline's APF-Levy RVs are shown as the orange diamonds. The default APF-Levy RVs show scatter that is seemingly inconsistent with the astrophysical jitter when compared to contemporaneous Keck-HIRES RVs. The iGrand reduction method seems to mitigate these systematics.
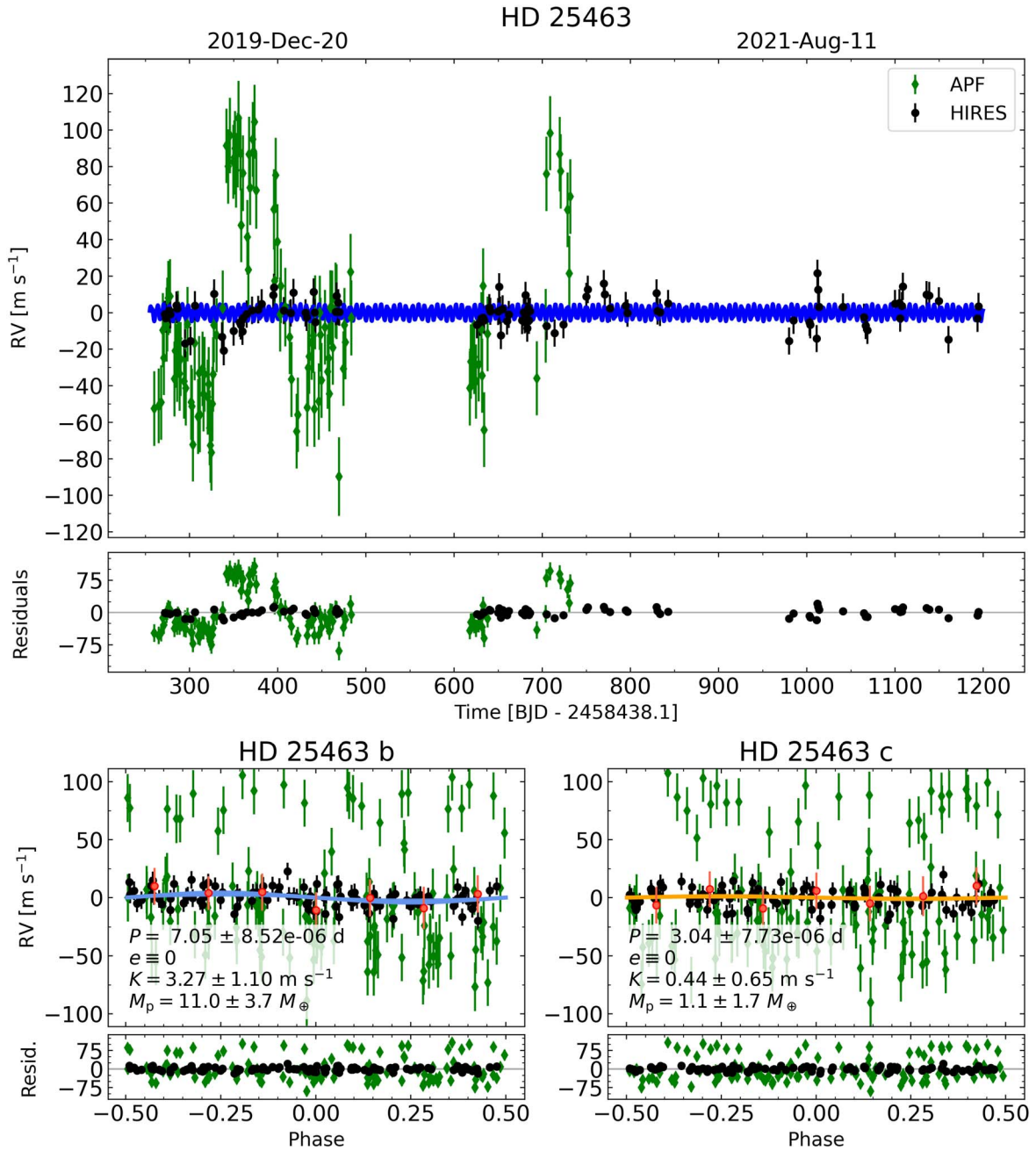
Figure 28. The RV portion of a joint model of the HD 25463 TESS photometry and RVs where the APF-Levy RVs are measured using the default Doppler pipeline (Howard et al. 2010) as opposed to the `iGrand` reduction pipeline. This figure is only included for comparison with Figure 15 and the planet properties listed in the phase-folded panels should not be used. The figure description is the same as for Figure 6. The default APF-Levy RVs show unreasonably large scatter, which is a possible symptom of the star's rapid rotation. Mass estimates for planets b and c are consistent with the results of our adopted model, which uses the `iGrand` APF-Levy velocities (Figure 15). The results of the photometry portion of this joint model (not shown here for brevity) are entirely consistent with those of the model shown on the left in Figure 15—because both the model here and in Figure 15 assume circular orbits for the planets, there is minimal information sharing between the photometry and RV components (for circular orbits, only the planet's orbital period and time of inferior conjunction, both of which are largely determined by the transits, are shared between the photometry and RV models). As such, we would expect the photometric model results to be essentially the same regardless of which APF-Levy velocities are used. Since they are not listed in an associated table of properties, for use in conjunction with the "HD 25463 Default" RVs in Table 5, the instrumental offsets and jitter terms for this model are: $\gamma_{\mathrm{APF}} = -7.56 \pm 1.95$ m s^{-1}, $\gamma_{\mathrm{HIRES}} = -1.99 \pm 0.81$ m s^{-1}, $\sigma_{\mathrm{APF}} = 19.97 \pm 0.03$ m s^{-1} (which would be larger if not for the joint model's prior on instrumental RV jitter that enforces a maximum of 20 m s^{-1}), and $\sigma_{\mathrm{HIRES}} = 7.31 \pm 0.61$ m s^{-1}.

ORCID iDs

Joseph M. Akana Murphy ⓘ https://orcid.org/0000-0001-8898-8284
Natalie M. Batalha ⓘ https://orcid.org/0000-0002-7030-9519
Nicholas Scarsdale ⓘ https://orcid.org/0000-0003-3623-7280
Howard Isaacson ⓘ https://orcid.org/0000-0002-0531-1073
David R. Ciardi ⓘ https://orcid.org/0000-0002-5741-3047

Erica J. Gonzales ⓘ https://orcid.org/0000-0002-9329-2190
Steven Giacalone ⓘ https://orcid.org/0000-0002-8965-3969
Joseph D. Twicken ⓘ https://orcid.org/0000-0002-6778-7552
Anne Dattilo ⓘ https://orcid.org/0000-0002-1092-2995
Tara Fetherolf ⓘ https://orcid.org/0000-0002-3551-279X
Ryan A. Rubenzahl ⓘ https://orcid.org/0000-0003-3856-3143
Courtney D. Dressing ⓘ https://orcid.org/0000-0001-8189-0233

Benjamin Fulton https://orcid.org/0000-0003-3504-5316
Andrew W. Howard https://orcid.org/0000-0001-8638-0320
Daniel Huber https://orcid.org/0000-0001-8832-4488
Stephen R. Kane https://orcid.org/0000-0002-7084-0529
Erik A. Petigura https://orcid.org/0000-0003-0967-2893
Paul Robertson https://orcid.org/0000-0003-0149-9678
Arpita Roy https://orcid.org/0000-0001-8127-5775
Lauren M. Weiss https://orcid.org/0000-0002-3725-3058
Corey Beard https://orcid.org/0000-0001-7708-2364
Ashley Chontos https://orcid.org/0000-0003-1125-2564
Fei Dai https://orcid.org/0000-0002-8958-0683
Malena Rice https://orcid.org/0000-0002-7670-670X
Judah Van Zandt https://orcid.org/0000-0002-4290-6826
Jack Lubin https://orcid.org/0000-0001-8342-7736
Sarah Blunt https://orcid.org/0000-0002-3199-2888
Alex S. Polanski https://orcid.org/0000-0001-7047-8681
Aida Behmard https://orcid.org/0000-0003-0012-9093
Paul A. Dalba https://orcid.org/0000-0002-4297-5506
Michelle L. Hill https://orcid.org/0000-0002-0139-4756
Lee J. Rosenthal https://orcid.org/0000-0001-8391-5182
Casey L. Brinkman https://orcid.org/0000-0002-4480-310X
Andrew W. Mayo https://orcid.org/0000-0002-7216-2135
Emma V. Turtelboom https://orcid.org/0000-0002-1845-2617
Isabel Angelo https://orcid.org/0000-0002-9751-2664
Teo Močnik https://orcid.org/0000-0003-4603-556X
Mason G. MacDougall https://orcid.org/0000-0003-2562-9043
Daria Pidhorodetska https://orcid.org/0000-0001-9771-7953
Dakotah Tyler https://orcid.org/0000-0003-0298-4667
Molly R. Kosiarek https://orcid.org/0000-0002-6115-4359
Rae Holcomb https://orcid.org/0000-0002-5034-9476
Emma M. Louden https://orcid.org/0000-0003-3179-5320
Lea A. Hirsch https://orcid.org/0000-0001-8058-7443
Emily A. Gilbert https://orcid.org/0000-0002-0388-8004
Jay Anderson https://orcid.org/0000-0003-2861-3995
Jeff A. Valenti https://orcid.org/0000-0003-3305-6281

References

Aceituno, J., Sánchez, S. F., Grupp, F., et al. 2013, A&A, 552, A31
Adams, E. R., Seager, S., & Elkins-Tanton, L. 2008, ApJ, 673, 1160
Aguichine, A., Mousis, O., Deleuil, M., & Marcq, E. 2021, ApJ, 914, 84
Aigrain, S., Pont, F., & Zucker, S. 2012, MNRAS, 419, 3147
Akaike, H. 1974, ITAC, 19, 716
Akana Murphy, J. M. 2023, tessla: Joint modeling of TESS photometry and radial velocities, v1.0, Zenodo, doi:10.5281/zenodo.7783386
Astropy Collaboration, Price-Whelan, A. M., Sipőcz, B. M., et al. 2018, AJ, 156, 123
Astropy Collaboration, Robitaille, T. P., Tollerud, E. J., et al. 2013, A&A, 558, A33
Badenas-Agusti, M., Günther, M. N., Daylan, T., et al. 2020, AJ, 160, 113
Baluev, R. V. 2008, MNRAS, 385, 1279
Batalha, N. E., Lewis, T., Fortney, J. J., et al. 2019, ApJL, 885, L25
Batalha, N. E., Wolfgang, A., Teske, J., et al. 2023, AJ, 165, 14
Batalha, N. M., Rowe, J. F., Bryson, S. T., et al. 2013, ApJS, 204, 24
Benz, W., Broeg, C., Fortier, A., et al. 2021, ExA, 51, 109
Berger, T. A., Huber, D., van Saders, J. L., et al. 2020, AJ, 159, 280
Betancourt, M. J., & Girolami, M. 2013, arXiv:1312.0906
Blunt, S., Carvalho, A., David, T. J., et al. 2023, AJ, 166, 62
Borucki, W. J., Koch, D., Basri, G., et al. 2010, Sci, 327, 977
Borucki, W. J., Koch, D. G., Batalha, N., et al. 2012, ApJ, 745, 120
Brandt, T. D., Dupuy, T. J., Li, Y., et al. 2021, AJ, 162, 186
Bryan, M. L., Knutson, H. A., Lee, E. J., et al. 2019, AJ, 157, 52
Bryson, S., Kunimoto, M., Kopparapu, R. K., et al. 2021, AJ, 161, 36

Burnham, K. P., & Anderson, D. R. 2004, Sociol. Methods Res., 33, 261
Butler, R. P., Marcy, G. W., Williams, E., et al. 1996, PASP, 108, 500
Cannon, A. J., & Pickering, E. C. 1993, yCat, 3135, 0
Chen, J., & Kipping, D. 2017, ApJ, 834, 17
Choi, J., Dotter, A., Conroy, C., et al. 2016, ApJ, 823, 102
Chontos, A., Murphy, J. M. A., MacDougall, M. G., et al. 2022, AJ, 163, 297
Ciardi, D. R., Crossfield, I. J. M., Feinstein, A. D., et al. 2018, AJ, 155, 10
Colquhoun, D. 2014, RSOS, 1, 140216
Cosentino, R., Lovis, C., Pepe, F., et al. 2012, Proc. SPIE, 8446, 84461V
Dai, F., Roy, A., Fulton, B., et al. 2020, AJ, 160, 193
Dalba, P. A., Kane, S. R., Dragomir, D., et al. 2022, AJ, 163, 61
Dekany, R., Roberts, J., Burruss, R., et al. 2013, ApJ, 776, 130
Dressing, C. D., & Charbonneau, D. 2013, ApJ, 767, 95
Drimmel, R., Cabrera-Lavers, A., & López-Corredoira, M. 2003, A&A, 409, 205
Duane, S., Kennedy, A. D., Pendleton, B. J., & Roweth, D. 1987, PhLB, 195, 216
Eastman, J., Siverd, R., & Gaudi, B. S. 2010, PASP, 122, 935
Fetherolf, T., Pepper, J., Simpson, E., et al. 2023, ApJS, 268, 4
Foreman-Mackey, D. 2018, RNAAS, 2, 31
Foreman-Mackey, D., Hogg, D. W., Lang, D., & Goodman, J. 2013, PASP, 125, 306
Foreman-Mackey, D., Luger, R., Czekala, I., et al. 2020, exoplanet-dev/exoplanet, v0.3.2, Zenodo, doi:10.5281/zenodo.1998447
Fressin, F., Torres, G., Charbonneau, D., et al. 2013, ApJ, 766, 81
Fulton, B. J., Petigura, E. A., Blunt, S., & Sinukoff, E. 2018, PASP, 130, 044504
Fulton, B. J., Petigura, E. A., Howard, A. W., et al. 2017, AJ, 154, 109
Furlan, E., Ciardi, D. R., Everett, M. E., et al. 2017, AJ, 153, 71
Gaia Collaboration, Brown, A. G. A., Vallenari, A., et al. 2018, A&A, 616, A1
Gaia Collaboration, Vallenari, A., Brown, A. G. A., et al. 2023, A&A, 674, A1
Gao, P., Wakeford, H. R., Moran, S. E., & Parmentier, V. 2021, JGRE, 126, e06655
Gelman, A., & Rubin, D. B. 1992, StaSc, 7, 457
Giacalone, S., Dressing, C. D., Jensen, E. L. N., et al. 2021, AJ, 161, 24
Goodman, J., & Weare, J. 2010, CAMCS, 5, 65
Green, G. M., Schlafly, E., Zucker, C., Speagle, J. S., & Finkbeiner, D. 2019, ApJ, 887, 93
Grimm, R. E., & McSween, H. Y. 1993, Sci, 259, 653
Grunblatt, S. K., Howard, A. W., & Haywood, R. D. 2015, ApJ, 808, 127
Guerrero, N. M., Seager, S., Huang, C. X., et al. 2021, ApJS, 254, 39
Hadden, S., & Lithwick, Y. 2017, AJ, 154, 5
Harris, C. R., Millman, K. J., van der Walt, S. J., et al. 2020, Natur, 585, 357
Harvey, J. 1985, in ESA SP-235, Future Missions in Solar, Heliospheric & Space Plasma Physics, ed. E. Rolfe & B. Battrick (Noordwijk: ESA), 199
Hastings, W. K. 1970, Biometrika, 57, 97
Hayward, T. L., Brandl, B., Pirger, B., et al. 2001, PASP, 113, 105
Haywood, R. D., Collier Cameron, A., Queloz, D., et al. 2014, MNRAS, 443, 2517
Haywood, R. D., Vanderburg, A., Mortier, A., et al. 2018, AJ, 155, 203
Hoffman, M., & Gelman, A. 2014, JMLR, 15, 1593, http://jmlr.org/papers/v15/hoffman14a.html
Houk, N., & Smith-Moore, M. 1988, Michigan Catalogue of Two-dimensional Spectral Types for the HD Stars, 4 (Ann Arbor, MI: Univ. Michigan)
Howard, A. W., & Fulton, B. J. 2016, PASP, 128, 114401
Howard, A. W., Johnson, J. A., Marcy, G. W., et al. 2010, ApJ, 721, 1467
Howard, A. W., Marcy, G. W., Bryson, S. T., et al. 2012, ApJS, 201, 15
Huber, D., Zinn, J., Bojsen-Hansen, M., et al. 2017, ApJ, 844, 102
Hunter, J. D. 2007, CSE, 9, 90
Isaacson, H., & Fischer, D. 2010, ApJ, 725, 875
Jeffreys, H. 1946, RSPSA, 186, 453
Jenkins, J. M. 2002, ApJ, 575, 493
Jenkins, J. M., Chandrasekaran, H., McCauliff, S. D., et al. 2010, Proc. SPIE, 7740, 77400D
Jenkins, J. M., Tenenbaum, P., Seader, S., et al. 2020, in Kepler Data Processing Handbook: Transiting Planet Search, Kepler Science Document KSCI-19081-003, id. 9, ed. Jon M. Jenkins (Moffett Field, CA: NASA Ames Research Center)
Jenkins, J. M., Twicken, J. D., McCauliff, S., et al. 2016, Proc. SPIE, 9913, 99133E
Kallinger, T., De Ridder, J., Hekker, S., et al. 2014, A&A, 570, A41
Kempton, E. M. R., Bean, J. L., Louie, D. R., et al. 2018, PASP, 130, 114401
Kipping, D. M. 2013, MNRAS, 435, 2152
Kite, E. S., Fegley, Bruce, J., Schaefer, L., & Ford, E. B. 2019, ApJL, 887, L33
Kite, E. S., Fegley, Bruce, J., Schaefer, L., & Ford, E. B. 2020, ApJ, 891, 111
Kosiarek, M. R., Berardo, D. A., Crossfield, I. J. M., et al. 2021, AJ, 161, 47

Kosiarek, M. R., & Crossfield, I. J. M. 2020, AJ, 159, 271
Kosiarek, M. R., Crossfield, I. J. M., Hardegree-Ullman, K. K., et al. 2019, AJ, 157, 97
Kovács, G., Zucker, S., & Mazeh, T. 2002, A&A, 391, 369
Li, J., Tenenbaum, P., Twicken, J. D., et al. 2019, PASP, 131, 024506
Lightkurve Collaboration, Cardoso, J. V. d. M., Hedges, C., et al. (2018) Lightkurve: Kepler and TESS time series analysis in Python, Astrophysics Source Code Library, ascl:1812.013
Lindegren, L., Mignard, F., Söderhjelm, S., et al. 1997, A&A, 323, L53
Lissauer, J. J., Marcy, G. W., Rowe, J. F., et al. 2012, ApJ, 750, 112
Lomb, N. R. 1976, Ap&SS, 39, 447
Lopez, E. D., & Fortney, J. J. 2014, ApJ, 792, 1
Lopez, E. D., Fortney, J. J., & Miller, N. 2012, ApJ, 761, 59
Lubin, J., Van Zandt, J., Holcomb, R., et al. 2022, AJ, 163, 101
Luger, R., Agol, E., Foreman-Mackey, D., et al. 2019, AJ, 157, 64
Lundkvist, M. S., Kjeldsen, H., Albrecht, S., et al. 2016, NatCo, 7, 11201
Luque, R., & Pallé, E. 2022, Sci, 377, 1211
MacDougall, M. G., Petigura, E. A., Angelo, I., et al. 2021, AJ, 162, 265
Madhusudhan, N. 2019, ARA&A, 57, 617
Mamajek, E. E., & Hillenbrand, L. A. 2008, ApJ, 687, 1264
Marshall, D. J., Robin, A. C., Reylé, C., Schultheis, M., & Picaud, S. 2006, A&A, 453, 635
Metropolis, N., Rosenbluth, A. W., Rosenbluth, M. N., Teller, A. H., & Teller, E. 1953, JChPh, 21, 1087
Meunier, N., Desort, M., & Lagrange, A. M. 2010, A&A, 512, A39
Middelkoop, F. 1982, A&A, 107, 31
Monteux, J., Golabek, G. J., Rubie, D. C., Tobie, G., & Young, E. D. 2018, SSRv, 214, 39
Morris, R. L., Twicken, J. D., Smith, J. C., et al. 2020, in Kepler Data Processing Handbook: Photometric Analysis, Kepler Science Document KSCI-19081-003, id. 6, ed. Jon M. Jenkins (Moffett Field, CA: NASA Ames Research Center)
Morton, T. D., Bryson, S. T., Coughlin, J. L., et al. 2016, ApJ, 822, 86
NASA Exoplanet Archive 2022, Planetary Systems, Version: 2022-11-17, NExScI-Caltech/IPAC, doi:10.26133/NEA12
Neal, R. M. 2003, AnSta, 31, 705
Neal, R. M. 2012, arXiv:1206.1901
Noyes, R. W., Hartmann, L. W., Baliunas, S. L., Duncan, D. K., & Vaughan, A. H. 1984, ApJ, 279, 763
Orell-Miquel, J., Nowak, G., Murgas, F., et al. 2023, A&A, 669, A40
Osborn, H. P., Bonfanti, A., Gandolfi, D., et al. 2022, A&A, 664, A156
Osborn, H. P., Nowak, G., Hébrard, G., et al. 2023, MNRAS, 523, 3069
Otegi, J. F., Dorn, C., Helled, R., et al. 2020, A&A, 640, A135
pandas development team, T 2020, pandas-dev/pandas: Pandas, 2.0, Zenodo, doi:10.5281/zenodo.3509134
Pedregosa, F., Varoquaux, G., Gramfort, A., et al. 2011, JMLR, 12, 2825, https://www.jmlr.org/papers/volume12/pedregosa11a/pedregosa11a.pdf
Perruchot, S., Kohler, D., Bouchy, F., et al. 2008, Proc. SPIE, 7014, 70140J
Petigura, E. A. 2020, AJ, 160, 89
Petigura, E. A., Howard, A. W., & Marcy, G. W. 2013, PNAS, 110, 19273
Petigura, E. A., Howard, A. W., & Marcy, G. W., et al. 2017, AJ, 154, 107
Piaulet, C., Benneke, B., Rubenzahl, R. A., et al. 2021, AJ, 161, 70
Plavchan, P., Latham, D., Gaudi, S., et al. 2015, arXiv:1503.01770
Press, W. H., Teukolsky, S. A., Vetterling, W. T., & Flannery, B. P. 1992, Numerical recipes in C. The art of scientific computing (Cambridge: Cambridge Univ. Press)

Gaia Collaboration, Prusti, T., de Bruijne, J. H. J., et al. 2016, A&A, 595, A1
Rasmussen, C. E., & Williams, C. K. I. 2006, Gaussian Processes for Machine Learning (Cambridge, MA: MIT Press)
Raymond, S. N., Boulet, T., Izidoro, A., Esteves, L., & Bitsch, B. 2018, MNRAS, 479, L81
Ricker, G. R., Winn, J. N., Vanderspek, R., et al. 2014, JATIS, 1, 014003
Robertson, P., Endl, M., Cochran, W. D., & Dodson-Robinson, S. E. 2013, ApJ, 764, 3
Rogers, L. A., & Seager, S. 2010, ApJ, 712, 974
Rosenthal, L. J., Fulton, B. J., Hirsch, L. A., et al. 2021, ApJS, 255, 8
Salvatier, J., Wiecki, T. V., & Fonnesbeck, C. 2016, PeerJ Comp. Sci., 2, e55
Savitzky, A., & Golay, M. J. E. 1964, AnaCh, 36, 1627
Scargle, J. D. 1982, ApJ, 263, 835
Scarsdale, N., Murphy, J. M. A., Batalha, N. M., et al. 2021, AJ, 162, 215
Schlafly, E. F., & Finkbeiner, D. P. 2011, ApJ, 737, 103
Schlichting, H. E., & Young, E. D. 2022, PSJ, 3, 127
Schlieder, J. E., Gonzales, E. J., Ciardi, D. R., et al. 2021, FrASS, 8, 63
Schwarz, G. 1978, AnSta, 6, 461
Skrutskie, M. F., Cutri, R. M., Stiening, R., et al. 2006, AJ, 131, 1163
Smith, J. C., Stumpe, M. C., Cleve, J. E. V., et al. 2012, PASP, 124, 1000
Stassun, K. G., Oelkers, R. J., Paegert, M., et al. 2019, AJ, 158, 138
Stumpe, M. C., Smith, J. C., Catanzarite, J. H., et al. 2014, PASP, 126, 100
Stumpe, M. C., Smith, J. C., Cleve, J. E. V., et al. 2012, PASP, 124, 985
Tayar, J., Claytor, Z. R., Huber, D., & van Saders, J. 2022, ApJ, 927, 31
Teske, J., Wang, S. X., Wolfgang, A., et al. 2021, ApJS, 256, 33
Theano Development Team 2016, arXiv:1605.02688
Twicken, J. D., Catanzarite, J. H., Clarke, B. D., et al. 2018, PASP, 130, 064502
Twicken, J. D., Clarke, B. D., Bryson, S. T., et al. 2010, Proc. SPIE, 7740, 774023
Valencia, D., Sasselov, D. D., & O'Connell, R. J. 2007, ApJ, 665, 1413
Van Eylen, V., Agentoft, C., Lundkvist, M. S., et al. 2018, MNRAS, 479, 4786
Van Eylen, V., Albrecht, S., Huang, X., et al. 2019, AJ, 157, 61
Van Rossum, G., & Drake, F. L. 2009, Python 3 Reference Manual (Scotts Valley, CA: CreateSpace)
Vanderburg, A., Huang, C. X., Rodriguez, J. E., et al. 2019, ApJL, 881, L19
Vanderburg, A., Plavchan, P., Johnson, J. A., et al. 2016, MNRAS, 459, 3565
Vehtari, A., Gelman, A., Simpson, D., Carpenter, B., & Bürkner, P.-C. 2021, BayAn, 16, 667
Virtanen, P., Gommers, R., Oliphant, T. E., et al. 2020, NatMe, 17, 261-272
Vogt, S. S., Allen, S. L., Bigelow, B. C., et al. 1994, Proc. SPIE, 2198, 362
Vogt, S. S., Radovan, M., Kibrick, R., et al. 2014, PASP, 126, 359
Vrieze, S. 2012, Psychol. Methods, 172, 228
Wizinowich, P., Acton, D. S., Shelton, C., et al. 2000, PASP, 112, 315
Wright, J. T. 2005, PASP, 117, 657
Wright, J. T., Marcy, G. W., Butler, R. P., et al. 2008, ApJL, 683, L63
Yee, S. W., Petigura, E. A., & von Braun, K. 2017, ApJ, 836, 77
Zechmeister, M., & Kürster, M. 2009, A&A, 496, 577
Zeng, L., Jacobsen, S. B., Sasselov, D. D., et al. 2019, PNAS, 116, 9723
Zeng, L., Sasselov, D. D., & Jacobsen, S. B. 2016, ApJ, 819, 127
Zhang, M., Knutson, H. A., Wang, L., Dai, F., & Barragán, O. 2022, AJ, 163, 67
Zhu, W., Petrovich, C., Wu, Y., Dong, S., & Xie, J. 2018, ApJ, 860, 101